

Survey of X-rays from Massive Stars Observed at High Spectral Resolution with *Chandra*

PRAGATI PRADHAN,^{1, 2,*} DAVID P. HUENEMOERDER,^{1, †} RICHARD IGNACE,³ JOY S. NICHOLS,⁴ AND A.M.T. POLLOCK⁵

¹*Massachusetts Institute of Technology , 77 Massachusetts Ave., Cambridge, MA 02139, USA*

²*Embry Riddle Aeronautical University, Department of Physics & Astronomy, 3700 Willow Creek Road Prescott, AZ 86301, USA*

³*Department of Physics & Astronomy, East Tennessee State University, Johnson City, TN 37614 USA*

⁴*Center for Astrophysics — Harvard & Smithsonian , 60 Garden Street, Cambridge, MA 02138, USA*

⁵*Department of Physics and Astronomy, University of Sheffield, Hounsfield Road, Sheffield S3 7RH, UK*

ABSTRACT

Identifying trends between observational data and the range of physical parameters of massive stars is a critical step to the still-elusive full understanding of the source, structure, and evolution of X-ray emission from the stellar winds, requiring a substantial sample size and systematic analysis methods. The *Chandra* data archive as of 2022 contains 37 high resolution spectra of O, B, and WR stars, observed with the *Chandra*/HETGS and of sufficient quality to fit the continua and emission line profiles. Using a systematic approach to the data analysis, we explore morphological trends in the line profiles (i.e., O, Ne, Mg, Si) and find that the centroid offsets of resolved lines versus wavelength can be separated in three empirically-defined groups based on the amount of line broadening and centroid offset. Using Fe XVII (15.01 Å, 17.05 Å) and Ne X α (12.13 Å) lines which are prevalent among the sample stars, we find a well-correlated linear trend of increasing Full Width Half Maximum (FWHM) with faster wind terminal velocity. The H-like/He-like total line flux ratio for strong lines displays different trends with spectral class depending on ion species. Some of the sources in our sample have peculiar properties (e.g., magnetic and γ Cas-analogue stars) and we find that these sources stand out as outliers from more regular trends. Finally, our spectral analysis is presented summarily in terms of X-ray spectral energy distributions in specific luminosity for each source, plus tables of line identifications and fluxes.

1. INTRODUCTION

X-ray studies of massive star winds have been central to the ongoing understanding of their structured and time-variable flows (e.g., Güdel & Nazé 2009; Oskinova 2016). Studies tend to fall into two categories: intensive observations of individual or binary stars and coarse observations for larger samples of objects, for example characterizing basic X-ray properties for stars in a cluster. A good example of the former would include ζ Pup, with around a ~ 1 Msec of data from *XMM-Newton* (Nazé et al. 2012) and a similar amount from *Chandra* (Huenemoerder et al. 2020; Cohen et al. 2020a; Nichols et al. 2021; Cohen et al. 2022). The star draws this continued attention because

* pradhanp@erau.edu

† dph@mit.edu

of its relative proximity, X-ray brightness, and high mass-loss rate ($2.5 \times 10^{-6} M_{\odot}/\text{yr}$; Cohen et al. 2020b) and high-speed wind v_{∞} of 2250 km/s (Puls et al. 2006a; Cohen et al. 2010a). There are numerous examples for X-ray studies of massive star populations in cluxters (e.g., Oskinova 2005; Rauw & Nazé 2016).

Fewer investigations have sought to frame massive stars in terms of an X-ray classification based on high-resolution spectral data. Certainly, there have been efforts to group high-resolution data in relation to stellar winds (Oskinova et al. 2006; Waldron & Cassinelli 2007; Cazorla & Nazé 2017), magnetic stars (Oskinova et al. 2011b; Nazé et al. 2014; ud-Doula & Nazé 2016), or studies of individual colliding-wind binaries like η Carinae, WR 147, WR 140, WR 48a, WR 25 (Corcoran et al. 2001; Zhekov & Park 2010; Pollock et al. 2005; Zhekov et al. 2014; Pradhan et al. 2021). Walborn et al. 2009 explored trends for massive stars based on *Chandra* grating spectra and found a trend of X-ray hardness correlated with spectral subtype in O and early B stars indicating a correlation between X-ray plasma temperature and stellar effective temperature. Some have argued that this variation in the X-ray hardness with spectral subtype among O stars is possibly an absorption effect (Leutenegger et al. 2010; Cohen et al. 2021a).

There remain outstanding questions concerning X-ray production from early-type massive-star winds. A key mechanism long invoked for explaining the presence of multi-million degree gas in the winds of OB stars, as well as WR stars, is rooted in the line-deshadowing instability (LDI) endemic to the wind-driving physics (e.g., Feldmeier et al. 1997). The radiative line-driving force through spectral lines (Lucy & White 1980) relates to the velocity gradient of the flow, which can have positive re-enforcement in the presence of perturbations that result in producing shock structures distributed throughout the wind (Feldmeier & Owocki 1998). Indeed, not only does LDI predict the presence of X-ray producing hot plasma, it can naturally account for the presence of structured outflow seen in other diagnostics, structure normally grouped under the heading of “clumping” (Hillier 1991; Brown et al. 1995; Hamann & Koesterke 1998; Puls et al. 2006b).

While LDI is qualitatively capable of accounting for X-ray production and structured flow in OB star winds, it has faced challenges to account quantitatively for the observations. There have been concerns about whether LDI can produce the requisite level of wind emission measure implied by observed X-ray luminosities (Feldmeier et al. 1997; Waldron & Cassinelli 2007). Also, there is uncertainty whether the LDI mechanism is capable of accounting for the well-known trend between X-ray and bolometric luminosities, with $L_X/L_{\text{bol}} \sim 10^{-7}$ observed among O and early-B stars (Long & White 1980; Berghoefer et al. 1997; Güdel & Nazé 2009; Nazé 2009). Owocki et al. (2013) have examined this scaling relation and generally found that LDI combined with photoabsorption of X-rays by the wind itself can account for the observed behavior with bolometric luminosities. There have also been concerns for whether LDI could produce X-rays at low wind velocities as implied, but this now seems to have been addressed (Sundqvist & Owocki 2013).

To understand better the underlying physics and properties for X-ray production in massive star winds requires a sufficient sample of stars to relate observations – spectral energy distributions and line shapes – to the heating of the gas (Gayley 2014; Cohen et al. 2014a). An analysis of a representative sample is complicated by the fact that early-type stars are relatively faint X-ray sources which limits the number of sources with high counts, plus the heterogeneous nature of early-type stars. Concerning the latter, there are two issues worth highlighting. The first is that binarity is common (Sana et al. 2012; de Mink et al. 2013), and magnetism is not too unusual (Wade et al. 2016). Both can alter the X-ray production in relation to predictions for the LDI mechanism

operating in single-star winds (Usov 1992; Stevens et al. 1992; Parkin & Pittard 2008; Hubrig et al. 2008b; Fossati et al. 2015; Waldron & Cassinelli 2009; Wade et al. 2016). The second issue with the heterogeneous sample is the nature of wind photoabsorption that can limit the escape of X-rays from the wind. The issue arises in two forms. One is simply that some early-type stars have high wind opacity that results in wavelength-dependent photoabsorption (e.g., Owocki & Cohen 2006); two is that structured winds (i.e., porosity) can alter the effectiveness of the wind photoabsorption (Cohen et al. 2010b; Osokinova et al. 2011a; Cohen et al. 2014b).

Understanding the LDI mechanism and disentangling its influence from other contributing mechanisms (i.e., wind collision or magnetism) continues to be a topic of active study. Cohen et al. (2021b) have presented a summary of high-resolution grating *Chandra* spectra for six O stars. In their focus on O stars, they provide an analysis of spectral trends and line profile fitting with spherically symmetric wind models for nominally single non-magnetic stars. Among their conclusions, chief is that wind absorption of X-rays is an important consideration, and that around 90% of X-rays produced in distributed wind shocks (i.e., via the LDI mechanism) are absorbed in the wind itself, with only 10% of the emission escaping. They attribute the empirical relation of $L_X \approx 10^{-7} L_{\text{bol}}$ as primarily related to wind absorption effects.

Here we continue and extend the efforts of Waldron & Cassinelli (2007), Walborn et al. (2009), and Cohen et al. (2021b) by considering a sample of early-type massive stars with high-resolution *Chandra* spectra. For our approach we adopt three main criteria for inclusion in the sample: (1) sources must be massive stars, (2) sources must have HETG spectra, and (3) the spectra, possibly from multiple pointings, must have a minimum number of counts to facilitate line profile analysis. The application of these criteria leads to about 40 sources consisting of a mix of types – putative single stars (or stars with distant companions), binary stars, magnetic stars, and a range of spectral types B, O, and Wolf-Rayet (WR). Section 2 describes the observations, Section 3 details the sample of stars, Section 4 details the fitting procedures. The results, discussion and summary are outlined in Sections 5, 6 and 7, respectively, followed by line measurement tables in Appendix B and spectrum plots as luminosity density in Appendix C.

2. OBSERVATIONS

Data for this project were taken from archival *Chandra* High Energy Transmission Grating Spectrometer (HETGS) observations. The HETGS covers the band from Fe xxv (1.85 Å) to N VII (24.78 Å) with resolving powers up to about 1000 and effective area up to about 150 cm². For details on the instrument, see Canizares et al. (2005) or the *Chandra* Proposers’ Observatory Guide¹.

The data are primarily comprised of the targets proposed by the principal investigators of the observations. In some cases (HD 150135, Cyg OB2-9, and ζ Ori B), we identified serendipitous sources in the field by searching for overlap between OB-star catalogs and all HETGS pointings. We accepted only candidate objects which were within 3 arcmin of the aim-point, since the resolving power rapidly degrades off-axis beyond 2 arcmin.

For high-resolution spectroscopy, a relatively large number of counts is necessary to achieve sufficient signal-to-noise (S/N) ratios for analysis of lines in terms of line width and location of peak line emission. For merged spectra of unique sources, we adopted a minimum number of counts in a dispersed spectrum of about 1800. Among the sources that we examined, the highest number

¹ For a detailed description of the spectrometer parameters and performance, see <https://cxc.harvard.edu/proposer/POG/html/chap8.html>

of counts was over 150,000 for γ Cas (the next brightest was 62,000). Slightly more than half the sources had more than 10,000 counts. The count rates per second ranged from 0.012 to 3.0. Observational information for the sample is given in Table 1.

3. SAMPLE OF STARS

The properties of our sample stars are summarized in Table 2. The sample is comprised of a wide range of X-ray luminosities, as derived from this work, from a few 10^{30} up to $1.6 \times 10^{34} \text{ erg s}^{-1}$, which approximately covers the known range of X-ray luminosities encountered for massive stars (Nebot Gómez-Morán & Oskinova 2018b). The luminosities and uncertainties listed in Table 2 were computed from the flux-calibrated high resolution spectra after correction for interstellar absorption.

There are 8 probable isolated stars and 27 stars in known binary systems. Eight stars in the sample are known or suspected magnetic stars; three are γ Cas and analogs; and three in the Cyg OB2 cluster display peculiar X-ray properties. The normal and atypical stellar groups are listed in Table 3.

Stellar parameters for the stars studied were collected from the literature available before 2022 April. A reference for each value is noted in the table. Preference was given to more recent work. Because we are using these values to evaluate trends across the spectral types surveyed, we did not collect the primary references for all values. If GAIA parallaxes were available for a source and appropriate priors were used by the respective authors in the literature references to make distance estimates, these distance estimates are preferred in Table 2.

4. SPECTRAL EXTRACTION AND FITTING

For most observations, we retrieved data from the Chandra archive and reprocessed with CIAO (Fruscione et al. 2006), using TGCat scripts (Huenemoerder et al. 2011). We modified the detection defaults to search in a small box centered on the known source position. For these extractions, we used CIAO versions 4.11-4.13, depending on the date of production. For a few sources (WR 6, WR 25, and ζ Pup), we already possessed data products from our previously published work (Huenemoerder et al. 2015b, 2020; Pradhan et al. 2021), and adopted those files for this study. In those cases CIAO versions 4.5, 4.8, and 4.10 had been used. In all cases we used the matched calibration database (CALDB) versions as updated after the observations so that time-dependent quantities (like the detector filter contamination) would be from interpolations, not extrapolations.

Some sources with small angular separations required modification of the cross-dispersion extraction region. ζ Ori A and B are quite close (2.4 arcsec separation); in two observations we used a narrow region, and in two observations we had to ignore component B altogether because of overlap with the much brighter component A. For HD 150135, one observation had an unfavorable roll, for which we reduced the extraction width to avoid the dispersed spectrum of HD 150136. The CIAO response computations account for this reduced width.

Our goal is to provide emission-line parameters for the sample of stars in a source-model-free manner. We adopt a simple approach for line profile fitting consisting of a sum of Gaussian emission lines plus a continuum model. While emission lines are theoretically not necessarily described by a Gaussian profile, this shape is typically adequate for characterizing the line profiles, given the wind broadening typical of the lines combined with the level of resolving power for the HETG. For some long-wavelength lines where wind absorption is stronger and resolving power is highest,

Table 1. The list of sources along with their observed fluxes (uncorrected for absorption), count rates, exposures, percentage uncertainty, number of observations, and a list of the observation-identifiers used in this work. The uncertainty is based on the square root of total counts and pertains as well to the integrated flux, f_x .

Index	Object	$10^{11} f_x$ (erg cm $^{-2}$ s $^{-1}$)	Rate (ct ks $^{-1}$)	Exp. (ks)	Err. (%)	#	ObsIDs
1	9 Sgr	0.24	40.39	146	1.3	2	5398 6285
2	ζ Oph	0.52	89.90	84	1.2	2	2571 4367
3	M17 Cen 1B	0.10	17.03	172	1.8	2	9948 10680
4	M17 Cen 1A	0.25	40.27	172	1.2	2	9948 10680
5	HD 191612	0.10	16.88	338	1.3	10	16653 16654 16655 17489 17655 17694 18743 18753 18754 18821
6	Cyg OB2-12	0.20	46.80	138	1.2	1	16659
7	Cyg OB2-9	0.16	28.73	65	2.3	1	2572
8	Cyg OB2-8A	0.52	146.80	65	1.0	1	2572
9	HD 206267	0.13	19.84	212	1.5	5	1888 1889 16309 16532 16533
10	γ Cas	17.65	3000.00	51	0.3	1	1895
11	ξ Per	0.28	44.84	159	1.2	1	4512
12	15 Mon	0.22	19.88	100	2.2	3	5401 6247 6248
13	δ Ori	0.94	99.49	528	0.4	5	639 14567 14568 14569 14570
14	ϵ Ori	0.76	89.93	92	1.1	1	3753
15	V640 Mon	0.32	52.97	320	0.8	6	17730 17731 17732 18751 18752 19955
16	ζ Ori A	1.22	143.70	367	0.4	7	610 1524 13460 13461 14373 14374 14375
17	ζ Ori B	0.11	8.05	205	2.5	3	13460 14373 14374
18	σ Ori Aa	0.21	25.44	91	2.1	1	3738
19	θ^1 Ori C	3.09	546.00	2035	0.1	68	3 4 2567 2568 7407 7408 7409 7410 8568 8589 8895 8896 8897 22334 22335 22336 22337 22338 22339 22340 22341 22342 22343 22892 22893 22904 22993 22994 22995 22996 22997 22998 22999 23000 23001 23002 23003 23004 23005 23006 23007 23008 23009 23010 23011 23012 23087 23097 23104 23114 23115 23120 23206 23207 23208 23233 24622 24623 24624 24829 24830 24831 24832 24834 24842 24873 24874 24906
20	ι Ori	0.85	117.10	50	1.3	2	599 2420
21	κ Ori	0.28	25.84	234	1.3	4	9939 9940 10839 10846
22	WR 6	0.15	33.55	440	0.8	3	14533 14534 14535
23	τ CMa	0.14	12.27	286	1.7	5	2525 2526 17441 17442 17593
24	HD 42054	0.27	50.20	150	1.2	2	11021 12226
25	ζ Pup	1.41	178.60	881	0.3	22	640 20154 20155 20156 20157 20158 21111 21112 21113 21114 21115 21116 21659 21661 21673 21898 22049 22076 22278 22279 22280 22281
26	γ^2 Vel	1.50	359.80	65	0.7	1	629
27	RCW 38 IRS 2	0.11	21.96	185	1.6	5	12351 15706 16535 16536 17638
28	HD 93129A	0.13	33.75	138	1.5	7	5397 7201 7202 7203 7204 7228 7229
29	HD 93250	0.21	46.32	194	1.1	5	5399 5400 7189 7341 7342
30	WR 25	1.00	215.10	85	0.7	2	18616 19867
31	θ Car	0.23	15.34	120	2.3	2	15730 16537
32	HD 110432	3.80	451.70	140	0.4	1	9947
33	β Cru	0.28	28.53	74	2.2	1	2575
34	HD 148937	0.38	86.46	99	1.1	1	10982
35	HD 150135	0.10	19.07	358	1.2	3	2569 14598 14599
36	HD 150136	0.62	137.70	358	0.5	3	2569 14598 14599
37	τ Sco	1.60	343.80	72	0.6	2	638 2305

Table 2. Stellar Parameters

Index	Star	Sp. Type	d (pc)	T_{eff} (K)	v_{∞} (km s $^{-1}$)	$\log \dot{M}$ dex(M_{\odot} yr $^{-1}$)	$\log L_x$ dex(erg s $^{-1}$)	$\log N_{\text{H}}$ dex(cm $^{-2}$)
1	9 Sgr	O4 V((f)) ²	1156 ¹	43000 ¹	2750 ¹	-6.32 ¹	32.96 ± 0.07	21.29 ± 0.07 ⁴¹
2	ζ Oph	O9.2 IVnn ⁵	182 ²⁹	32500 ¹⁹	1470 ³³	-7.03 ³⁶	31.41 ± 0.02	20.69 ± 0.10 ⁴¹
3	M17 Cen 1B	O2-4 V ³⁰	1630 ³⁰	...	3331 (850)	...	32.97 ± 0.09	22.30 ± 0.05 ^{39x}
4	M17 Cen 1A	O2-4 Vp ³⁰	1630 ³⁰	...	2932 (974)	...	33.32 ± 0.08	22.30 ± 0.05 ^{39x}
5	HD 191612	O6-8 f?p ¹³	2010 ²⁹	36000 ²¹	2400 ²¹	-7.90 ²¹	33.13	21.65 ^y
6	Cyg OB2-12	B3-4 Ia+ ¹⁶	1750 ¹⁶	...	400 ¹⁶	-5.52 ¹⁶	33.64 ± 0.03	22.31 ± 0.01 ^{16x}
7	Cyg OB2-9	O4 If + O5.5 III(f) ¹³	1709 ²⁹	40000 ¹	1685 (414)	-5.64 ¹	33.05	22.09 ^{1x}
8	Cyg OB2-8A	O6 Ib(fc) + O4.5 III(fc) ¹³	1804 ²⁹	37000 ¹	2216 (267)	-5.87 ¹	33.72	21.93 ^{1x}
9	HD 206267	O6 V(n)((fc)) + B0 V ¹³	1093 ²⁸	40900 ¹⁹	2680 ³³	...	33.29	21.64 ^y
10	γ Cas	B0.5 IVe ⁶	168 ⁷	...	1800 ⁴⁶	...	32.78 ± 0.00	20.17 ± 0.09 ⁴¹
11	ξ Per	O7.5 III((f))(n) ⁵	1134 ²⁹	35000 ¹⁹	2330 ³³	-6.66 ³⁷	32.85 ± 0.04	21.05 ± 0.08 ⁴¹
12	15 Mon	O7 V((f))z ¹³	719 ³⁰	37000 ¹	2055 ³³	-7.95 ¹	32.18 ± 0.01	20.32 ± 0.10 ⁴¹
13	δ Ori	O9.5 II Nwk ¹³	212 ⁷	31000 ¹⁹	1995 ³³	-6.40 ⁴³	31.73 ± 0.01	20.18 ± 0.07 ⁴¹
14	ϵ Ori	B0 Ib ⁴	606 ⁷	27000 ¹⁰	1910 ³³	-6.35 ¹⁰	32.59 ± 0.02	20.49 ± 0.11 ⁴¹
15	V640 Mon	O8 Iabf + O8.5:fp ¹³	1478 ²⁹	35100 ²³	2410 ³³	-6.22 ²³	33.07 ± 0.05	21.18 ± 0.11 ⁴¹
16	ζ Ori A	O9.2 Ib Nwk ¹³	226 ⁷	31000 ¹⁹	1860 ³³	-6.47 ³⁷	31.93 ± 0.01	20.40 ± 0.09 ⁴¹
17	ζ Ori B	O9.7 IIIIn ¹³	226 ⁷	...	728 (94)	...	30.87 ± 0.01	20.40 ± 0.09 ⁴¹
18	σ Ori Aa	O9.5 V + B0.2 V(n) ¹³	388 ¹²	33000 ²²	1060 ²²	-7.00 ²²	31.66 ± 0.01	20.55 ± 0.07 ⁴¹
19	θ^1 Ori C	O7 Vp ⁵	373 ²⁹	37000 ¹	580 ¹	-7.94 ¹	32.96 ± 0.11	21.54 ± 0.11 ⁴¹
20	ι Ori	O8.5 III + B0.2 V ¹³	412 ²⁸	32900 ¹⁹	2195 ³³	-9.49 ³⁷	32.27 ± 0.01	20.20 ± 0.10 ⁴¹
21	κ Ori	B0.5 Ia ¹⁷	198 ⁷	25700 ¹⁸	1525 ³³	...	31.22 ± 0.02	20.61 ± 0.08 ⁴¹
22	WR 6	WN4b ²⁶	2270 ²⁶	...	1700 ²⁵	-4.20 ²⁵	33.09	21.2 ^{47x}
23	τ CMa	O9 II ⁵	1500 ²⁸	31000 ¹⁹	1960 ³³	...	32.72 ± 0.03	20.80 ± 0.08 ⁴¹
24	HD 42054	B5 Ve ⁶	334 ²⁹	17860 ¹⁵	1684 (557)	...	31.56	19.78 ^{15x}
25	ζ Pup	O4 I(n)fp ⁵	332 ⁷	39000 ³²	2485 ³³	-5.07 ³²	32.28 ± 0.00	19.95 ± 0.08 ⁴¹
26	γ^2 Vel	WC8 + O7.5 III-V ²⁶	340 ²⁶	35000 ²⁴	1415 ³³	-4.5 ²⁴	32.32 ± 0.00	19.74 ± 0.06 ⁴¹
27	RCW 38 IRS 2	O5.5 V ⁴²	1700 ⁴²	...	3462 (1144)	...	32.93 ± 0.09	22.15 ± 0.06 ^{40x}
28	HD 93129A	O2 If*+ ³¹	2430 ³⁰	52000 ³⁴	3150 ³³	-4.7 ³⁴	33.22	21.44 ^{1x}
29	HD 93250	O4 IV(fc) ³	2555 ¹	42000 ¹	3160 ³³	-5.98 ¹	33.47 ± 0.12	21.39 ± 0.15 ⁴¹
30	WR 25	O2.5 If*/WN6 + OB ²⁶	1985 ²⁶	...	2480 ²⁵	-4.60 ²⁵	33.87 ± 0.08	21.55 ± 0.13 ⁴¹
31	θ Car	B0.5 Vp ⁺³⁵	140 ⁷	31000 ³⁸	482 (85)	...	30.77 ± 0.01	20.28 ± 0.08 ⁴¹
32	HD 110432	B0.5 IVpe ⁴⁴	416 ²⁹	20350 ¹⁴	1121 (357)	...	32.93	21.52 ^y
33	β Cru	B1 IV ⁴	85 ⁷	27000 ¹¹	420 ¹¹	-9.00 ¹¹	30.40	19.54 ^{11x}
34	HD 148937	O6 f?p+ ⁵	1102 ²⁹	41000 ²⁰	2215 ³³	...	33.09 ± 0.11	21.60 ± 0.10 ⁴¹
35	HD 150135	O6.5 V((f))z ⁵	1118 ²⁹	37900 ¹⁹	2455 ²⁷	...	32.77	21.60 ^y
36	HD 150136	O3.5/4 III(f*) + O6 IV ⁵	1049 ²⁹	46500 ⁹	3500 ⁹	-6.00 ⁹	33.59	21.61 ^y
37	τ Sco	B0 IV ⁴	215 ²⁹	32000 ⁸	1000 ⁴⁵	-9.3 ⁴⁵	31.99 ± 0.01	20.48 ± 0.09 ⁴¹

NOTE—Objects are ordered by increasing Galactic longitude. L_x was empirically determined from the flux-corrected HETG spectra, using the given values of d and N_{H} , with uncertainties being from the systematic error values on N_{H} . Uncertainties from counting statistics are given as percentages in Table 1 and scale directly to L_x . Values of v_{∞} with uncertainties in parentheses are newly determined values from this work, estimated from the widths of Ne X and Fe XVII lines. Superscripts indicate the references as follows (and for each reference, see references therein). “x” indicates the N_{H} value was derived from X-ray data and may include wind absorption as well as interstellar absorption. “y” indicates the N_{H} value was derived from $N_{\text{H}} = 0.83 \times E(B - V)10^{22} \text{ cm}^{-2}$ (Liszt 2014a,b).

References— 1: Nebot Gómez-Morán & Oschinova (2018a); 2: Arias et al. (2016); 3: Maíz Apellániz et al. (2016); 4: Zorec et al. (2009); 5: Sota et al. (2011); 6: Slettebak (1982); 7: van Leeuwen (2007); 8: Nieva & Przybilla (2014); 9: Mahy et al. (2012); 10: Puebla et al. (2016); 11: Cohen et al. (2008); 12: Schaefer et al. (2016); 13: Maíz Apellániz et al. (2019); 14: Zorec et al. (2005); 15: Nazé & Motch (2018); 16: Oschinova et al. (2017); 17: Lesh (1968); 18: Haucke et al. (2018); 19: Martins et al. (2005); 20: Nazé et al. (2008); 21: Marcolino et al. (2013); 22: Skinner et al. (2008); 23: Linder et al. (2008); 24: De Marco et al. (2000); 25: Hamann et al. (2019); 26: Rate & Crowther (2020); 27: Skinner et al. (2005); 28: Maíz Apellániz & Barbá (2020); 29: Bailer-Jones et al. (2018); 30: Maíz Apellániz et al. (2020a); 31: Maíz Apellániz et al. (2017); 32: Puls et al. (2006b); 33: Prinja et al. (1990); 34: Gruner et al. (2019); 35: Hiltner et al. (1969); 36: Cohen et al. (2021b); 37: Cohen et al. (2014b); 38: Hubrig et al. (2008a); 39: Broos et al. (2007); 40: Wolk et al. (2002); 41: Diplas & Savage (1994); 42: Weidner et al. (2010); 43: Shenar et al. (2015); 44: Nazé et al. (2022); 45: Oschinova et al. (2011b); 46: Smith & Robinson (1999); 47: Huenemoerder et al. (2015a).

Table 3. Single and Multiple Normal and Peculiar OB stars

Normal OB stars	magnetic stars and candidates	γ Cas and analogs	Cyg OB2 stars
Apparently single stars			
ζ Oph	τ Sco		
ξ Per			
ϵ Ori			
ζ Ori B			
κ Ori			
ζ Pup			
β Cru			
Confirmed binary or multiple systems			
M17 Cen 1A	9 Sgr	γ Cas	Cyg OB2 8A
M17 Cen 1B	θ^1 Ori C	HD 110432	Cyg OB2 9
HD 206267	HD 191612	HD 42054	
15 Mon	V640 Mon		
δ Ori	ζ Ori A		
σ Ori Aa	θ Car		
ι Ori	HD 148937		
τ CMa			
γ^2 Vel			
RCW 38 IRS 2			
HD 93129A			
HD 93250			
WR 25			
HD 150135			
HD 150136			
Systems of uncertain status			
WR 6		Cyg OB2 12	

asymmetrically-shaped lines may be expected (e.g., Ignace 2016). Even in these cases, a Gaussian is often still sufficient to characterize the lines relative to others and to other stars on a uniform basis.

Line fluxes are tabulated in Appendix B, both as the model-independent as-observed values, and as corrected for absorption using column densities, N_{H} , given in Table 2. Judgement must be applied when using the absorption-corrected values, since the column density comes from a variety of sources. If scaled from $E(B - V)$, we used the relation from Liszt (2014a), which is an average. If from X-ray data, it may already include some component from wind absorption, which can be significant, and which may require stellar wind modeling or independent determinations of the intrinsic and interstellar components (see for example Huenemoerder et al. 2015b, Figure 11). While we give uncertainties on N_{H} from the literature in Table 2, this is a systematic and not a random error when considering line fluxes; line fluxes for any object will be correlated with variation in assumed absorption.

Fitting the lines requires a well determined continuum level. In parts of the spectrum, however, the line density and wind broadening creates a pseudo-continuum which can be very different from the true continuum. In order to remove a large part of the systematic uncertainty due to

continuum placement, we fit absorbed plasma models to coarsely binned spectra and then used the model evaluated without the emission line contributions as a model continuum. The binning at a resolution well above the instrumental value removes dependence on the details of line shapes and centroids, and allows line fluxes to determine dominant temperatures and normalizations. Such a model is not adequate for high quality line flux determinations, but it is good for informing fits of what emission lines are likely present and what order of magnitude their relative strengths are. This provisional model is used to guide the multi-component Gaussian fitting. While we fit a plasma temperature and an absorption column in this continuum model estimation, we do not trust these as meaningful physical parameters and so do not here report them as interesting results. The temperature components and absorption are quite degenerate; physically reliable values would require detailed modeling of each source's spectrum, which is beyond the scope of this primarily empirical study.

We made no use of zeroth order spectra since the CCD imaging resolution is too low to aid in continuum level determination, and also because the zeroth order images are generally saturated, suffering from heavy photon pileup which is very difficult to mitigate. Figure 1 shows an example of a counts spectrum, the plasma model for lines plus continuum, and the continuum-only evaluation. Between about 10 and 20 Å the true continuum is well below the pseudo-continuum.

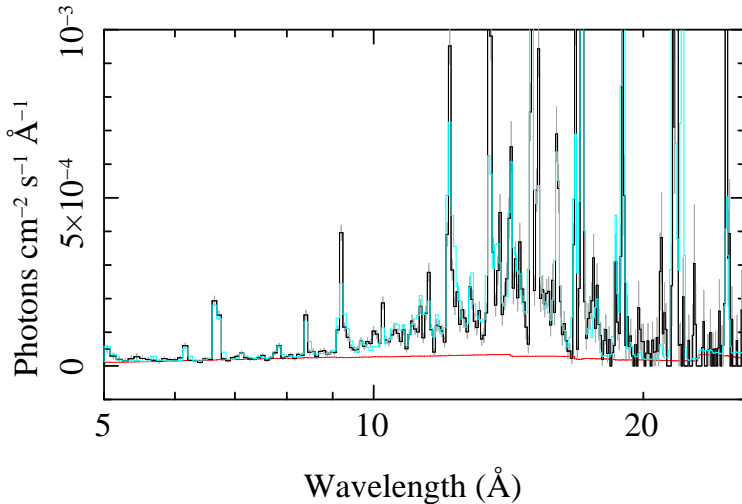


Figure 1. The black histogram shows the flux spectrum for ζ Oph. The light-colored curve overlaying it (cyan) is a plasma model including line plus continuum emission. Below that (red) is the continuum contribution only, which is used as the baseline for Gaussian line fitting.

We adopt standard X-ray spectral fitting methods that employ iterative forward-folding, in which one takes a model flux, convolves it by the instrument response, computes a statistic, and then iterates parameters to minimize the statistic. This is required because the count spectrum cannot be uniquely inverted, and because inversion can amplify noise. The forward folding also maintains rigorous handling of Poisson counting statistics. Our fitting handles the four first orders of high energy grating (HEG) ± 1 and medium energy grating (MEG) ± 1 simultaneously. Since the wind-broadened lines are resolved at the lower MEG resolving power, we matched HEG grids to MEG and

combine data dynamically during the fit — each order is still folded by the individual responses, but model counts are combined before computing the statistic. This is mainly a convenience because it means models only need to be evaluated once on a common grid, saving computation time (which can be significant when evaluating confidence limits), and for visualization of a single, combined result. There is no quantitative statistical advantage because we are using a maximum-likelihood statistic. We used a Cash statistic and an amoeba-subplex minimization method (Rowan 1990).² All spectral fitting was performed using the Interactive Spectral Interpretation System (ISIS software³, Houck & Denicola 2000), which also provides interfaces to AtomDB (Smith et al. 2001; Foster et al. 2012) as well as to `xspec` (Arnaud 1996) models.

Emission lines were fitted in groups of overlapping or close features, using sums of Gaussian profiles folded through the instrument response. If features were too blended or too weak for unconstrained fits, they were restricted accordingly, either by constraining its parameters to a stronger line’s parameters or by freezing the position or width and fitting the flux. For example, for the weak Fe XXV line (1.858 Å) present in some stars, we froze the wavelength to the theoretical value and the Gaussian σ to the typical value for massive stars, so that we could constrain only the flux. The r , i lines (3.949 Å, 3.968 Å) of Ar XVII cannot be resolved with HETG and therefore both lines were fitted with a single Gaussian while the f line (3.994 Å) was tied in wavelength offset and Gaussian σ to the ($r + i$) line’s value. The S XV triplets (5.039 Å, 5.065 Å, 5.102 Å) and Si XIII triplets (6.648 Å, 6.687 Å, 6.740 Å) were fitted with three Gaussians with the wavelength offsets and Gaussian σ of the i and f line tied to the r line. Being blended with Ne X (9.291 Å), the Mg XI region was fitted with six Gaussians (9.169 Å, 9.230 Å, 9.291 Å, 9.314 Å, 9.362 Å, 9.481 Å) with the wavelength offset and Gaussian σ of five lines fixed to the strongest Mg XI r -line. In some cases, we also froze the Gaussian σ of the Ne X β (10.239 Å) and Ne X γ (9.708 Å) lines since this region is heavily blended with Fe making independent constraints difficult. The Gaussian σ and wavelength offsets of Fe XVII (12.266 Å) and Fe XXI (12.393 Å) were tied to the main Ne X Ly α -like line (12.135 Å). The Ne IX region was fitted with six lines (13.447 Å, 13.497 Å, 13.552 Å, 13.699 Å, 13.795 Å, 13.825 Å) with the wavelength offset and Gaussian σ of five lines tied to the strongest Ne IX r line. The Fe XVII region was fitted with four Gaussian lines (15.014 Å, 15.079 Å, 15.176 Å, 15.261 Å) with the wavelength offsets tied to the 15.014 Å line. The O VIII region was fitted with four Gaussian lines (16.006 Å, 16.071 Å, 16.110 Å, 16.159 Å) at with the wavelength offsets tied to the 16.006 Å line. The Fe XVII region was fitted with two lines (17.051 Å, 17.096 Å) with the normalization of the latter line fixed at 0.86 times the first line as guided by plasma models, and the wavelength offset of 17.096 Å line tied to the 17.051 Å line. The O VII region were fitted with four Gaussian lines (21.170 Å, 21.601 Å, 21.802 Å, 22.098 Å), with the wavelength offset tied to the strongest O VII (r) line. All the isolated H-lines S XVI (4.730 Å), Si XIII β (5.681 Å), Si XIV (6.183 Å), Mg XII (8.422 Å), Ne X γ (9.708 Å), Ne X β (10.239 Å), Ne X (12.135 Å), Fe XVII (16.780 Å), O VII β (18.627 Å), O VIII (18.970 Å), N VII (24.782) were freely fitted. Emission line fit results are given in the tables in Appendix B; for tied parameters in constrained fits, uncertainties have null values. Note that for certain stars (e.g., ζ Pup), there were additional lines present, and we refer the reader to the tables in Appendix B for complete information of the line measurements.

² The ISIS implementation of the amoeba-subplex method is from <https://www.netlib.org/opt/subplex.tgz>.

³ For information on the Interactive Spectral Interpretation System (ISIS software package), see <https://space.mit.edu/cxc/ISIS/index.html>

5. RESULTS

Fundamental diagnostics of stellar winds are found in the line centroid, which can be blue-shifted from the rest wavelength by wind absorption, and the line width, which is proportional to the wind velocity. These are the primary empirical products of the emission line fitting.

In Figure 2 we show the line centroid offset frequency histogram for lines in the 7–18 Å region where the wind continuum absorption is moderate. We see two distinct groups, one near zero offset,

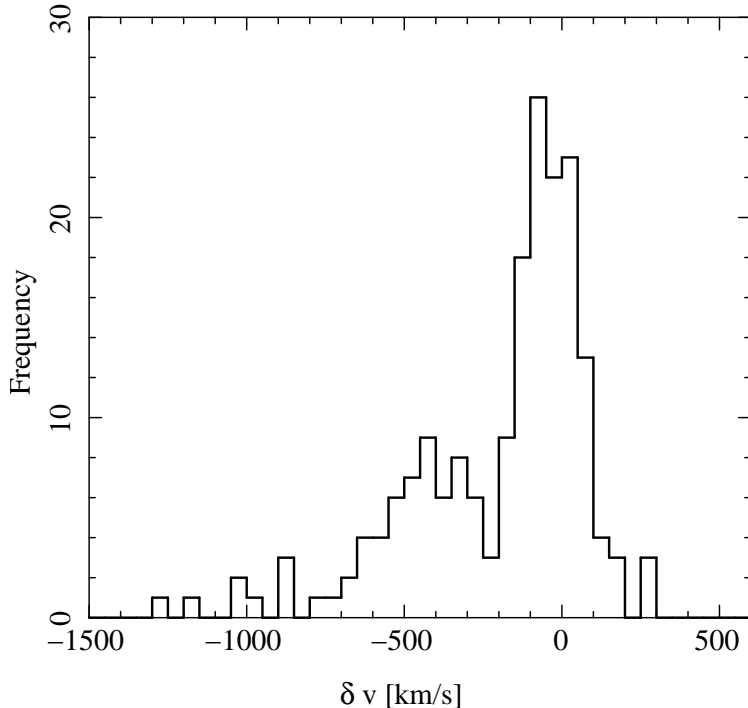


Figure 2. The frequency histogram of line centroid velocity offsets. Two distinct groups are present, centered near 0 km s^{-1} and -400 km s^{-1} , with a long tail to large negative velocities.

and another near -400 km s^{-1} , as well as a long tail to large negative velocities. We have used this distribution to sort objects into “low”, “intermediate”, or “large” velocity offset classes. In Figure 3 we show the weighted mean offsets against wavelength for stars in these groups.

Each point represents an error-weighted-mean for a particular emission line for each class. In Figure 3 we show the line widths for these same groupings, and now see only two clear loci – those with low width, and those with higher width, which increases with wavelength. If we look at the correlation of offset and width (Figure 4), we see there is a clear separation of stars with unshifted narrow lines from the others. The most-shifted group (largest absolute Δv) is comprised of 9 objects (ζ Pup, Cyg OB2-9, HD 150136, HD 206267, HD 93129A, M17 Cen 1A, RCW 38, WR 25, and WR 6), the intermediate group has 6 objects (τ CMa, ξ Per, 9 Sgr, Cyg OB2-8A, HD 150135, and HD 93250), and the remaining 22 are in the narrow, unshifted group.

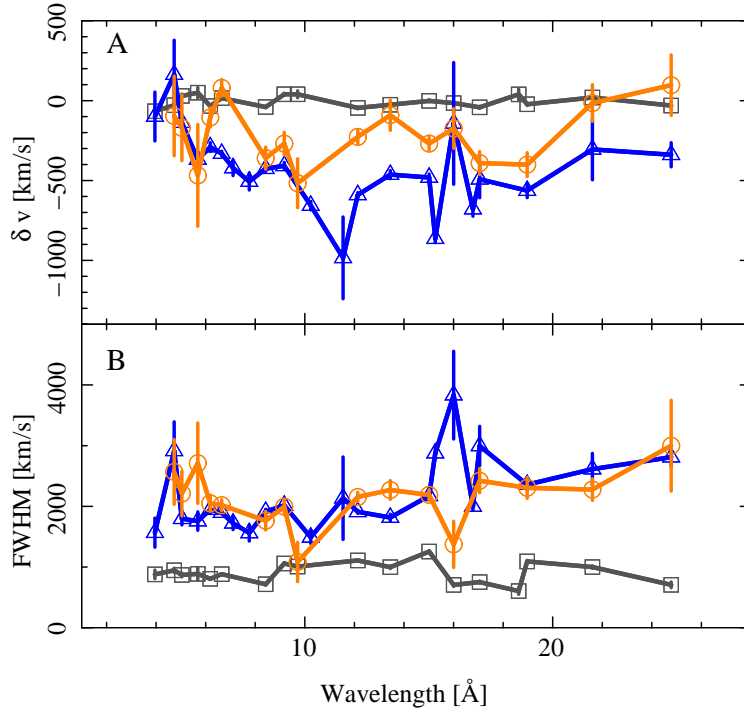


Figure 3. Error-weighted mean line centroid offsets vs line wavelength (top panel, A), and error-weighted-mean line widths vs line wavelength (bottom panel, B). Classes of objects were defined from the velocity offset histogram group (see Figure 2 and are denoted as squares (gray) for zero offset, circles (orange) for intermediate offset and triangles (blue) for large negative offsets.

In Figure 5 we show the velocity profile of the Fe XVII 15 Å line for three well-exposed spectra for a star from each group. We can easily see the difference between the unshifted and most-shifted cases in centroid and width. The middle case is more subtle, the apparent shift being more due to the width and asymmetry than the position of maximum line flux.

In Figure 6 we show a broader band view of the same three stars in units of luminosity density, along with the very different γ Cas spectrum. In this view, the OB-wind-shock systems all look quite similar, with perhaps slightly different spectral slopes and a spectral break near 15 Å. At the longest wavelength (> 20 Å), there is an apparent flattening or even rise in flux; this is artificial, and due to reaching the noise floor in the continuum. This is due to division of constant background counts by a falling effective area. If we were rigorously fitting broad-band spectral models, this would be handled by including background spectra or models in the analysis, but results here are not affected by background.

The weighted means, however, can hide significant outliers, if a mean is dominated by group of measurements with small errorbars. Hence, it is still important to look at correlations among individual objects. In Figure 7 we show our measured line widths against v_∞ from the literature. Here we can see that while there is a group of objects with $FWHM \sim 1000$ km s $^{-1}$ from the “unshifted, narrow” group (gray circles), there are also members of this group with $FWHM \sim 2000$ km s $^{-1}$. The $FWHM$ generally correlates with v_∞ , but there are significant deviations from

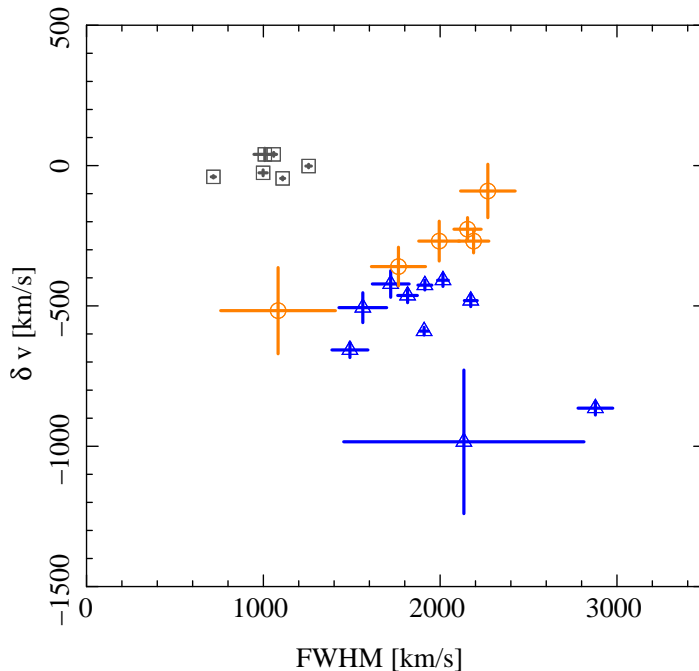


Figure 4. The correlation of centroid offset vs line width for the groupings defined by centroid offset vs wavelength shown in Figures 2 and 3, for lines in the 7.1 Å–15.3 Å range. Symbols and colors are as in Figure 3.

the 1 : 1 relationship. Since the mean X-ray $FWHM$ seems a reasonable proxy for v_∞ , we have entered the mean X-ray $FWHM$ into Table 2 as the value for v_∞ in the case of objects with no value available in the literature. The individually fit values for each feature for each star are given in tables in Appendix B.

The spectra for each object are shown in Appendix C, Figures C1–C37. In these figures, we show the absorption-corrected specific luminosity using the distances and N_{H} values from Table 2 as well as the spectra uncorrected for absorption, since in some cases this is a large and uncertain term, as can be seen in some of the spectra (e.g., Cyg OB2-12, Figure C6). The logarithmic scales all have the same range and allow inter-comparison of the strength and shape of X-ray emission. The linearly-scaled plots emphasize the emission lines and allow quick assessment of plasma characteristics, such as seen between the magnetic θ^1 Ori C and non-magnetic ι Ori (Figures C19–C20).

6. DISCUSSION

The sample of stars in this paper more than doubles the Walborn et al. (2009) sample. Using Chandra ACIS HETG existing spectra at the time, Walborn et al. (2009) fit the Ne IX and Ne x lines for the 18 stars in their study. These lines were selected because the Ne H/He ratio is expected to show strong trends throughout the temperature regime of O stars. They found that stars of later O spectral type, and thus lower T_{eff} , showed lower X-ray ionization temperatures. In comparing our work to Walborn et al. (2009), we note some differences in fitting the emission lines. First, Walborn et al. (2009) used a linear continuum of constant value for each line fit, while we used

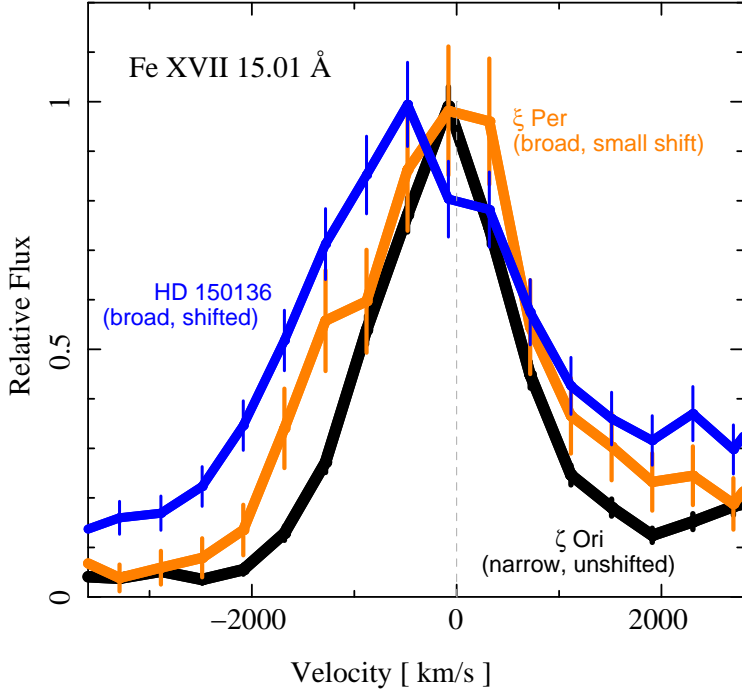


Figure 5. The Fe XVII 15 Å velocity profile for stars from each of the three velocity-offset selected groups. Colors are as in Figure 3.

a global plasma model applied to all emission lines of a star. Also, Walborn et al. (2009) used a single Gaussian fit to the Ne IX triple rather than fit each component of the triplet, as we did. See Section 4 for a complete description of the current analysis.

Walborn et al. (2009) noted S XV emission essentially disappears for spectral types later than O4. We confirm that trend with our larger dataset, and can add that the only sources in our study with measurable S XV emission later than O4 are either magnetic stars, γ Cas and analogs, or the Cyg OB2 stars. Also, for ratios of H-like to He-like fluxes, Walborn et al. (2009) found that the ratios diminish “drastically” in later O spectral types for Si XIV/Si XIII and Mg XII/Mg XI. While we confirm the general trend of lower ratios with later O spectral type, with our larger dataset we find an approximate linear decline from O3.5 to B0, with the dispersion about that linear relationship decreasing with later spectral type (smaller T_{eff}). As with the S XV results, only γ Cas and analogs, and the three Cyg OB2 stars, as well as some of the magnetic stars, have anomalously large values compared to this trend.

These conclusions are demonstrated in Figure 8. In the left panel of Figure 8 the absorption-corrected H-like/He-like ratios of Si, Mg, Ne, and O for all 37 stars in our study are plotted vs. T_{eff} (each ion is color-coded on the plot). The upper plot shows the data points with error bars, and the lower plot shows the data points without error bars, but with a linear regression line for each ion. For comparison, we show the same representation in the right panel, but we have restricted this plot to only the “normal” OB stars. The “atypical” OB stars that we excluded from the right panel were selected based on known attributes (i.e., γ Cas and analogs, magnetic stars) or based on

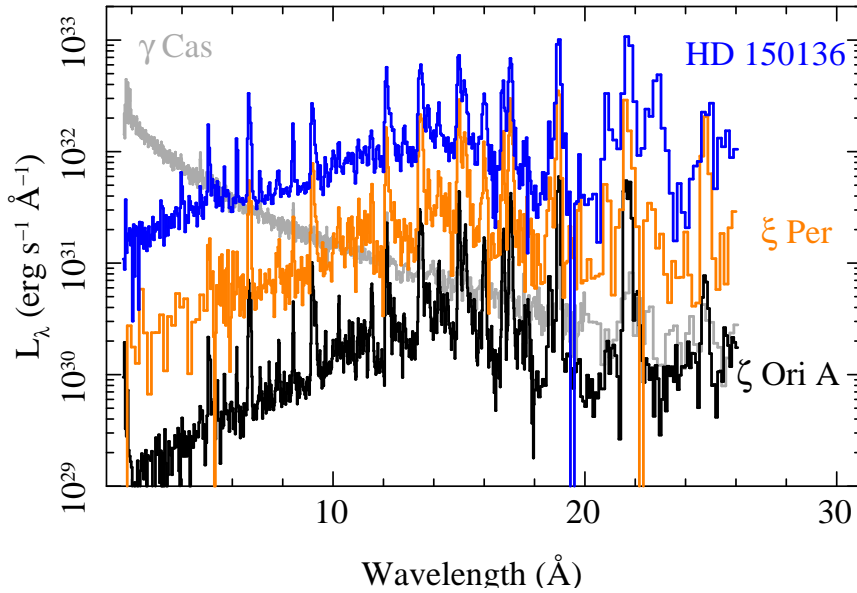


Figure 6. The luminosity density for stars from each of the three velocity-offset selected groups, plus the very different γ Cas. Colors are as in Figure 3; γ Cas is shown in gray. Spectra have been corrected for absorption using the nominal interstellar values from Table 2.

empirical evidence of disparate measurement values compared to other OB stars of their spectral type (Cyg OB2 stars). Note that binary status of the stars was not a selection criterion, so binaries exist in both the normal (9 stars) and atypical (6 stars) groups. See Table 3 for list of stars in each group, and see Table 6 for slope and intercept values of the linear fits.

A physical explanation of why these atypical stars have different spectral parameters compared to our normal group of OB stars is beyond the scope of this paper. We found no systematic difference in the emission line ratios with luminosity class for the normal stars. The H/He ratios can be an approximation to X-ray temperatures, so our results are consistent with the lower temperatures and lower ionization for later O-type spectral classes in normal stars.

It is tempting to use line ratios to determine a plasma temperature, since there is a unique relationship between the H- to He-like ratio and temperature for an isothermal plasma. However, we generally have emission measure distributions, which can greatly change the these ratios. As a qualitative aid, we adopt the powerlaw emission measure distribution defined by Huenemoerder et al. (2020) to describe the ζ Pup X-ray spectrum. The model has three primary parameters: the exponent β (unsigned, such that the emission measure is $\propto T^{-\beta}$), the maximum temperature cutoff, and the minimum temperature. In Figure 9 we show theoretical H:He photon flux ratios against the high temperature cutoff for three values of β , using the AtomDB emissivities.

Here, the minimum temperature was kept at 1 MK. The solid curves show the ratios for $\beta = 2.5$, about the value derived for ζ Pup. The ratios rise steeply at low T_{\max} and then quickly plateau. This is because beyond a certain maximum temperature, there is no longer any additional contribution from the hotter H-like line, once T_{\max} has exceeded the line's temperature of maximum emissivity. For shallower emission measure distributions (smaller β ; dashed and dotted lines), the ratios are

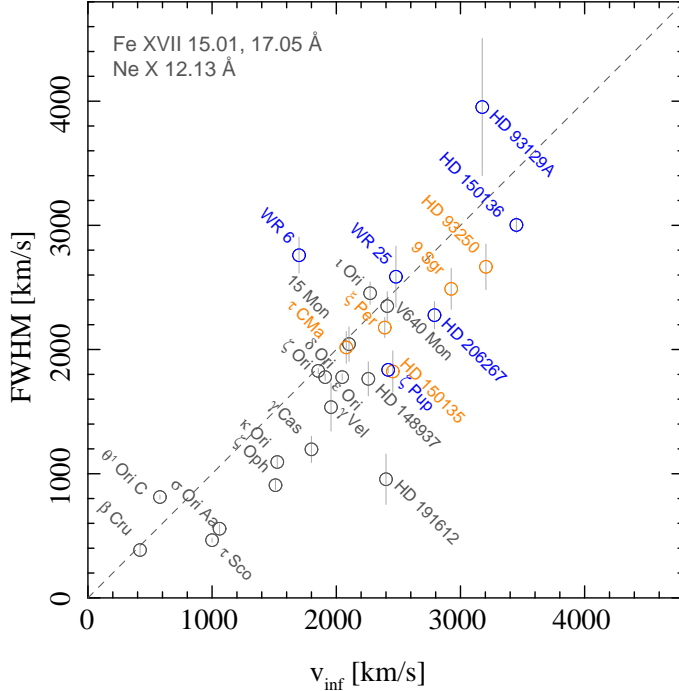


Figure 7. For each star with good measurements of the line width, we show their error-weighted-mean $FWHM$ over $\text{Ne X } 12 \text{ \AA}$, $\text{Fe XVII } 15 \text{ \AA}$ and 17 \AA . Colors are as in Figure 3. The dashed diagonal line is the $1 : 1$ dependence.

higher at any T_{\max} , since there is now relatively more contribution from the H-like line at higher T .

Comparison of these trends to the observed ratios in Figure 8 is not direct. We expect that effective temperature defines the radiation field driving the wind so higher T_{eff} implies, in general, a greater terminal velocity, v_{∞} . This, in turn, relates to the maximum embedded wind shock velocity, and thereby the T_{\max} of the emission measure distribution. Hence, T_{eff} is a qualitative proxy for T_{\max} . So it is reasonable to compare the trends in each plot, and we do indeed find them similar if we restrict to the “normal” stars (excluding known magnetic, colliding wind, or γ Cas stars): the ratios rise slightly with temperature, values are $\lesssim 1$, and they are in the same order vs element.

The power-law exponents used are reasonable for OB-stars. In addition to the fit of the model to ζ Pup, the emission measure distribution analysis of Wojdowski & Schulz (2005) and Cohen et al. (2021a) show slopes in this range. The outliers in Figure 8 tend to be points for O and Ne. These are the lines first affected by a decrease in relative emission measure at low temperatures. In the powerlaw emission measure model, if we were to increase the minimum temperature a bit, to say 3 MK, then the ratios for O and Ne would be significantly raised, by factors of about 5 and 2, respectively. For magnetically confined plasmas we might even have a more “coronal” distribution which rises with temperature, as is the case found for θ^1 Ori C (Wojdowski & Schulz 2005); it is indeed one of the outliers with H:He ratios of about 3.0 for O and Ne.

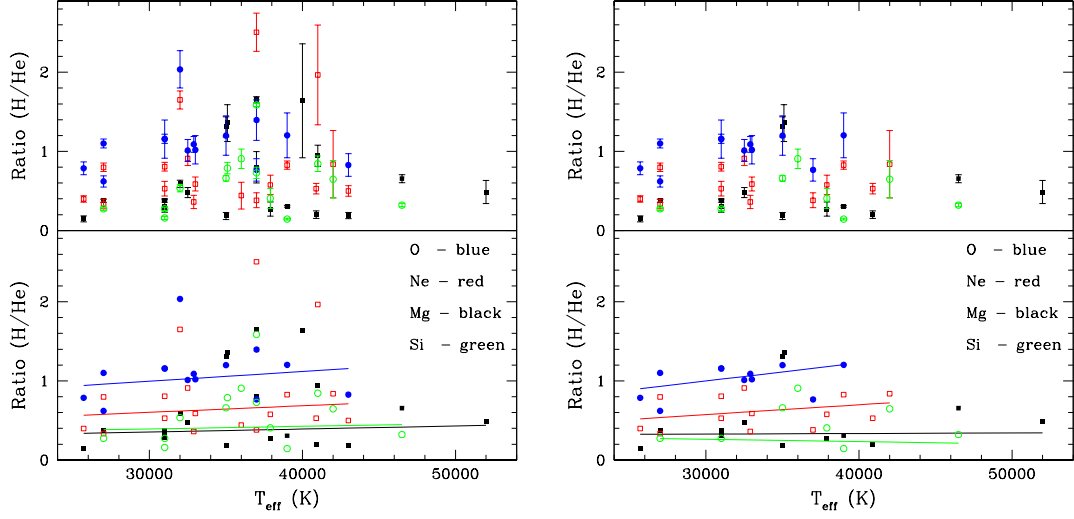


Figure 8. H/He line ratios involving O, Ne, Mg, and Si, as indicated, against source effective temperature. The left side shows all stars in our sample; right side shows only the normal stars. The upper panel displays ratios with flux measurement uncertainties. The lower panel displays linear regressions to the respective ratio data sets. The different lengths of line fits indicate the domain of temperature for which there are data. Line fluxes were corrected for the nominal interstellar absorption values given in Table 2.

Table 4. Fit Parameters for H/He Trends

Species	All Stars		Normal Stars	
	Slope (K^{-1})	Intercept	Slope (K^{-1})	Intercept
O	123×10^{-7}	0.628	220×10^{-7}	0.312
Ne	83×10^{-7}	0.353	124×10^{-7}	0.202
Mg	38×10^{-7}	0.238	7×10^{-7}	0.308
Si	34×10^{-7}	0.292	-29×10^{-7}	0.350

7. SUMMARY

In an effort to maximize the number of stars from which to assess statistical trends of massive star X-ray properties from a uniform analysis approach, we extracted a sample of hot massive star X-ray spectra taken with the *Chandra* HETGS. A selection criterion requiring a minimum of approximately 1800 total counts, possibly from multiple exposures, was adopted to ensure sufficient data quality for fitting of resolved wind-broadened line profiles. We did not limit the categories of stars in terms of being single, binary, or magnetic. We did however identify these separate categories with our analysis. Our sample consisted of 37 WR, O, and B star sources (see Tab. 2).

We identified the stronger emission line features in the spectrum of each source and fit them using Gaussian profiles. The *FWHM* of the Gaussian and the peak of line center were fit parameters.

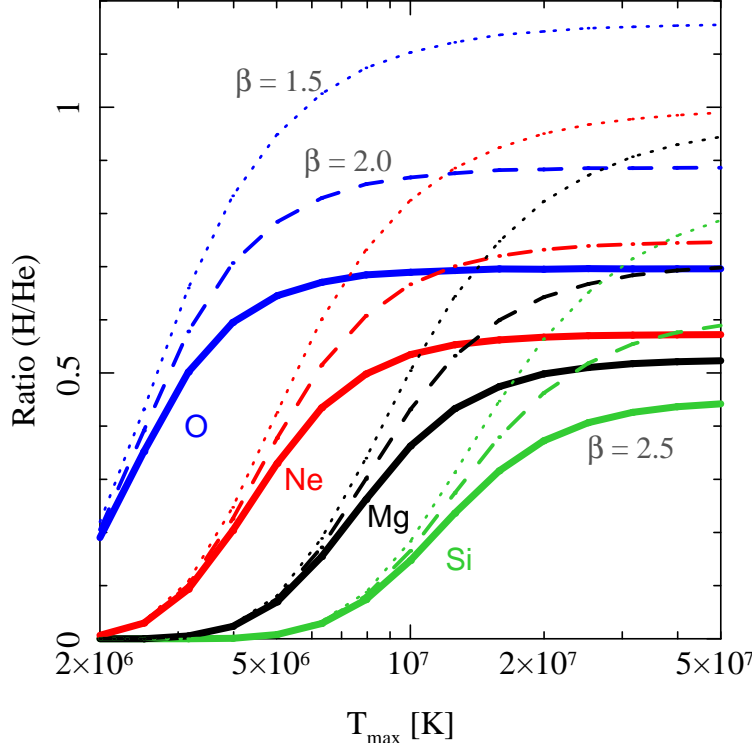


Figure 9. The H- to He-like photon flux ratios (y -axis) for several elements as labeled, for powerlaw emission measure distributions vs the high-temperature cutoff (x -axis) for three values of the exponent on temperature, β (solid lines: 2.5, dashed: 2.0, and dotted: 1.5, with larger values meaning steeper, or relatively less high-temperature plasma).

We were able to accumulate an ensemble of line measurements in terms of line width, location of peak emission, and line flux for each source, and to assign uncertainties for each measure.

The primary results found from these spectra can be summarized as follows:

1. For normal OB stars, our measurements of X-ray parameters such as H/He ratios of the X-ray emission lines and the L_x values determined herein are, in general, well described by the optically-determined spectral types and their associated T_{eff} . This finding reinforces and extends the conclusions of Walborn et al. (2009) and provides a framework for identifying atypical OB stars.
2. Three subgroups of stars were identified in terms of trends for line width (FWHM) and offset of peak line emission (Δv), as shown in Figure 4. One group was identified as having little to no shift and low to modest line broadening. Another group had broad lines and the largest shifts in peak line emission. The final group was intermediate, with modest to large line broadenings and low to modest line peak offsets. The groupings generally correlated with wind speed.

3. X-ray emission line $FWHM$ for lines at $\lambda \gtrsim 12\text{\AA}$ is a reasonable proxy for wind terminal velocity, v_∞ (see, Fig. 7). This trend could be useful for wind modeling of heavily obscured sources where UV or optical diagnostics are not available.
4. The H/He line ratio versus the effective stellar temperature for O, Ne, Mg, Si are shown in Figure 8
5. For the benefit of future analyses, tabulations of line measurements, including the velocity offsets, the full-width half maxima (FWHMs) and total flux, are provided for each star in Appendix B.
6. A gallery of X-ray spectra the form of specific luminosity vs wavelength (linear and logarithmic versions) are provided in Appendix C, placing all sources of our sample on a common footing for comparison. Determination of specific luminosities were calculated using distances and interstellar absorption values from the literature.

In this paper, we have performed a comprehensive spectral analysis focusing on the emission line properties of massive stars. We were able to investigate the individual emission lines in great details, thanks to the impeccable spectral resolution of Chandra grating spectrometers that make such high resolution studies possible. With the future of high resolution spectral studies heading towards micro calorimeter measurements (Ezoe et al. 2021), some of our findings are natural segue into understanding the plasma properties of massive stars to be investigated with XRISM and Athena/XIFU (XRISM Science Team 2020; Pajot et al. 2018). For instance, the empirical relation between the line widths of emission lines and terminal wind velocity of massive stars we present here (Fig. 7) can be useful to measure terminal wind velocity in stars found in star clusters where direct measurements with UV are not feasible due to extinction. Additionally, XRISM will also provide some complementary view of the hard X-ray properties of where Chandra gratings are not covered. This is especially useful to study line emission from hot and unusual stars in our sample.

¹ Support for this work was in part provided by NASA through the Smithsonian Astrophysical Observatory (SAO) contract SV3-73016 to MIT for Support of the *Chandra* X-Ray Center (CXC) and Science Instruments, and by *Chandra* Award Number AR8-19001 (A, B, and C) issued by the CXC. JSON acknowledges the support of NASA *Chandra* contract NAS8-03060. The CXC is operated by the Smithsonian Astrophysical Observatory for and on behalf of NASA under contract NAS8-03060.

APPENDIX

A. NOTES ON SOME INDIVIDUAL STARS

As discussed above, massive stars are usually found in binary or higher order multiple systems that have the potential to generate X-rays through the interactions of colliding winds that can rival or outshine the intrinsic emission of the winds of individual stars. Establishing system multiplicity is therefore an important consideration. Of the current sample of stars, the sometimes complex multiplicities of HD 191612, Cyg OB2-9, Cyg OB2-8A, HD 206267, 15 Mon, δ Ori, V460 Mon,

ζ Ori, σ Ori, θ^1 Ori C and ι Ori were discussed by Maíz Apellániz et al. (2019); and those of ζ Ori, ι Ori, 15 Mon, τ CMa, HD 206267 and HD 93129A by Maíz Apellániz & Barbá (2020).

9 Sgr alias HD 164794: The two *Chandra* HETG observations analysed here were taken 216 and 245 d after the 2004 October periastron passage of the most recent definition of the SB2 binary orbit of the 8.9-year period established by Fabry et al. (2021). The change in MEG count rate after the gap of about a month was small at $1.5 \pm 1.4\%$. The four XMM-Newton observations performed an orbital cycle later (Rauw et al. 2016) showed that most of the X-ray emission is intrinsic to the individual winds of the $53 M_{\odot}$ primary and $39 M_{\odot}$ secondary stars that dominate a relatively weak variable colliding-wind component that accounts for the increase of about 20% from apastron seen about a week before the 2013 September periastron.

M17 Cen 1A & 1B alias ALS 19613 A & B: According to Maíz Apellániz et al. (2020b) and references therein, these two bright X-ray sources separated by $1.65''$ at the center of the H II region M17 are both spectroscopic binaries. They have also been resolved in *Chandra* images following Broos et al. (2007) and appear with moderate pile-up warnings in the latest release 2.0.1 of the *Chandra* Source Catalog.

HD 191612: The 10 HETG observations of the magnetic star HD 191612 (Nazé et al. 2016) were scheduled in 2 groups according to the maximum and minimum phases of its primary's 537.2 day rotational period. The two sets differed by about 20% in count rate but with no obvious change in line shape so we combined all the data for analysis.

Cyg OB2-12: According to Nazé et al. (2019), the regular 108-d X-ray variability of this B-type hypergiant is not obviously of binary origin.

Cyg OB2-9 alias ALS 11422: This pair of supergiant and giant early O stars is one of the clearest examples of an X-ray colliding-wind binary system (Nazé et al. 2012): over the course of its 2.35-yr period, the luminosity varies inversely with the binary separation of its highly eccentric orbit. The single HETG spectrum available was obtained 186 days after the 2002 January periastron during an early *Chandra* observation targeted at its neighbor CygOB2-8A that lies $3.8'$ away. At this orbital phase, the luminosity of Cyg OB2-9 should already have been close to the minimum expected at apastron at a count rate consistent with the value observed.

Cyg OB2-8A alias ALS 11423: The one HETG observation of this close double-lined spectroscopic binary was obtained near the X-ray minimum of the 25% amplitude variations over the 21.9-day orbit. It was one of the brightest stars in the survey.

γ Cas: Following Nazé et al. (2022), the prototype of this class and two analogs are classified as binary systems in Table 3.

V640 Mon alias HD 47129, Plaskett's Star: When phased by the 14.4-d binary orbital period (Linder et al. 2008), the X-ray light curve of the 6 HETG observations of this SB2 shows a decrease of about 25% at an epoch reasonably consistent with an expected stellar conjunction. This merits further exploration.

- ι Ori alias HD 37043:** The tidally-induced photometric variations observed in the optical close to the periastron of the 29.1-day orbital period of this eccentric binary (Pablo et al. 2017) classify ι Ori as the most massive of the heartbeat stars. The 2 HETG exposures were taken a day apart 3 days before apastron early in the *Chandra* mission and a long time before recognition of the system's heartbeat status.
- κ Ori:** The 234 ks HETG exposure time of this early B supergiant was accumulated in 4 observations scheduled over 10 days including one long exposure responsible for nearly half the time. The mean count rates show significant variability of $9 \pm 2\%$ between the brightest and faintest. In common with stars of similar type, the fractional amplitude of X-ray variability is about an order of magnitude greater than that observed on similar timescales in the optical through TESS photometry.
- ζ Pup alias Naos, HD 66811:** After the discovery with the XMM-Newton RGS of strong N VI and N VII lines in its spectrum, the nearby, bright, single early O-star supergiant ζ Pup has continued to be observed on a roughly annual basis by XMM-Newton for long-wavelength calibration purposes. While an initial astronomical assessment by Nazé et al. (2012) of these data mistakenly cited instrumental issues, it is now well established that the X-rays generated in the wind of ζ Pup are subject to slow stochastic variability at the few percent level as well as more coherent changes of similar amplitude at the same period of 1.78 days seen in optical photometry (Nichols et al. 2021).
- γ^2 Vel alias WR 11, HD 68273:** γ^2 Velorum is a first magnitude star, the nearest and brightest Wolf-Rayet star and a binary system. The orbital period is 78.53 d (Schmutz et al. 1997) and its complex but repeatable phased X-ray light curve with a dynamic range of about 5 is still best captured by the 1991-1993 ROSAT PSPC observations (Willis et al. 1995). The combination of these data with a few subsequent XMM-Newton measurements shows a steady increase in intensity over 9 days after periastron. The single *Chandra* HETG spectrum was obtained at about $\frac{2}{3}$ of the observed maximum with little evidence of any internal variability that might have been expected.
- RCW 38 IRS 2:** The binary nature of this central ionizing system of the H II region RCW 38 was discovered by DeRose et al. (2009).
- WR 25 alias HD 93162:** Colliding winds account for most of the X-rays from this very massive Wolf-Rayet binary system of 208-d period observed with the HETG near maximum light between 10 and 12 d before periastron by Pradhan et al. (2021). The level of intrinsic emission from the wind of the Wolf-Rayet primary star may be judged by comparison with WR 24, a neighboring single star in Carina of similar type. The 6 separate observations of WR 24 reported in the *Chandra* Source Catalog define a consistent picture of an X-ray imaging count rate about a factor of 20 lower than that of the single imaging observation of WR 25 that was taken a few days before apastron.
- θ Car alias HD 93030:** The star has an accurately defined spectroscopic binary period of 2.20 d although recent TESS photometry (Koen & Johnston 2021) suggested that rotation could also be relevant. The HETG data were taken in two observations 10 days apart and partially overlaped in phase, covering in total about half the period. The HETG spectrum resolves

the narrow lines identified in the RGS spectrum early in the XMM-Newton mission (Nazé & Rauw 2008). As reported in Table 1, the measured mean X-ray line width implies a wind terminal velocity of $482 \pm 85 \text{ km s}^{-1}$ that is consistent, for example, with the velocity profile of Si IV $\lambda\lambda 1393.8, 1402.8$ absorption in the IUE spectrum.

B. LINE MEASUREMENTS TABLES

We present line measurements for each star in the following tables. The first column gives the ion names, the second column λ_0 is the theoretical wavelength of the line, the third column δv is the offset of the measured wavelength from the theoretical wavelength in velocity units, the fourth column $\sigma_{\delta v}$ is the error on this offset followed by the full-width, half-maximum (FWHM) of the line and the error on the FWHM is σ_{FW} . The next two columns are the model-independent fluxes f_x and the error on the flux, σ_{f_x} , uncorrected for interstellar absorption. The last two columns f_0 , and σ_{f_0} , are fluxes, f_x , and bounds corrected for interstellar absorption using N_{H} and its uncertainty from Table 2. (For a visual estimate of the effect of absorption, see the plots in Appendix C.) For those lines where the Gaussian line center or line width were not determined by the fit, we only provide fluxes. Since the interstellar absorption term's bounds are systematic uncertainties, any change (as per the uncertainties on N_{H} listed in Table 2) would be correlated over all lines for any given star. Hence, we have not propagated the statistical flux uncertainty with the systematic absorption uncertainty. We provide the latter to give some idea of the possible effects of uncertain absorption. The fractional statistical uncertainties on f_0 are equal to those of f_x .

Table B1. 9 Sgr

Ion	λ_0	δv	$\sigma_{\delta v}$	$FWHM$	σ_{FW}	f_x	σ_{f_x}	f_0	σ_{f_0}
	(Å)	(km s ⁻¹)	(10 ⁻⁵ photon cm ⁻² s ⁻¹)						
Si XIV	6.183	0.09	0.03	0.10	0.00
Si XIII	6.648	5	214	2774	329	0.69	0.12	0.77	0.01
Si XIII	6.740	0.28	0.05	0.30	0.00
Mg XII	8.422	-55	244	2757	479	0.36	0.06	0.43	0.01
Mg XI (r)	9.169	260	155	3641	315	1.79	0.20	2.26	0.08
Ne IX δ	9.481	0.16	0.06	0.20	0.01
Ne X β	10.239	-627	265	1629	754	0.24	0.11	0.32	0.02
Ne X	12.135	-418	103	2662	228	3.92	0.28	6.21	0.47
Fe XVII	12.266	1.07	0.18	1.71	0.13
Ne IX (r)	13.447	134	179	2909	276	6.82	0.78	12.48	1.23
Ne IX (i)	13.552	2.43	0.69	4.51	0.45
Fe XVII	15.014	-771	117	2130	310	3.90	0.51	7.89	0.91
Fe XVII	15.261	2.76	0.73	5.76	0.69
Fe XVIII	16.071	0.78	0.26	1.80	0.25
Fe XVII	16.780	-11	252	3425	501	5.21	0.76	13.35	2.06
Fe XVII	17.051	-608	123	2542	371	4.84	0.61	12.91	2.08
O VIII	18.970	-495	120	2372	282	14.53	1.71	45.98	8.73
O VII (r)	21.601	-129	269	3184	473	11.24	1.42	56.44	15.19

Table B2. ζ Oph

Ion	λ_0	δv	$\sigma_{\delta v}$	$FWHM$	σ_{FW}	f_x	σ_{f_x}	f_0	σ_{f_0}
	(Å)	(km s ⁻¹)	(10 ⁻⁵ photon cm ⁻² s ⁻¹)						
S XV	5.039	0.45	0.12	0.45	0.00
Si XIV	6.183	0.35	0.06	0.36	0.00
Si XIII	6.648	23	39	875	90	1.27	0.12	1.31	0.01
Si XIII	6.687	0.52	0.08	0.54	0.00
Si XIII	6.740	0.70	0.08	0.72	0.00
Mg XII	8.422	6	53	802	123	1.13	0.13	1.18	0.01
Mg XI (r)	9.169	5	32	968	67	2.33	0.17	2.47	0.03
Mg XI (i)	9.230	1.52	0.14	1.61	0.02
Ne X	9.291	0.20	0.09	0.21	0.00
Mg XI (f)	9.314	0.38	0.10	0.40	0.01
Ne X	9.362	0.25	0.08	0.27	0.00
Ne IX δ	9.481	0.16	0.06	0.17	0.00
Ne X γ	9.708	120	248	579	687	0.21	0.10	0.23	0.00
Ne X β	10.239	-61	83	755	248	0.87	0.17	0.94	0.02
Ne X	12.135	-128	22	784	51	9.56	0.53	10.73	0.29
Fe XVII	12.266	0.87	0.37	0.99	0.03
Fe XXI	12.284	1.66	0.39	1.87	0.05
Ne IX (r)	13.447	-83	41	1400	88	10.08	0.83	11.73	0.42
Ne IX (i)	13.552	8.22	0.76	9.60	0.35
Ne IX (f)	13.699	2.04	0.37	2.39	0.09
Fe XVII	13.825	4.40	0.71	5.18	0.20
Fe XVII	15.014	-40	30	1117	68	20.10	1.30	23.99	0.99
Fe XIX	15.079	1.18	0.47	1.41	0.06
O VIII γ	15.176	2.65	0.49	3.18	0.14
Fe XVII	15.261	9.61	0.79	11.56	0.50
O VIII β	16.006	64	84	852	155	4.55	0.79	5.61	0.27
Fe XVIII	16.071	2.92	0.69	3.61	0.18
Fe XVII	16.780	-134	37	721	81	10.44	1.04	13.23	0.73
Fe XVII	17.051	-67	47	1135	274	14.57	1.03	18.65	1.08
O VII β	18.627	-156	80	380	226	1.90	0.61	2.50	0.16
O VIII	18.970	-49	49	1098	100	28.94	2.77	38.66	2.63
O VII (r)	21.601	62	61	1264	106	25.48	2.50	38.22	3.65
N VII α	24.782	-139	87	1352	207	28.90	4.23	40.39	3.18

Table B3. M17 Cen 1B

Ion	λ_0	δv	$\sigma_{\delta v}$	$FWHM$	σ_{FW}	f_x	σ_{f_x}	f_0	σ_{f_0}
	(Å)	(km s ⁻¹)	(10 ⁻⁵ photon cm ⁻² s ⁻¹)						
Fe XXV	1.858	0.38	0.13	0.39	0.00
S XVI	4.730	0.20	0.08	0.31	0.01
S XV	5.039	0.16	0.06	0.26	0.01
Si XIV	6.183	-113	290	3331	850	0.34	0.07	0.81	0.07
Mg XI (i)	9.230	0.17	0.05	1.95	0.47
Ne X	9.362	0.08	0.04	0.98	0.25

Table B4. M17 Cen 1A

Ion	λ_0	δv	$\sigma_{\delta v}$	$FWHM$	σ_{FW}	f_x	σ_{f_x}	f_0	σ_{f_0}
	(Å)	(km s ⁻¹)	(10 ⁻⁵ photon cm ⁻² s ⁻¹)						
Fe XXV	1.858	0.82	0.23	0.85	0.00
S XVI	4.730	0.49	0.14	0.76	0.03
S XV	5.039	158	523	2782	1111	0.40	0.17	0.65	0.03
S XV	5.102	0.33	0.12	0.55	0.03
Si XIV	6.183	8	185	3052	356	0.66	0.08	1.60	0.14
Si XIII	6.648	-47	200	3276	294	0.69	0.08	2.02	0.22
Si XIII	6.740	0.57	0.08	1.59	0.16
Mg XII	8.422	-444	390	3218	840	0.26	0.06	1.67	0.31
Mg XI (r)	9.169	-1409	222	1585	424	0.22	0.06	2.34	0.55
Mg XI (i)	9.230	-	0.37	0.08	4.10	0.99
Ne X	9.362	0.13	0.05	1.60	0.40
Ne X	12.135	-366	452	2932	974	0.25	0.09	28.46	13.64

Table B5. HD 191612

Ion	λ_0	δv	$\sigma_{\delta v}$	$FWHM$	σ_{FW}	f_x	σ_{f_x}	f_0	σ_{f_0}
	(Å)	(km s ⁻¹)	(10 ⁻⁵ photon cm ⁻² s ⁻¹)						
Fe XXV	1.858	0.23	0.09	0.23	...
Ar XVII (i)	3.968	0.06	0.02	0.07	...
S XVI	4.730	0.13	0.03	0.15	...
S XV	5.039	0.17	0.04	0.19	...
S XV	5.102	0.10	0.03	0.11	...
Si XIV	6.183	-37	39	556	143	0.34	0.03	0.42	...
Si XIII	6.648	7	54	1031	146	0.36	0.04	0.46	...
Si XIII	6.687	0.12	0.02	0.15	...
Si XIII	6.740	0.17	0.03	0.21	...
Mg XII	8.422	-21	50	747	151	0.28	0.03	0.43	...
Mg XI (r)	9.169	0.28	0.04	0.47	...
Mg XI (i)	9.230	0.15	0.04	0.26	...
Ne X γ	9.708	-25	129	245	310	0.05	0.03	0.10	...
Ne X β	10.239	-266	122	485	393	0.09	0.03	0.18	...
Ne X	12.135	-59	89	933	297	0.65	0.11	1.84	...
Ne IX (r)	13.447	892	375	2716	597	1.07	0.37	4.20	...
Fe XVII	15.014	-168	140	975	278	0.87	0.24	4.27	...

Table B6. Cyg OB2-12

Ion	λ_0	δv	$\sigma_{\delta v}$	$FWHM$	σ_{FW}	f_x	σ_{f_x}	f_0	σ_{f_0}
	(Å)	(km s ⁻¹)	(10 ⁻⁵ photon cm ⁻² s ⁻¹)						
Fe XXV	1.858	0.47	0.18	0.48	0.00
Ar XVII (i)	3.968	0.18	0.07	0.24	0.00
S XVI	4.730	-506	226	1835	666	0.59	0.14	0.93	0.01
S XV	5.039	115	77	1011	198	1.46	0.17	2.43	0.03
S XV	5.065	0.23	0.11	0.38	0.00
S XV	5.102	0.59	0.11	1.00	0.01
Si XIII β	5.681	0.34	0.09	0.70	0.01
Si XIV	6.183	-91	40	1082	97	1.66	0.11	4.09	0.09
Si XIII	6.648	39	27	1007	60	2.05	0.12	6.18	0.17
Si XIII	6.687	0.46	0.07	1.40	0.04
Si XIII	6.740	1.45	0.09	4.12	0.11
Mg XII	8.422	49	57	1270	139	1.00	0.08	6.88	0.32
Mg XI (r)	9.169	190	104	1310	265	0.68	0.11	7.72	0.46
Mg XI (i)	9.230	0.25	0.08	2.97	0.18
Mg XI (f)	9.314	0.22	0.08	2.76	0.17
Ne IX δ	9.481	0.22	0.08	2.69	0.16
Ne X γ	9.708	274	163	1177	287	0.23	0.06	3.29	0.21
Ne X β	10.239	-108	218	895	404	0.14	0.06	3.03	0.23
Ne X	12.135	0.50	0.12	63.72	7.55

Table B7. Cyg OB2-9

Ion	λ_0	δv	$\sigma_{\delta v}$	$FWHM$	σ_{FW}	f_x	σ_{f_x}	f_0	σ_{f_0}
	(Å)	(km s ⁻¹)	(10 ⁻⁵ photon cm ⁻² s ⁻¹)						
Ar XVII (f)	3.994	0.27	0.11	0.32	...
S XV	5.102	0.78	0.21	1.07	...
Si XIV	6.183	0.70	0.14	1.19	...
Mg XII	8.422	-1048	207	3944	922	0.79	0.15	2.48	...
Mg XI (r)	9.169	-1445	209	1702	350	0.30	0.12	1.29	...
Mg XI (i)	9.230	0.44	0.13	1.91	...
Ne X	9.362	0.21	0.09	0.97	...
Ne IX δ	9.481	0.26	0.10	1.15	...
Ne X	12.135	-287	317	1685	414	0.62	0.23	11.13	...
Fe XVII	12.266	0.39	0.18	7.60	...

Table B8. Cyg OB2-8A

Ion	λ_0	δv	$\sigma_{\delta v}$	$FWHM$	σ_{FW}	f_x	σ_{f_x}	f_0	σ_{f_0}
	(Å)	(km s ⁻¹)	(10 ⁻⁵ photon cm ⁻² s ⁻¹)						
Fe XXV	1.858	0.78	0.30	0.80	...
Ar XVII (r)	3.949	0.25	0.12	0.28	...
Ar XVII (i)	3.968	0.39	0.14	0.43	...
S XVI	4.730	-96	249	2567	534	1.56	0.27	1.88	...
S XV	5.039	-171	205	2211	367	2.32	0.49	2.87	...
S XV	5.102	1.68	0.34	2.09	...
Si XIII β	5.681	-468	319	2712	662	1.20	0.26	1.61	...
Si XIV	6.183	-96	66	1954	144	3.81	0.25	5.54	...
Si XIII	6.648	-55	71	2123	128	4.81	0.37	7.59	...
Si XIII	6.687	1.76	0.32	2.79	...
Si XIII	6.740	2.99	0.22	4.60	...
Mg XII	8.422	-481	108	1997	247	2.46	0.28	5.46	...
Mg XI (r)	9.169	-336	286	1804	498	2.50	0.55	6.82	...
Mg XI (i)	9.230	1.15	0.47	3.19	...
Ne X	9.291	0.61	0.26	1.72	...
Ne X	9.362	0.40	0.16	1.15	...
Ne X γ	9.708	1.12	0.30	3.36	...
Ne X	12.135	-126	133	2168	282	2.50	0.39	18.50	...
Fe XXI	12.284	1.04	0.32	8.21	...
Fe XIX	13.497	0.89	0.29	12.61	...
Ne IX (i)	13.552	0.76	0.29	10.99	...
Fe XVII	15.014	-132	330	2619	824	1.98	0.87	42.20	...

Table B9. HD 206267

Ion	λ_0	δv	$\sigma_{\delta v}$	$FWHM$	σ_{FW}	f_x	σ_{f_x}	f_0	σ_{f_0}
	(Å)	(km s ⁻¹)	(10 ⁻⁵ photon cm ⁻² s ⁻¹)						
Si XIV	6.183	0.02	0.01	0.03	...
Si XIII	6.648	-130	171	1996	350	0.33	0.06	0.42	...
Si XIII	6.687	0.12	0.05	0.15	...
Si XIII	6.740	0.12	0.03	0.15	...
Mg XII	8.422	-583	309	2778	644	0.17	0.03	0.25	...
Mg XI (r)	9.169	-300	140	1997	259	0.75	0.10	1.26	...
Mg XI (i)	9.230	0.48	0.08	0.82	...
Mg XI (f)	9.314	0.18	0.05	0.30	...
Ne X	12.135	-366	79	2066	143	2.38	0.19	6.74	...
Fe XVII	12.266	0.47	0.10	1.36	...
Ne IX (r)	13.447	-87	104	1949	169	3.29	0.33	12.84	...
Ne IX (i)	13.552	1.89	0.27	7.58	...
Ne IX (f)	13.699	0.45	0.15	1.87	...
Fe XVII	15.014	-353	91	2533	177	5.20	0.53	25.48	...
Fe XVII	15.261	3.06	0.49	16.10	...
Fe XVII	16.780	-320	159	1811	490	2.59	0.51	21.70	...
Fe XVII	17.051	-455	233	3285	700	2.63	0.51	24.13	...
O VIII	18.970	-457	113	2372	362	11.06	1.57	148.81	...
N VII α	24.782	2.69	0.97	54.24	...

Table B10. γ Cas

Ion	λ_0	δv	$\sigma_{\delta v}$	$FWHM$	σ_{FW}	f_x	σ_{f_x}	f_0	σ_{f_0}
	(Å)	(km s ⁻¹)	(10 ⁻⁵ photon cm ⁻² s ⁻¹)						
S XVI	4.730	-9	101	1408	236	8.83	1.03	8.86	0.01
S XV	5.039	1427	386	2356	725	3.74	1.19	3.75	0.00
Si XIV	6.183	107	50	1176	158	8.99	0.67	9.04	0.01
Si XIII	6.648	70	106	801	244	2.29	0.47	2.31	0.00
Si XIII	6.687	0.99	0.42	1.00	0.00
Si XIII	6.740	0.89	0.39	0.90	0.00
Mg XII	8.422	40	78	1158	228	5.98	0.75	6.06	0.02
Ne X γ	9.708	1.26	0.40	1.28	0.01
Ne X	12.135	64	43	1225	111	18.32	1.25	18.97	0.14
Fe XVII	12.266	2.27	0.78	2.35	0.02
Ne IX (r)	13.447	5.86	1.08	6.13	0.06
Ne IX (i)	13.552	5.73	1.11	6.00	0.06
Fe XVII	13.825	2.04	1.00	2.14	0.02
Fe XVII	15.014	4.03	1.04	4.26	0.05
Fe XVII	15.261	2.52	0.88	2.66	0.03
O VIII β	16.006	96	88	676	169	5.56	1.25	5.92	0.08
Fe XVIII	16.071	2.65	1.05	2.83	0.04
Fe XVII	16.780	-170	105	376	237	3.23	1.19	3.47	0.05
Fe XVII	17.051	-107	163	913	347	4.82	0.53	5.20	0.08
O VIII	18.970	85	77	1232	185	32.81	4.05	35.81	0.66
O VII (r)	21.601	83	125	1387	258	19.61	3.28	22.17	0.57
O VII (f)	22.098	7.12	3.54	8.11	0.22
N VII α	24.782	-139	114	757	229	13.86	4.06	15.33	0.33

Table B11. ξ Per

Ion	λ_0	δv	$\sigma_{\delta v}$	$FWHM$	σ_{FW}	f_x	σ_{f_x}	f_0	σ_{f_0}
	(Å)	(km s ⁻¹)	(10 ⁻⁵ photon cm ⁻² s ⁻¹)						
Si XIV	6.183	0.07	0.03	0.08	0.00
Si XIII	6.648	108	118	1701	203	0.49	0.07	0.52	0.01
Si XIII	6.687	0.26	0.06	0.27	0.00
Si XIII	6.740	0.28	0.04	0.30	0.00
Mg XII	8.422	35	199	1640	357	0.22	0.05	0.25	0.00
Mg XI (r)	9.169	-377	105	1721	160	1.17	0.12	1.33	0.03
Mg XI (i)	9.230	1.04	0.11	1.19	0.03
Mg XI (f)	9.314	0.25	0.12	0.29	0.01
Ne X γ	9.708	0.12	0.04	0.14	0.00
Ne X β	10.239	-290	214	1928	500	0.42	0.12	0.50	0.02
Ne X	12.135	-254	70	2123	122	4.44	0.28	5.78	0.29
Fe XVII	12.266	1.01	0.17	1.33	0.07
Fe XVII	15.014	-148	67	2214	122	11.05	0.71	16.56	1.26
O VIII γ	15.176	2.05	0.50	3.11	0.24
Fe XVII	15.261	4.87	0.57	7.44	0.59
O VIII β	16.006	-174	125	1374	382	2.82	0.50	4.55	0.41
Fe XIX	16.110	0.86	0.30	1.40	0.13
Fe XVII	16.780	-197	116	2142	260	5.06	0.57	8.69	0.89
Fe XVII	17.051	-334	92	2251	252	6.58	0.65	11.57	1.23
O VII β	18.627	0.91	0.41	1.70	0.20
O VIII	18.970	-395	135	2408	369	21.34	2.98	41.36	5.17
O VII (r)	21.601	26	158	1975	235	13.71	2.11	34.64	6.11
O VII (i)	21.802	6.23	1.61	16.10	2.91
N VII α	24.782	97	189	3000	749	21.64	4.23	46.50	6.74

Table B12. 15 Mon

Ion	λ_0	δv	$\sigma_{\delta v}$	$FWHM$	σ_{FW}	f_x	σ_{f_x}	f_0	σ_{f_0}
	(Å)	(km s ⁻¹)	(10 ⁻⁵ photon cm ⁻² s ⁻¹)						
Si XIII	6.648	0.10	0.03	0.10	0.00
Mg XI (r)	9.169	-50	169	1415	284	0.30	0.07	0.31	0.00
Mg XI (i)	9.230	0.17	0.06	0.17	0.00
Ne X	12.135	-284	191	2451	413	1.47	0.21	1.55	0.02
Fe XVII	12.266	0.41	0.14	0.43	0.01
Ne IX (r)	13.447	49	178	2144	258	3.81	0.75	4.07	0.06
Ne IX (i)	13.552	2.32	0.57	2.48	0.04
Fe XVII	15.014	-48	118	2009	290	5.36	0.74	5.78	0.10
O VIII γ	15.176	1.02	0.49	1.10	0.02
Fe XVII	15.261	2.84	0.51	3.07	0.06
O VIII β	16.006	-478	108	1423	255	2.75	0.50	3.00	0.06
Fe XVII	16.780	-304	210	2756	461	4.50	0.70	4.97	0.12
Fe XVII	17.051	-294	118	1985	172	4.32	0.51	4.80	0.12
O VIII	18.970	-119	122	1778	245	24.67	2.94	27.91	0.80
O VII (r)	21.601	119	145	1946	204	30.58	4.27	36.35	1.47
O VII (i)	21.802	20.37	3.82	24.32	1.00
N VII α	24.782	10.88	3.89	12.55	0.42

Table B13. δ Ori

Ion	λ_0	δv	$\sigma_{\delta v}$	$FWHM$	σ_{FW}	f_x	σ_{f_x}	f_0	σ_{f_0}
	(Å)	(km s ⁻¹)	(10 ⁻⁵ photon cm ⁻² s ⁻¹)						
Fe XXV	1.858	0.15	0.04	0.15	0.00
S XVI	4.730	0.09	0.03	0.09	0.00
S XV	5.039	0.36	0.13	0.36	0.00
S XV	5.102	0.26	0.04	0.26	0.00
Si XIII β	5.681	84	144	1334	393	0.17	0.03	0.17	0.00
Si XIV	6.183	-75	50	1191	143	0.38	0.03	0.38	0.00
Si XIII	6.648	5	20	1169	43	1.38	0.05	1.39	0.00
Si XIII	6.687	0.45	0.03	0.45	0.00
Si XIII	6.740	0.83	0.04	0.83	0.00
Mg XII	8.422	-49	26	1135	70	1.05	0.04	1.06	0.00
Mg XI (r)	9.169	-34	30	1612	68	2.76	0.10	2.81	0.01
Mg XI (i)	9.230	1.57	0.08	1.60	0.00
Ne X	9.291	0.20	0.10	0.21	0.00
Mg XI (f)	9.314	0.76	0.11	0.78	0.00
Ne X	9.362	0.30	0.05	0.31	0.00
Ne IX δ	9.481	0.42	0.05	0.43	0.00
Ne X γ	9.708	60	63	805	216	0.35	0.06	0.36	0.00
Ne X β	10.239	-50	44	1000	104	0.91	0.08	0.93	0.00
Ne X	12.135	-158	17	1621	34	12.24	0.28	12.69	0.07
Fe XVII	12.266	3.67	0.17	3.80	0.02
Ne IX (r)	13.447	-127	50	2139	77	15.02	0.96	15.74	0.12
Fe XIX	13.497	5.45	1.09	5.71	0.04
Ne IX (i)	13.552	12.63	0.78	13.25	0.10
Ne IX (f)	13.699	3.15	0.29	3.31	0.03
Fe XVII	13.825	4.04	0.66	4.24	0.03
Fe XVII	15.014	-10	21	2117	45	33.89	0.73	35.79	0.32
O VIII γ	15.176	5.44	0.55	5.75	0.05
Fe XVII	15.261	16.66	0.67	17.64	0.16
O VIII β	16.006	-176	59	1288	116	9.23	0.70	9.85	0.10
Fe XVIII	16.071	5.06	0.68	5.40	0.06
Fe XVII	16.780	-205	31	1773	71	20.13	0.79	21.65	0.26
Fe XVII	17.051	-114	25	1641	66	23.40	0.71	25.25	0.31
O VII β	18.627	121	77	2025	286	9.59	1.59	10.44	0.14
O VIII	18.970	-19	19	1780	42	100.60	2.47	109.99	1.59
O VII (r)	21.601	158	37	1677	50	85.05	3.76	96.37	1.96
O VII (i)	21.802	70.73	3.57	80.39	1.67
O VII (f)	22.098	-	4.27	1.19	4.88	0.11
N VII α	24.782	-119	88	1320	217	13.51	2.06	14.98	0.25

Table B14. ϵ Ori

Ion	λ_0	δv	$\sigma_{\delta v}$	$FWHM$	σ_{FW}	f_x	σ_{f_x}	f_0	σ_{f_0}
	(Å)	(km s ⁻¹)	(10 ⁻⁵ photon cm ⁻² s ⁻¹)						
S XV	5.039	0.15	0.07	0.15	0.00
Si XIII	6.648	46	62	1072	137	0.78	0.09	0.80	0.00
Si XIII	6.687	0.21	0.06	0.21	0.00
Si XIII	6.740	0.42	0.06	0.42	0.00
Mg XII	8.422	-146	96	1063	233	0.41	0.06	0.42	0.00
Mg XI (r)	9.169	-61	60	1364	102	2.15	0.17	2.23	0.02
Mg XI (i)	9.230	0.73	0.12	0.76	0.01
Ne X	9.291	0.35	0.17	0.37	0.00
Mg XI (f)	9.314	0.71	0.19	0.74	0.01
Ne X γ	9.708	-180	211	1641	489	0.46	0.11	0.48	0.00
Ne X β	10.239	-234	72	519	251	0.55	0.12	0.58	0.01
Ne X	12.135	-190	35	1395	67	8.92	0.48	9.59	0.18
Fe XVII	12.266	1.73	0.24	1.86	0.04
Ne IX (r)	13.447	-227	42	1438	76	12.97	1.01	14.27	0.35
Fe XIX	13.497	3.24	0.97	3.57	0.09
Ne IX (i)	13.552	9.79	0.81	10.79	0.27
Ne IX (f)	13.699	4.32	0.53	4.78	0.12
Fe XVII	13.825	2.62	0.63	2.91	0.08
Fe XVII	15.014	-12	41	1839	90	26.06	1.25	29.14	0.83
O VIII γ	15.176	7.21	0.87	8.09	0.24
Fe XVII	15.261	12.03	1.06	13.52	0.40
O VIII β	16.006	-213	84	1764	176	12.20	1.06	13.92	0.47
Fe XIX	16.110	2.13	0.64	2.44	0.08
Fe XVII	16.780	-209	70	1495	177	12.82	1.29	14.88	0.57
Fe XVII	17.051	-188	55	1966	132	19.93	1.08	23.28	0.93
O VII β	18.627	8.19	1.24	9.74	0.44
O VIII	18.970	-87	33	1618	60	89.80	4.08	107.78	5.06
O VII (r)	21.601	-103	47	1654	75	95.37	4.76	123.16	8.12
O VII (f)	22.098	7.43	2.14	9.74	0.68
N VII α	24.782	206	161	2910	348	40.37	4.75	49.86	2.71

Table B15. V640 Mon

Ion	λ_0	δv	$\sigma_{\delta v}$	$FWHM$	σ_{FW}	f_x	σ_{f_x}	f_0	σ_{f_0}
	(Å)	(km s ⁻¹)	(10 ⁻⁵ photon cm ⁻² s ⁻¹)						
Fe XXV	1.858	0.44	0.10	0.44	0.00
S XVI	4.730	-226	302	2536	914	0.37	0.08	0.39	0.00
S XV	5.039	7	123	1307	242	0.49	0.09	0.51	0.00
S XV	5.102	0.33	0.07	0.35	0.00
Si XIII β	5.681	0.20	0.06	0.21	0.00
Si XIV	6.183	73	52	1537	119	0.98	0.06	1.04	0.02
Si XIII	6.648	-30	56	1711	124	1.23	0.08	1.33	0.03
Si XIII	6.687	0.34	0.07	0.37	0.01
Si XIII	6.740	0.72	0.05	0.78	0.02
Mg XII	8.422	-21	61	2062	148	1.23	0.07	1.42	0.05
Mg XI (r)	9.169	-80	175	1865	343	0.87	0.14	1.04	0.05
Mg XI (i)	9.230	0.40	0.12	0.48	0.02
Ne X γ	9.708	0.38	0.06	0.46	0.02
Ne X β	10.239	-237	211	1789	499	0.39	0.11	0.49	0.03
Ne X	12.135	-148	75	2321	135	3.86	0.25	5.52	0.52
Fe XVII	12.266	2.07	0.20	2.99	0.29
Fe XVII	15.014	78	140	2715	290	5.62	0.63	9.71	1.40
O VIII γ	15.176	1.48	0.53	2.59	0.38
Fe XVII	15.261	1.94	0.51	3.44	0.52
O VIII β	16.006	0.64	0.30	1.21	0.21
Fe XVIII	16.071	0.85	0.33	1.63	0.28
Fe XVII	16.780	0.81	0.39	1.68	0.33
Fe XVII	17.051	-51	155	1919	395	3.51	0.60	7.50	1.52
O VIII	18.970	-299	209	2200	481	4.54	1.07	11.08	2.65
N VII α	24.782	3.88	1.92	10.87	3.03

Table B16. ζ Ori A

Ion	λ_0	δv	$\sigma_{\delta v}$	$FWHM$	σ_{FW}	f_x	σ_{f_x}	f_0	σ_{f_0}
	(Å)	(km s ⁻¹)	(10 ⁻⁵ photon cm ⁻² s ⁻¹)						
S XVI	4.730	0.11	0.04	0.12	0.00
S XV	5.039	133	139	1373	238	0.30	0.05	0.30	0.00
S XV	5.065	0.13	0.05	0.13	0.00
S XV	5.102	0.22	0.05	0.22	0.00
Si XIII	5.405	0.12	0.04	0.12	0.00
Si XIV	6.183	-223	99	1490	242	0.26	0.03	0.26	0.00
Si XIII	6.648	-42	27	1457	58	1.62	0.07	1.64	0.00
Si XIII	6.687	0.53	0.05	0.53	0.00
Si XIII	6.740	1.14	0.05	1.15	0.00
Mg XII	8.422	-68	42	1439	114	1.16	0.06	1.19	0.01
Mg XI (r)	9.169	-54	27	1674	53	4.15	0.12	4.28	0.03
Mg XI (i)	9.230	1.91	0.10	1.97	0.01
Mg XI (f)	9.314	1.50	0.14	1.55	0.01
Ne X	9.362	0.42	0.06	0.43	0.00
Ne IX δ	9.481	0.49	0.05	0.51	0.00
Ne X γ	9.708	-109	68	1095	159	0.54	0.07	0.56	0.00
Ne X β	10.239	-187	42	1090	100	1.30	0.10	1.35	0.01
Ne X	12.135	-163	17	1683	31	16.95	0.37	17.99	0.22
Fe XVII	12.266	4.40	0.21	4.68	0.06
Fe XVII	15.014	-66	18	1985	38	47.79	0.95	52.33	0.99
O VIII γ	15.176	8.58	0.64	9.42	0.18
Fe XVII	15.261	24.41	0.86	26.83	0.53
O VIII β	16.006	22	37	2095	92	23.27	1.20	25.90	0.58
Fe XVIII	16.159	1.83	0.40	2.04	0.05
Fe XVII	16.780	-202	31	1524	63	22.13	0.97	24.98	0.64
Fe XVII	17.051	-195	24	1942	53	34.11	0.80	38.70	1.03

Table B17. ζ Ori B

Ion	λ_0	δv	$\sigma_{\delta v}$	$FWHM$	σ_{FW}	f_x	σ_{f_x}	f_0	σ_{f_0}
	(Å)	(km s ⁻¹)	(10 ⁻⁵ photon cm ⁻² s ⁻¹)						
Si XIII	6.648	-9	246	1511	534	0.09	0.03	0.09	0.00
Si XIII	6.687	0.05	0.02	0.05	0.00
Si XIII	6.740	0.06	0.02	0.06	0.00
Mg XII	8.422	-106	154	988	325	0.08	0.02	0.08	0.00
Mg XI (r)	9.169	112	76	891	155	0.27	0.04	0.28	0.00
Mg XI (i)	9.230	0.14	0.03	0.14	0.00
Ne X γ	9.708	0.06	0.03	0.06	0.00
Ne X β	10.239	-67	78	69	107	0.07	0.03	0.07	0.00
Ne X	12.135	-12	93	743	221	1.19	0.17	1.27	0.02
Fe XVII	12.266	0.19	0.08	0.20	0.00
Ne IX (r)	13.447	-76	106	1346	210	1.49	0.29	1.61	0.03
Ne IX (i)	13.552	1.32	0.25	1.43	0.02
Fe XVII	15.014	-6	50	726	119	3.65	0.46	4.00	0.08
Fe XVII	15.261	1.34	0.33	1.47	0.03
O VIII β	16.006	-67	100	706	166	1.57	0.36	1.74	0.04
Fe XVII	16.780	-20	64	467	180	2.09	0.49	2.36	0.06
Fe XVII	17.051	-204	90	721	216	2.77	0.43	3.14	0.08
O VII β	18.627	2.01	0.86	2.31	0.07
O VIII	18.970	6	73	937	180	9.65	1.50	11.19	0.35
O VII (r)	21.601	326	121	1020	180	10.29	2.00	12.67	0.55

Table B18. σ Ori Aa

Ion	λ_0	δv	$\sigma_{\delta v}$	$FWHM$	σ_{FW}	f_x	σ_{f_x}	f_0	σ_{f_0}
	(Å)	(km s ⁻¹)	(10 ⁻⁵ photon cm ⁻² s ⁻¹)						
Si XIII	6.648	-49	85	592	229	0.13	0.04	0.14	0.00
Si XIII	6.687	0.06	0.03	0.07	0.00
Si XIII	6.740	0.07	0.03	0.07	0.00
Mg XI (r)	9.169	-56	47	612	122	0.43	0.07	0.45	0.00
Mg XI (i)	9.230	0.38	0.06	0.40	0.00
Ne X γ	9.708	0.06	0.00	0.06	0.00
Ne X β	10.239	-152	70	74	139	0.20	0.06	0.21	0.00
Ne X	12.135	-114	32	567	90	2.32	0.24	2.52	0.03
Fe XVII	12.266	0.64	0.13	0.70	0.01
Ne IX (r)	13.447	-51	27	639	63	3.87	0.41	4.32	0.08
Ne IX (i)	13.552	3.73	0.41	4.17	0.08
Ne IX (f)	13.699	0.51	0.17	0.57	0.01
Fe XIX	13.795	0.45	0.18	0.51	0.01
Fe XVII	13.825	0.35	0.17	0.39	0.01
Fe XVII	15.014	8	32	836	67	8.02	0.73	9.12	0.19
O VIII γ	15.176	2.47	0.39	2.82	0.06
Fe XVII	15.261	3.78	0.48	4.32	0.09
O VIII β	16.006	2	44	480	98	3.41	0.53	3.97	0.10
Fe XVIII	16.071	0.53	0.26	0.62	0.02
Fe XVII	16.780	-141	29	294	88	5.00	0.70	5.94	0.17
Fe XVII	17.051	-74	23	354	56	7.43	0.66	8.89	0.26
O VII β	18.627	-53	61	379	61	2.27	0.62	2.77	0.09
O VIII	18.970	9	28	560	60	21.84	2.12	26.94	0.92
O VII (r)	21.601	57	40	773	84	19.93	2.92	26.74	1.28
O VII (i)	21.802	19.51	2.96	26.36	1.29
N VII α	24.782	2.85	1.22	3.63	0.14

Table B19. θ^1 Ori C

Ion	λ_0	δv	$\sigma_{\delta v}$	$FWHM$	σ_{FW}	f_x	σ_{f_x}	f_0	σ_{f_0}
	(Å)	(km s $^{-1}$)	(km s $^{-1}$)	(km s $^{-1}$)	(km s $^{-1}$)	(10 $^{-5}$ photon cm $^{-2}$ s $^{-1}$)			
Fe XXV	1.858	100	43	3466	104	8.13	0.18	8.17	0.01
Ar XVII (r)	3.949	-67	24	879	72	1.48	0.07	1.54	0.02
Ar XVII (i)	3.968	0.60	0.06	0.62	0.01
Ar XVII (f)	3.994	1.71	0.07	1.79	0.02
S XVI	4.730	-29	12	917	38	6.08	0.11	6.56	0.13
S XV	5.039	27	12	805	33	5.19	0.11	5.66	0.13
S XV	5.065	1.41	0.08	1.54	0.03
S XV	5.102	2.40	0.09	2.63	0.06
Si XIII β	5.681	46	35	815	112	1.21	0.08	1.36	0.04
Si XIV	6.183	-36	4	780	11	13.06	0.10	15.21	0.60
Si XIII	6.648	14	4	794	12	7.98	0.08	9.62	0.46
Si XIII	6.687	2.73	0.06	3.30	0.16
Si XIII	6.740	3.79	0.06	4.52	0.21
Mg XII	8.422	-43	4	660	13	7.76	0.08	10.75	0.91
Mg XI (r)	9.169	56	10	942	22	4.32	0.09	6.52	0.70
Mg XI (i)	9.230	2.76	0.08	4.19	0.46
Ne X	9.291	0.22	0.07	0.34	0.04
Mg XI (f)	9.314	0.27	0.07	0.41	0.05
Ne X	9.362	0.53	0.06	0.82	0.09
Ne IX δ	9.481	1.07	0.06	1.64	0.18
Ne X γ	9.708	41	34	1182	98	1.56	0.11	2.45	0.29
Ne X β	10.239	-23	12	499	38	2.00	0.08	3.37	0.46
Ne X	12.135	35	9	803	19	12.61	0.23	28.65	6.23
Fe XVII	12.266	3.89	0.15	9.05	2.03
Ne IX (r)	13.447	-548	52	1848	72	5.52	0.36	16.16	4.66
Ne IX (i)	13.552	9.74	0.42	29.12	8.59
Ne IX (f)	13.699	0.66	0.19	2.03	0.62
Fe XVII	13.825	2.79	0.32	8.83	2.75
Fe XVII	15.014	-18	15	807	42	9.59	0.38	33.57	11.42
Fe XIX	15.079	1.38	0.21	4.91	1.69
O VIII γ	15.176	1.03	0.21	3.75	1.32
Fe XVII	15.261	3.44	0.27	12.72	4.54
O VIII β	16.006	-19	27	614	69	3.22	0.27	14.17	5.78
Fe XVIII	16.071	1.92	0.22	8.59	3.55
Fe XIX	16.110	0.62	0.18	2.81	1.17
Fe XVII	16.780	-93	29	829	97	4.85	0.36	25.93	12.12
Fe XVII	17.051	-18	40	1353	140	5.78	0.34	33.15	16.23
O VII β	18.627	0.45	0.17	3.17	1.76
O VIII	18.970	24	41	1637	125	15.47	1.01	120.16	70.57
O VII (r)	21.601	13	160	1841	244	4.88	0.84	86.14	75.95
O VII (i)	21.802	5.32	0.88	100.62	91.44
O VII (f)	22.098	2.50	0.76	52.56	49.93
N VII α	24.782	2.37	0.94	25.37	17.67

Table B20. ι Ori

Ion	λ_0	δv	$\sigma_{\delta v}$	$FWHM$	σ_{FW}	f_x	σ_{f_x}	f_0	σ_{f_0}
	(Å)	(km s ⁻¹)	(10 ⁻⁵ photon cm ⁻² s ⁻¹)						
Si XIV	6.183	0.28	0.07	0.28	0.00
Si XIII	6.648	146	147	2035	277	0.70	0.13	0.71	0.00
Si XIII	6.687	0.30	0.12	0.30	0.00
Si XIII	6.740	0.75	0.12	0.76	0.00
Mg XII	8.422	-216	336	3016	1059	0.86	0.17	0.88	0.00
Ne X γ	9.708	0.41	0.12	0.42	0.00
Ne X β	10.239	149	180	1276	480	0.79	0.24	0.81	0.00
Ne X	12.135	-57	91	2364	161	9.50	0.69	9.87	0.09
Fe XVII	12.266	3.42	0.47	3.56	0.03
Ne IX (r)	13.447	950	250	3007	263	26.00	5.76	27.30	0.31
Ne IX (f)	13.699	2.73	1.00	2.87	0.03
Fe XVII	15.014	16	78	2525	160	27.88	2.19	29.52	0.40
O VIII γ	15.176	6.71	1.68	7.12	0.10
Fe XVII	15.261	16.61	1.77	17.63	0.25
O VIII β	16.006	52	203	3027	436	14.80	2.05	15.83	0.25
Fe XVII	16.780	2	113	2560	223	19.30	1.80	20.83	0.37
Fe XVII	17.051	72	72	2468	150	23.59	1.42	25.54	0.48
O VII β	18.627	-93	255	2846	582	10.98	1.99	12.00	0.25
O VIII	18.970	73	81	2255	201	100.40	6.98	110.22	2.42
O VII (r)	21.601	43	98	2251	158	87.59	5.31	99.83	3.07
N VII α	24.782	17	208	2474	518	31.38	5.34	34.96	0.89

Table B21. κ Ori

Ion	λ_0	δv	$\sigma_{\delta v}$	$FWHM$	σ_{FW}	f_x	σ_{f_x}	f_0	σ_{f_0}
	(Å)	(km s $^{-1}$)	(km s $^{-1}$)	(km s $^{-1}$)	(km s $^{-1}$)	(10 $^{-5}$ photon cm $^{-2}$ s $^{-1}$)			
S XV	5.039	0.07	0.03	0.07	0.00
Si XIV	6.183	0.06	0.02	0.06	0.00
Si XIII	6.648	125	65	1012	145	0.26	0.03	0.26	0.00
Si XIII	6.687	0.06	0.02	0.06	0.00
Si XIII	6.740	0.12	0.02	0.12	0.00
Mg XII	8.422	-100	146	966	342	0.09	0.02	0.09	0.00
Mg XI (r)	9.169	-31	62	1165	119	0.58	0.06	0.61	0.01
Mg XI (i)	9.230	0.32	0.05	0.34	0.00
Mg XI (f)	9.314	0.27	0.06	0.29	0.00
Ne X γ	9.708	0.24	0.07	0.25	0.00
Ne X β	10.239	-182	69	137	184	0.14	0.04	0.14	0.00
Ne X	12.135	-86	41	1211	86	2.22	0.16	2.45	0.04
Fe XVII	12.266	0.60	0.09	0.67	0.01
Ne IX (r)	13.447	-83	38	1359	77	5.40	0.39	6.15	0.15
Ne IX (i)	13.552	3.35	0.31	3.82	0.09
Ne IX (f)	13.699	0.97	0.16	1.12	0.03
Fe XIX	13.795	0.57	0.20	0.66	0.02
Fe XVII	15.014	-62	37	1124	89	6.56	0.49	7.63	0.21
O VIII γ	15.176	0.92	0.24	1.08	0.03
Fe XVII	15.261	3.60	0.39	4.22	0.12
O VIII β	16.006	-88	72	1280	219	3.37	0.51	4.03	0.13
Fe XVII	16.780	-168	57	1076	127	4.45	0.49	5.44	0.20
Fe XVII	17.051	-86	43	863	109	5.79	0.42	7.15	0.28
O VII β	18.627	85	116	1838	237	4.64	0.64	5.87	0.26
O VIII	18.970	-169	40	1342	83	28.87	1.71	36.93	1.69
O VII (r)	21.601	24	45	1396	78	33.40	2.83	47.17	3.03
O VII (i)	21.802	26.48	2.63	37.70	2.48
O VII (f)	22.098	3.46	1.08	4.98	0.34
N VII α	24.782	113	110	1926	218	19.13	2.38	25.43	1.34

Table B22. WR 6

Ion	λ_0	δv	$\sigma_{\delta v}$	$FWHM$	σ_{FW}	f_x	σ_{f_x}	f_0	σ_{f_0}
	(Å)	(km s ⁻¹)	(10 ⁻⁵ photon cm ⁻² s ⁻¹)						
Fe XXV	1.858	0.14	0.05	0.14	...
Ar XVII (r)	3.949	0.12	0.03	0.12	...
S XVI	4.730	0.16	0.05	0.16	...
Si XIV	6.183	-324	161	2744	385	0.29	0.03	0.32	...
Si XIII	6.648	-477	73	2793	121	1.02	0.07	1.12	...
Si XIII	6.687	0.33	0.07	0.37	...
Si XIII	6.740	0.91	0.06	0.99	...
Mg XII	7.106	154	298	3513	604	0.18	0.03	0.20	...
Mg XII	8.422	-379	137	2949	290	0.44	0.04	0.51	...
Mg XI (r)	9.169	-412	90	2686	155	1.18	0.09	1.44	...
Ne X	9.291	0.68	0.13	0.84	...
Ne X	9.362	0.23	0.06	0.28	...
Ne IX δ	9.481	0.20	0.04	0.25	...
Ne X γ	9.708	0.06	0.03	0.08	...
Ne X β	10.239	-1037	149	975	300	0.13	0.04	0.17	...
Ne IX β	11.544	-984	256	2134	679	0.26	0.09	0.38	...
Ne X	12.135	-571	147	2845	229	1.61	0.13	2.41	...
Fe XVII	12.266	0.58	0.10	0.88	...
Ne IX (r)	13.447	-1188	94	1300	218	0.80	0.15	1.35	...
Fe XIX	13.497	0.52	0.14	0.88	...
Ne IX (i)	13.552	0.61	0.12	1.04	...
Ne IX (f)	13.699	0.56	0.12	0.97	...
Fe XIX	13.795	0.59	0.16	1.03	...
Fe XVII	15.014	-497	101	2788	200	3.13	0.32	5.79	...
Fe XVII	15.261	1.57	0.26	2.98	...
Fe XVII	16.780	0.43	0.15	0.98	...
Fe XVII	17.051	-584	188	2066	541	0.98	0.21	2.32	...

Table B23. τ CMa

Ion	λ_0	δv	$\sigma_{\delta v}$	$FWHM$	σ_{FW}	f_x	σ_{f_x}	f_0	σ_{f_0}
	(Å)	(km s ⁻¹)	(10 ⁻⁵ photon cm ⁻² s ⁻¹)						
Si XIII	6.648	609	136	1434	259	0.11	0.02	0.11	0.00
Si XIII	6.740	0.09	0.02	0.09	0.00
Mg XII	8.422	-475	125	1102	289	0.09	0.02	0.10	0.00
Mg XI (r)	9.169	-429	146	1670	228	0.29	0.04	0.31	0.00
Mg XI (i)	9.230	0.25	0.04	0.27	0.00
Ne X	9.362	0.07	0.03	0.07	0.00
Ne IX δ	9.481	0.07	0.02	0.07	0.00
Ne X β	10.239	-56	230	1830	559	0.16	0.05	0.17	0.00
Ne X	12.135	25	86	1912	170	1.29	0.12	1.49	0.04
Fe XVII	12.266	0.43	0.08	0.50	0.01
Ne IX (r)	13.447	-129	120	1926	205	2.34	0.34	2.84	0.10
Ne IX (i)	13.552	1.56	0.25	1.90	0.07
Ne IX (f)	13.699	0.46	0.12	0.56	0.02
Fe XVII	13.825	0.47	0.16	0.58	0.02
Fe XVII	15.014	-76	86	2160	197	4.22	0.40	5.30	0.23
O VIII γ	15.176	0.92	0.27	1.17	0.05
Fe XVII	15.261	1.99	0.31	2.53	0.11
O VIII β	16.006	-1577	340	1987	597	0.78	0.34	1.03	0.05
Fe XIX	16.110	1.89	0.49	2.49	0.13
Fe XVII	16.780	-513	116	2200	483	1.98	0.41	2.68	0.15
O VII β	18.627	1.19	0.35	1.69	0.11
O VIII	18.970	-215	148	2235	302	17.62	2.04	25.58	1.78
O VII (r)	21.601	-18	213	2426	329	13.28	2.32	22.39	2.19
O VII (i)	21.802	11.39	2.23	19.44	1.95

Table B24. HD 42054

Ion	λ_0	δv	$\sigma_{\delta v}$	$FWHM$	σ_{FW}	f_x	σ_{f_x}	f_0	σ_{f_0}
	(Å)	(km s ⁻¹)	(10 ⁻⁵ photon cm ⁻² s ⁻¹)						
Fe XXV	1.858	1.21	0.23	1.21	...
Ar XVII (f)	3.994	0.12	0.05	0.12	...
S XVI	4.730	0.24	0.11	0.24	...
Si XIV	6.183	159	62	743	181	0.53	0.06	0.53	...
Si XIII	6.648	0.17	0.05	0.17	...
Mg XII	8.422	85	61	503	148	0.29	0.05	0.29	...
Ne X β	10.239	246	154	582	312	0.14	0.06	0.14	...
Ne X	12.135	131	159	1684	557	1.02	0.20	1.02	...
Fe XVII	12.266	0.42	0.14	0.42	...
Fe XVII	15.014	0.58	0.18	0.58	...
Fe XVII	16.780	222	184	1102	331	0.91	0.32	0.92	...
Fe XVII	17.051	0.67	0.20	0.68	...
O VIII	18.970	30	150	970	382	2.38	0.70	2.39	...

Table B25. ζ Pup

Ion	λ_0	δv	$\sigma_{\delta v}$	$FWHM$	σ_{FW}	f_x	σ_{f_x}	f_0	σ_{f_0}
	(Å)	(km s ⁻¹)	(10 ⁻⁵ photon cm ⁻² s ⁻¹)						
Ar XVII (r)	3.949	-129	199	1558	274	0.09	0.03	0.09	0.00
Ar XVII (i)	3.968	0.07	0.03	0.07	0.00
Ar XVII (f)	3.994	0.13	0.03	0.13	0.00
S XV	4.088	0.06	0.02	0.06	0.00
S XV	5.039	-184	43	1672	115	1.60	0.10	1.60	0.00
S XV	5.065	0.67	0.09	0.67	0.00
S XV	5.102	0.97	0.07	0.97	0.00
Si XIII β	5.681	-369	45	1720	155	0.88	0.06	0.88	0.00
Si XII	5.816	0.28	0.04	0.28	0.00
Si XIV	6.183	-398	36	1504	94	0.97	0.05	0.98	0.00
Si XIII	6.648	-361	17	1787	23	6.70	0.09	6.73	0.01
Si XIII	6.687	3.84	0.10	3.85	0.00
Si XIII	6.740	3.95	0.09	3.97	0.00
Mg XII	7.106	-422	47	1720	104	0.71	0.04	0.71	0.00
Al XIII	7.171	0.28	0.04	0.28	0.00
Mg XI	7.310	0.16	0.04	0.16	0.00
Mg XI γ	7.473	0.47	0.04	0.47	0.00
Al XII (r)	7.757	-506	53	1562	135	0.68	0.06	0.69	0.00
Al XII (i)	7.805	0.40	0.06	0.40	0.00
Mg XI	7.850	1.19	0.15	1.20	0.00
Al XII (f)	7.872	0.36	0.14	0.37	0.00
Mg XII	8.422	-452	20	1737	44	3.62	0.06	3.65	0.01
Mg XI (r)	9.169	-409	25	1944	33	11.80	0.18	11.93	0.02
Mg XI (i)	9.230	6.99	0.21	7.07	0.01
Mg XI (f)	9.314	3.18	0.13	3.21	0.01
Na X	9.433	0.54	0.10	0.55	0.00
Ne IX δ	9.481	0.64	0.09	0.65	0.00
Ne X γ	9.708	1.45	0.10	1.46	0.00
Ne X β	10.239	-644	27	1557	108	3.32	0.26	3.37	0.01
Fe XVIII	11.423	1.43	0.17	1.45	0.00
Fe XVIII	11.527	4.47	1.10	4.55	0.02
Ne X	12.135	-642	15	1769	27	25.43	0.45	25.97	0.10
Fe XVII	12.266	5.21	0.40	5.32	0.02
Ni XIX	12.435	2.64	0.22	2.70	0.01
Ne IX (r)	13.447	-424	28	1848	63	30.46	1.09	31.31	0.16
Fe XIX	13.518	12.27	1.26	12.62	0.07
Ne IX (i)	13.552	10.96	0.84	11.27	0.06
Fe XIX	13.645	2.83	0.53	2.91	0.02
Ne IX (f)	13.699	2.95	0.40	3.03	0.02
Fe XX	13.767	3.88	0.41	3.99	0.02
Fe XVII	13.825	5.75	0.52	5.92	0.03
Fe XVII	15.014	-519	25	1982	40	52.48	1.36	54.20	0.32
Fe XVII	15.261	-864	25	2878	98	32.66	1.24	33.78	0.21
Fe XVII	15.453	6.64	0.71	6.87	0.04
Fe XVIII	15.625	1.60	0.45	1.66	0.01
O VIII β	16.006	7.85	1.20	8.16	0.06
Fe XVIII	16.071	3.73	0.85	3.88	0.03
Fe XVII	16.780	-679	45	1998	64	27.51	1.29	28.72	0.23
Fe XVII	17.051	21.84	2.71	22.84	0.19
Fe XVII	17.096	19.44	2.74	20.34	0.17
O VII β	18.627	4.74	0.96	4.98	0.05
O VIII	18.970	-616	49	2340	106	45.15	2.37	47.59	0.46
N VII γ	19.826	4.17	1.20	4.43	0.05
N VII β	20.910	18.04	2.24	19.31	0.24
O VII (r)	21.602	-305	191	2613	260	36.78	5.04	39.59	0.54
O VII (i)	21.802	30.43	4.56	32.82	0.46
N VII α	24.782	-339	76	2810	152	90.69	5.24	96.38	1.08

Table B26. γ^2 Vel

Ion	λ_0	δv	$\sigma_{\delta v}$	<i>FWHM</i>	σ_{FW}	f_x	σ_{f_x}	f_0	σ_{f_0}
	(Å)	(km s ⁻¹)	(10 ⁻⁵ photon cm ⁻² s ⁻¹)						
Fe XXV	1.858	673	385	3367	963	2.35	0.48	2.35	0.00
Ar XVII (r)	3.949	1.27	0.26	1.28	0.00
Ar XVII (i)	3.968	0.67	0.23	0.67	0.00
Ar XVII (f)	3.994	1.19	0.27	1.19	0.00
S XVI	4.730	82	107	1433	305	3.37	0.42	3.37	0.00
S XV	5.039	8.90	0.73	8.91	0.00
S XV	5.065	3.04	0.60	3.04	0.00
S XV	5.102	4.86	0.49	4.87	0.00
Si XIII β	5.681	2.64	0.39	2.64	0.00
Si XIV	6.183	-8	31	1298	73	9.12	0.38	9.14	0.00
Si XIII	6.648	-51	21	1349	45	13.82	0.47	13.86	0.01
Si XIII	6.687	3.84	0.32	3.85	0.00
Si XIII	6.740	9.28	0.35	9.31	0.00
Mg XII	8.422	-93	40	1186	94	5.33	0.33	5.36	0.00
Mg XI (r)	9.169	-63	64	1510	117	4.07	0.30	4.10	0.00
Mg XI (i)	9.230	1.39	0.23	1.40	0.00
Mg XI (f)	9.314	1.29	0.33	1.30	0.00
Ne IX δ	9.481	0.61	0.17	0.61	0.00
Ne X γ	9.708	173	152	1194	312	0.69	0.18	0.70	0.00
Ne X β	10.239	102	88	906	235	1.12	0.21	1.13	0.00
Ne X	12.135	64	385	1536	193	2.93	0.33	2.97	0.01
Ne IX (r)	13.447	1.55	0.31	1.58	0.00
Ne IX (i)	13.552	0.43	0.19	0.44	0.00
Ne IX (f)	13.699	1.03	0.27	1.05	0.00
O VII β	18.627	1.01	0.49	1.04	0.00
O VIII	18.970	1.33	0.53	1.38	0.01

Table B27. RCW 38 IRS 2

Ion	λ_0	δv	$\sigma_{\delta v}$	<i>FWHM</i>	σ_{FW}	f_x	σ_{f_x}	f_0	σ_{f_0}
	(Å)	(km s ⁻¹)	(10 ⁻⁵ photon cm ⁻² s ⁻¹)						
S XV	5.039	819	223	1715	573	0.37	0.10	0.53	-0.06
Si XIII β	5.681	0.15	0.06	0.24	-0.04
Si XIV	6.183	-250	237	2819	611	0.41	0.06	0.76	-0.14
Si XIII	6.648	224	417	3431	527	0.80	0.25	1.70	-0.36
Si XIII	6.740	0.24	0.08	0.50	-0.10
Mg XII	8.422	-620	282	2982	681	0.25	0.05	0.93	-0.26
Mg XI (i)	9.230	0.33	0.09	1.77	-0.53
Ne X	12.135	-665	336	3462	1144	0.24	0.09	6.65	-1.95

Table B28. HD 93129A

Ion	λ_0	δv	$\sigma_{\delta v}$	$FWHM$	σ_{FW}	f_x	σ_{f_x}	f_0	σ_{f_0}
	(Å)	(km s ⁻¹)	(10 ⁻⁵ photon cm ⁻² s ⁻¹)						
S XV	5.102	0.15	0.06	0.16	...
Si XIII β	5.681	0.12	0.05	0.13	...
Si XIII	6.648	-600	200	2676	343	0.82	0.15	0.95	...
Si XIII	6.687	0.62	0.13	0.72	...
Si XIII	6.740	0.57	0.10	0.66	...
Mg XII	8.422	-873	209	3386	774	0.53	0.11	0.68	...
Mg XI (r)	9.169	-860	213	2881	446	1.02	0.22	1.40	...
Mg XI (i)	9.230	0.67	0.21	0.93	...
Ne X	9.362	0.25	0.08	0.35	...
Ne X	12.135	-578	214	3953	552	1.73	0.23	3.30	...
Fe XVII	12.266	0.61	0.19	1.18	...

Table B29. HD 93250

Ion	λ_0	δv	$\sigma_{\delta v}$	$FWHM$	σ_{FW}	f_x	σ_{f_x}	f_0	σ_{f_0}
	(Å)	(km s ⁻¹)	(10 ⁻⁵ photon cm ⁻² s ⁻¹)						
Fe XXV	1.858	0.30	0.11	0.30	0.00
S XV	5.039	0.16	0.06	0.17	0.00
Si XIV	6.183	-132	264	3692	482	0.43	0.06	0.48	0.02
Si XIII	6.648	129	496	3615	585	0.65	0.22	0.74	0.03
Si XIII	6.740	0.21	0.07	0.24	0.01
Mg XII	8.422	0.72	0.10	0.91	0.08
Mg XI (r)	9.169	-737	342	2485	683	0.57	0.16	0.76	0.08
Mg XI (i)	9.230	0.40	0.13	0.53	0.06
Ne X	9.291	0.32	0.09	0.44	0.05
Ne IX δ	9.481	0.16	0.06	0.22	0.02
Ne X	12.135	-1275	177	2190	241	1.19	0.18	2.12	0.45
Fe XVII	12.266	1.10	0.18	2.01	0.44
Ne IX (r)	13.447	-517	315	2227	446	1.18	0.57	2.51	0.71
Ne IX (i)	13.552	0.89	0.44	1.94	0.56
Fe XVII	15.014	-168	174	3339	313	3.49	0.38	8.45	2.84
Fe XVII	15.261	1.26	0.24	3.16	1.11
O VIII β	16.006	0.37	0.17	1.05	0.42
Fe XVII	17.051	280	294	3283	688	0.98	0.21	3.35	1.63
O VIII	18.970	-736	382	1903	708	1.21	0.55	5.15	3.01

Table B30. WR 25

Ion	λ_0	δv	$\sigma_{\delta v}$	$FWHM$	σ_{FW}	f_x	σ_{f_x}	f_0	σ_{f_0}
	(Å)	(km s ⁻¹)				(10 ⁻⁵ photon cm ⁻² s ⁻¹)			
Fe XXV	1.858	1.64	0.38	1.64	0.00
Ar XVII (r)	3.949	-56	238	1595	497	0.69	0.18	0.73	0.01
Ar XVII (f)	3.994	0.62	0.17	0.65	0.01
S XVI	4.730	163	215	2915	476	2.55	0.35	2.76	0.07
S XV	5.039	-278	311	2453	446	2.62	0.68	2.86	0.08
S XV	5.102	1.44	0.34	1.58	0.04
Si XIII β	5.681	-266	327	2576	731	1.18	0.28	1.34	0.05
Si XIV	6.183	-264	65	2340	149	4.83	0.26	5.65	0.27
Si XIII	6.648	-243	67	2303	135	5.49	0.37	6.64	0.39
Si XIII	6.687	0.96	0.33	1.17	0.07
Si XIII	6.740	2.97	0.23	3.56	0.20
Mg XII	8.422	-332	80	2160	198	3.73	0.31	5.20	0.54
Mg XI (r)	9.169	-291	133	1986	275	3.20	0.37	4.87	0.64
Ne X γ	9.708	0.88	0.21	1.40	0.20
Ne X β	10.239	1.23	0.21	2.10	0.35
Ne X	12.135	-388	128	2569	292	6.33	0.60	14.66	3.93
Fe XVII	12.266	2.72	0.47	6.45	1.78
Fe XXI	12.393	2.79	0.48	6.77	1.93
Ne IX (r)	13.447	-526	147	1695	247	2.99	0.68	8.97	3.21
Ne IX (i)	13.552	2.77	0.70	8.51	3.11
Ne IX (f)	13.699	1.69	0.51	5.37	2.02
Fe XVII	13.825	0.94	0.45	3.05	1.18
Fe XVII	15.014	-465	228	2627	456	6.35	1.15	22.88	9.70
Fe XVII	15.261	1.44	0.61	5.50	2.44
O VIII β	16.006	1.55	0.68	7.06	3.61

Table B31. θ Car

Ion	λ_0	δv	$\sigma_{\delta v}$	$FWHM$	σ_{FW}	f_x	σ_{f_x}	f_0	σ_{f_0}
	(Å)	(km s ⁻¹)	(10 ⁻⁵ photon cm ⁻² s ⁻¹)						
Si XIII	6.648	0.18	0.04	0.18	0.00
Si XIII	6.687	0.04	0.02	0.04	0.00
Si XIII	6.740	0.10	0.03	0.11	0.00
Mg XII	8.422	0.12	0.03	0.13	0.00
Mg XI (r)	9.169	103	47	523	119	0.48	0.07	0.49	0.00
Mg XI (i)	9.230	0.32	0.06	0.32	0.00
Mg XI (f)	9.314	0.11	0.04	0.11	0.00
Ne X β	10.239	-38	184	832	391	0.16	0.06	0.16	0.00
Ne X	12.135	2.45	0.27	2.56	0.02
Fe XVII	12.266	0.57	0.14	0.60	0.01
Ne IX (r)	13.447	33	37	470	95	1.87	0.34	1.98	0.02
Ne IX (i)	13.552	2.72	0.44	2.89	0.03
Fe XVII	13.825	0.52	0.22	0.55	0.01
Fe XVII	15.014	30	32	482	85	7.56	0.82	8.10	0.10
Fe XVII	15.261	1.53	0.47	1.65	0.02
O VIII β	16.006	1.25	0.42	1.36	0.02
Fe XVIII	16.071	0.89	0.37	0.97	0.01
Fe XVII	16.780	-86	40	216	166	4.78	0.98	5.24	0.09
Fe XVII	17.051	42	55	498	127	6.32	0.85	6.95	0.12
O VIII	18.970	183	56	318	117	10.98	2.00	12.29	0.26
O VII (r)	21.601	10.76	2.82	12.60	0.37
N VII α	24.782	18	48	379	116	25.09	5.72	28.59	0.69

Table B32. HD 110432

Ion	λ_0	δv	$\sigma_{\delta v}$	$FWHM$	σ_{FW}	f_x	σ_{f_x}	f_0	σ_{f_0}
	(Å)	(km s ⁻¹)	(10 ⁻⁵ photon cm ⁻² s ⁻¹)						
Fe XXVI	1.781	170	262	2583	692	5.38	0.29	5.41	...
Fe XXV	1.858	-226	244	3192	524	6.59	0.80	6.63	...
Ar XVII (f)	3.994	0.82	0.27	0.86	...
S XVI	4.730	-87	203	1599	481	1.76	0.32	1.90	...
S XV	5.065	0.50	0.21	0.55	...
Si XIII β	5.681	0.64	0.31	0.72	...
Si XIV	6.183	89	66	1249	206	1.99	0.19	2.30	...
Si XIII	6.648	0.46	0.12	0.55	...
Si XIII	6.687	0.24	0.12	0.29	...
Mg XII	8.422	176	107	1152	227	0.72	0.11	0.99	...
Mg XI (r)	9.169	0.21	0.08	0.31	...
Ne X	12.135	0.35	0.13	0.76	...
Fe XVII	15.014	-84	188	1121	357	0.45	0.18	1.48	...
Fe XVII	15.261	0.37	0.17	1.29	...

Table B33. β Cru

Ion	λ_0	δv	$\sigma_{\delta v}$	$FWHM$	σ_{FW}	f_x	σ_{f_x}	f_0	σ_{f_0}
	(Å)	(km s $^{-1}$)	(km s $^{-1}$)	(km s $^{-1}$)	(km s $^{-1}$)	(10 $^{-5}$ photon cm $^{-2}$ s $^{-1}$)			
Si XIII	6.648	0.10	0.04	0.10	...
Si XIII	6.740	0.07	0.03	0.07	...
Mg XI (r)	9.169	0.25	0.06	0.25	...
Mg XI (i)	9.230	0.22	0.05	0.22	...
Mg XI (f)	9.314	0.13	0.04	0.13	...
Ne X	12.135	-30	41	529	113	1.46	0.21	1.47	...
Fe XVII	12.266	0.55	0.14	0.56	...
Ne IX (r)	13.447	-7	19	329	58	4.25	0.46	4.30	...
Ne IX (i)	13.552	3.68	0.43	3.72	...
Ne IX (f)	13.699	0.35	0.16	0.35	...
Fe XVII	13.825	0.74	0.22	0.75	...
Fe XVII	15.014	8	28	338	111	6.37	0.80	6.45	...
O VIII γ	15.176	1.03	0.37	1.05	...
Fe XVII	15.261	3.10	0.53	3.15	...
O VIII β	16.006	3.89	0.57	3.95	...
Fe XVIII	16.071	0.86	0.28	0.87	...
Fe XVII	16.780	-63	32	69	76	3.68	0.63	3.75	...
Fe XVII	17.051	-49	25	352	67	7.56	0.70	7.70	...
O VII β	18.627	18	73	515	187	2.92	0.73	2.98	...
O VIII	18.970	-49	21	394	53	29.77	2.58	30.39	...
O VII (r)	21.601	-33	15	310	42	44.59	3.31	45.90	...
N VII α	24.782	10.02	2.32	10.26	...

Table B34. HD 148937

Ion	λ_0 (Å)	δv	$\sigma_{\delta v}$	$FWHM$	σ_{FW}	f_x	σ_{f_x}	f_0	σ_{f_0}
								(10 ⁻⁵ photon cm ⁻² s ⁻¹)	
Fe XXV	1.858	0.64	0.20	0.64	0.00
Ar XVII (r)	3.949	0.28	0.14	0.29	0.00
Ar XVII (f)	3.994	0.29	0.14	0.31	0.00
S XVI	4.730	0.52	0.13	0.56	0.01
S XV	5.039	118	135	1228	450	1.04	0.20	1.14	0.03
S XV	5.102	0.55	0.15	0.61	0.01
Si XIV	6.183	-46	46	830	127	1.42	0.12	1.70	0.07
Si XIII	6.648	97	42	940	103	1.62	0.13	2.01	0.10
Si XIII	6.687	0.74	0.10	0.92	0.05
Si XIII	6.740	0.62	0.08	0.76	0.04
Mg XII	8.422	-18	38	762	118	1.47	0.12	2.13	0.19
Mg XI (r)	9.169	38	78	1250	148	1.41	0.17	2.27	0.25
Mg XI (i)	9.230	0.93	0.15	1.51	0.17
Ne X	9.291	0.27	0.12	0.44	0.05
Ne X	9.362	0.20	0.10	0.33	0.04
Ne X β	10.239	-26	116	537	424	0.35	0.12	0.64	0.09
Ne X	12.135	-136	77	1709	153	4.51	0.39	11.57	2.61
Fe XVII	12.266	1.73	0.27	4.55	1.06
Ne IX (r)	13.447	-328	194	1521	379	1.72	0.53	5.90	1.77
Ne IX (i)	13.552	2.45	0.59	8.61	2.64
Fe XVII	15.014	-134	136	1860	330	5.25	0.89	22.09	7.81
O VIII γ	15.176	1.24	0.51	5.45	1.99
O VIII β	16.006	0.64	0.31	3.48	1.48
Fe XVII	16.780	-281	101	517	233	1.41	0.47	9.61	4.67
Fe XVII	17.051	-302	251	3275	1003	5.09	1.79	37.71	19.19
O VIII	18.970	17	205	1765	331	4.67	1.19	49.00	29.93

Table B35. HD 150135

Ion	λ_0 (Å)	δv (km s ⁻¹)	$\sigma_{\delta v}$ (km s ⁻¹)	$FWHM$ (km s ⁻¹)	σ_{FW} (km s ⁻¹)	f_x	σ_{f_x}	f_0	σ_{f_0}	(10 ⁻⁵ photon cm ⁻² s ⁻¹)
S XV	5.039	0.05	0.02	0.06
Si XIV	6.183	-182	202	1521	471	0.06	0.01	0.08
Si XIII	6.648	-24	206	1856	319	0.15	0.03	0.19
Si XIII	6.740	0.08	0.02	0.10
Mg XII	8.422	-201	240	2118	671	0.12	0.03	0.17
Mg XI (r)	9.169	817	319	3628	673	0.39	0.09	0.62
Ne X	9.362	0.25	0.05	0.42
Ne X γ	9.708	-517	153	1083	324	0.12	0.03	0.21
Ne X β	10.239	-539	337	2777	1028	0.25	0.11	0.45
Ne X	12.135	44	122	2157	236	1.00	0.11	2.56
Fe XVII	12.266	0.28	0.08	0.75
Ne IX (r)	13.447	459	222	2582	436	1.32	0.25	4.52
Ne IX (i)	13.552	0.52	0.20	1.84
Ne IX (f)	13.699	0.55	0.20	2.02
Fe XVII	15.014	-505	106	1499	233	1.16	0.24	4.88
Fe XIX	15.079	0.47	0.21	2.01
O VIII γ	15.176	0.38	0.17	1.68
Fe XVII	15.261	1.27	0.22	5.68
O VIII β	16.006	-294	81	363	294	0.39	0.14	2.12
Fe XVII	16.780	0.56	0.17	3.84
Fe XVII	17.051	1.02	0.17	7.60
O VIII	18.970	5.14	1.49	53.97
O VII (r)	21.601	2.31	0.63	62.32
O VII (f)	22.098	2.49	1.08	81.63

Table B36. HD 150136

Ion	λ_0	δv	$\sigma_{\delta v}$	$FWHM$	σ_{FW}	f_x	σ_{f_x}	f_0	σ_{f_0}
	(Å)	(km s ⁻¹)	(10 ⁻⁵ photon cm ⁻² s ⁻¹)						
S XV	5.039	385	142	2221	280	1.16	0.16	1.29	...
S XV	5.102	0.52	0.09	0.57	...
Si XIV β	5.217	0.30	0.07	0.33	...
Si XIV	6.183	-75	57	2190	124	1.39	0.07	1.66	...
Si XIII	6.648	-41	54	2707	91	4.15	0.19	5.16	...
Si XIII	6.687	1.16	0.17	1.44	...
Si XIII	6.740	1.90	0.09	2.33	...
Mg XII	8.422	-288	42	2608	108	2.86	0.09	4.20	...
Mg XI (r)	9.169	-418	93	2623	130	3.98	0.28	6.44	...
Mg XI (i)	9.230	2.99	0.24	4.88	...
Ne X	9.291	0.99	0.15	1.63	...
Ne X	9.362	1.02	0.13	1.70	...
Ne IX δ	9.481	0.93	0.09	1.53	...
Ne X γ	9.708	1.74	0.15	2.96	...
Ne X β	10.239	-468	116	2189	348	1.22	0.20	2.26	...
Ne X	12.135	-311	41	2806	78	12.51	0.35	32.75	...
Fe XXI	12.284	4.79	0.25	12.94	...
Fe XIX	13.497	17.22	4.71	61.43	...
Fe XIX	13.795	6.52	2.33	25.06	...
Fe XVII	15.014	-311	60	3427	119	18.72	0.70	81.43	...
Fe XVII	15.261	11.01	0.71	51.09	...
O VIII β	16.006	-142	381	3832	722	7.26	2.93	41.31	...
Fe XVII	16.780	-318	121	2744	258	6.79	0.60	48.47	...
Fe XVII	17.051	-425	187	3624	494	7.91	0.96	61.36	...
O VIII	18.970	-130	180	2621	422	15.83	2.08	175.27	...
O VII (r)	21.601	6.04	0.85	175.21	...
N VII α	24.782	1.31	0.63	21.09	...

Table B37. τ Sco

Ion	λ_0	δv	$\sigma_{\delta v}$	$FWHM$	σ_{FW}	f_x	σ_{f_x}	f_0	σ_{f_0}
	(Å)	(km s $^{-1}$)	(km s $^{-1}$)	(km s $^{-1}$)	(km s $^{-1}$)	(10 $^{-5}$ photon cm $^{-2}$ s $^{-1}$)			
S XVI	4.730	0.54	0.16	0.55	0.00
S XV	5.039	1.01	0.19	1.02	0.00
S XV	5.065	0.37	0.13	0.37	0.00
S XV	5.102	0.90	0.18	0.90	0.00
Si XIV	6.183	37	30	500	97	2.19	0.16	2.22	0.01
Si XIII	6.648	75	14	412	50	4.09	0.22	4.16	0.01
Si XIII	6.687	1.32	0.14	1.34	0.00
Si XIII	6.740	2.76	0.17	2.81	0.01
Mg XII	8.422	25	23	575	68	4.02	0.26	4.14	0.02
Mg XI (r)	9.169	87	16	695	43	6.76	0.32	7.01	0.05
Mg XI (i)	9.230	3.48	0.24	3.61	0.02
Ne X	9.291	0.68	0.15	0.71	0.00
Mg XI (f)	9.314	1.34	0.18	1.39	0.01
Ne X	9.362	0.48	0.12	0.50	0.00
Ne IX δ	9.481	1.41	0.17	1.46	0.01
Ne X γ	9.708	56	48	709	134	1.78	0.20	1.85	0.01
Ne X β	10.239	-53	32	331	116	1.96	0.23	2.05	0.02
Ne X	12.135	-10	11	665	29	26.92	0.90	28.91	0.38
Fe XVII	12.266	4.84	0.66	5.21	0.07
Fe XXI	12.284	7.73	0.73	8.32	0.11
Ne IX (r)	13.447	25	22	660	44	15.99	0.96	17.56	0.30
Fe XIX	13.497	7.14	0.81	7.85	0.14
Ne IX (i)	13.552	16.95	1.12	18.65	0.33
Fe XIX	13.795	3.09	0.68	3.42	0.06
Fe XVII	13.825	4.43	0.70	4.89	0.09
Fe XVII	15.014	42	11	465	31	46.35	1.93	51.69	1.05
Fe XIX	15.079	10.14	0.95	11.32	0.23
O VIII γ	15.176	8.63	0.82	9.65	0.20
Fe XVII	15.261	21.62	1.19	24.23	0.51
O VIII β	16.006	4	14	397	35	17.93	1.19	20.40	0.49
Fe XVIII	16.071	10.89	0.97	12.41	0.30
Fe XIX	16.110	3.88	0.65	4.43	0.11
Fe XVII	16.780	-52	12	299	36	30.94	1.72	35.80	0.97
Fe XVII	17.051	7	9	337	23	38.30	2.03	44.59	1.26
Fe XVII	17.096	37.14	1.99	43.28	1.23
O VII β	18.627	3.08	0.75	3.65	0.12
O VIII	18.970	-27	15	573	35	75.05	3.88	89.71	2.98
O VII (r)	21.601	14	17	473	43	34.29	3.55	44.03	2.05
O VII (i)	21.802	47.07	4.27	60.80	2.90
N VII α	24.782	-21	29	500	64	32.68	3.65	40.17	1.54

C. SPECTRAL PLOTS FOR EACH STAR

We show each spectrum as luminosity density on two scales. Panel A in each pair uses a logarithmic y -axis scaling which is useful to convey the overall shape of the spectrum. All logarithmic y -ranges span 3 dex. Panel B of the pair has a linear scale to emphasize the emission lines, auto-scaled from zero to the maximum flux in the range plotted. In each plot, the black curve is uncorrected for interstellar absorption, and the gray curve is the corrected version. Some of these are apparently over-corrected with the absorption values adopted from the literature (see Table 2). Plots are in the same order as given in Table 2. The plot captions give the observed fluxes (uncorrected for absorption, corresponding to the black curve), and the absorption corrected luminosity (corresponding to the gray curves), along with the N_{H} and distances from Table 2.

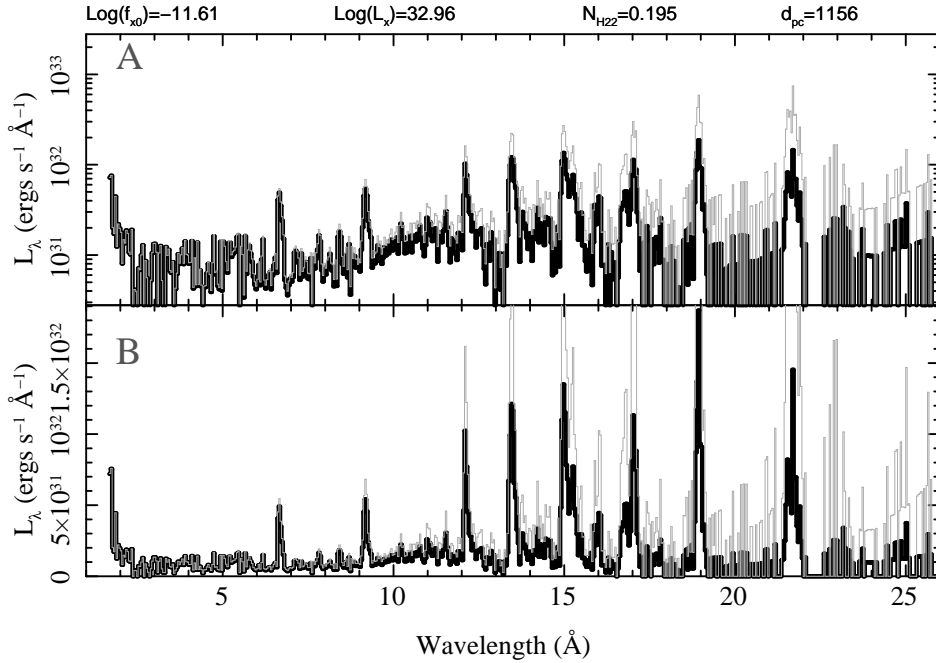


Figure C1. 9 Sgr

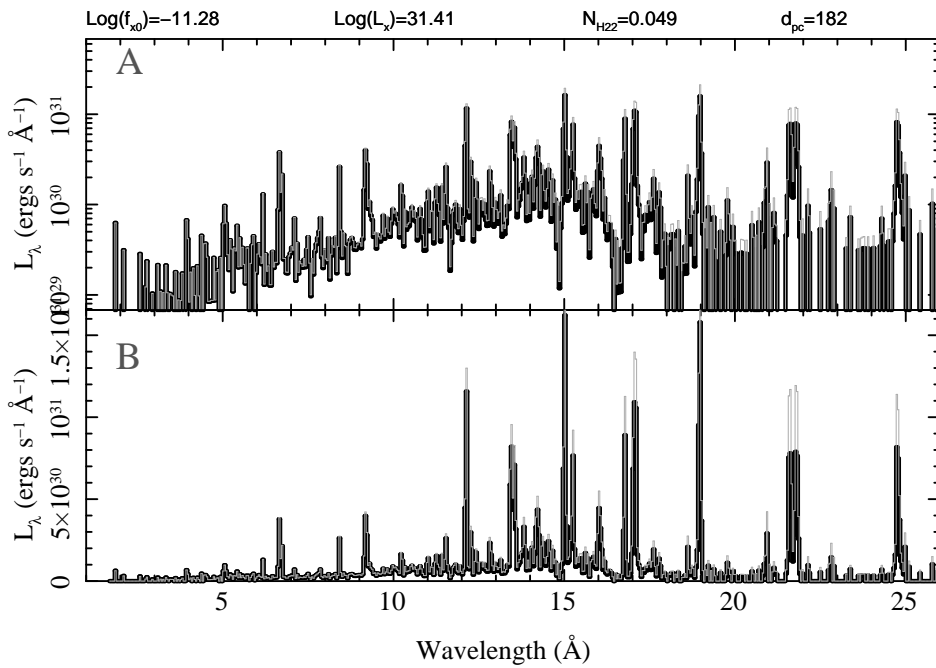


Figure C2. ζ Oph

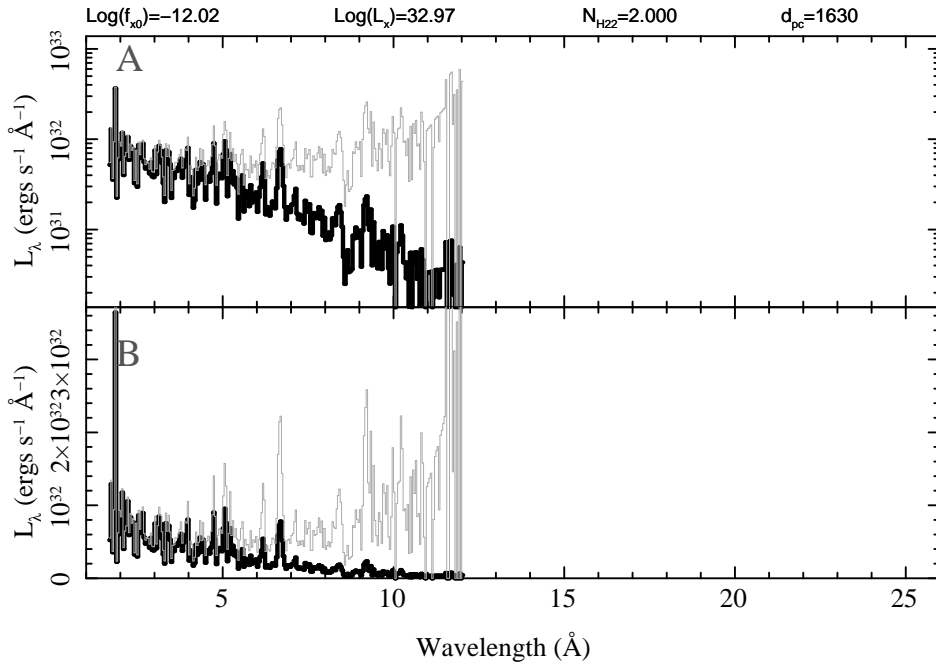


Figure C3. M17 Cen 1B

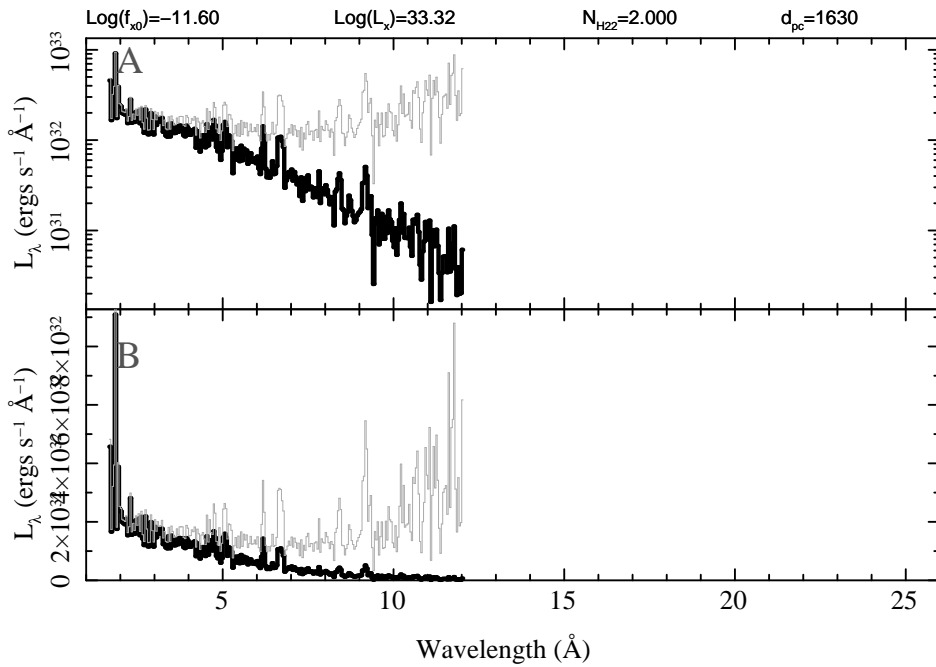


Figure C4. M17 Cen 1A

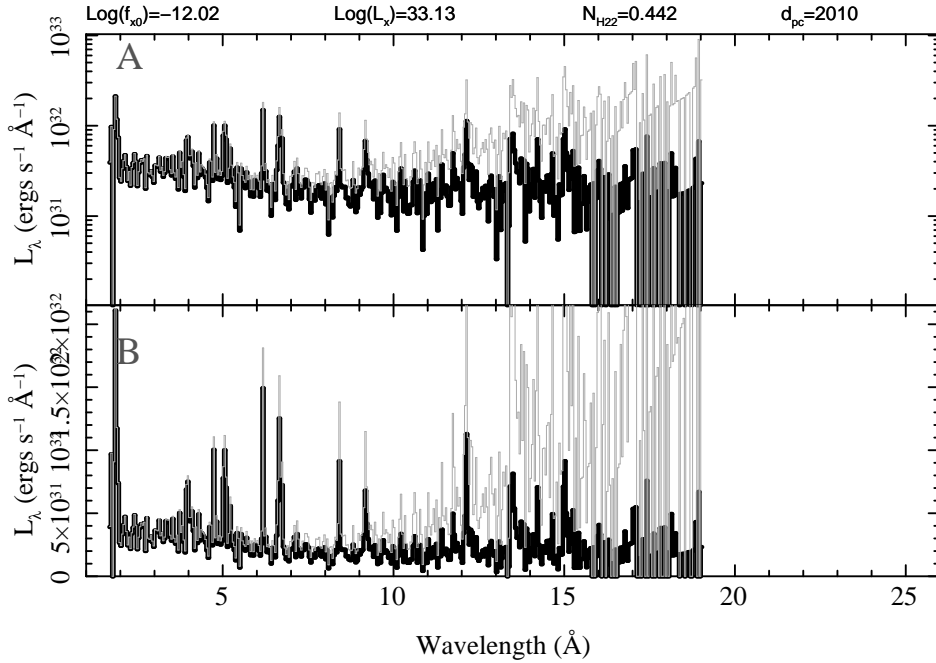


Figure C5. HD 191612

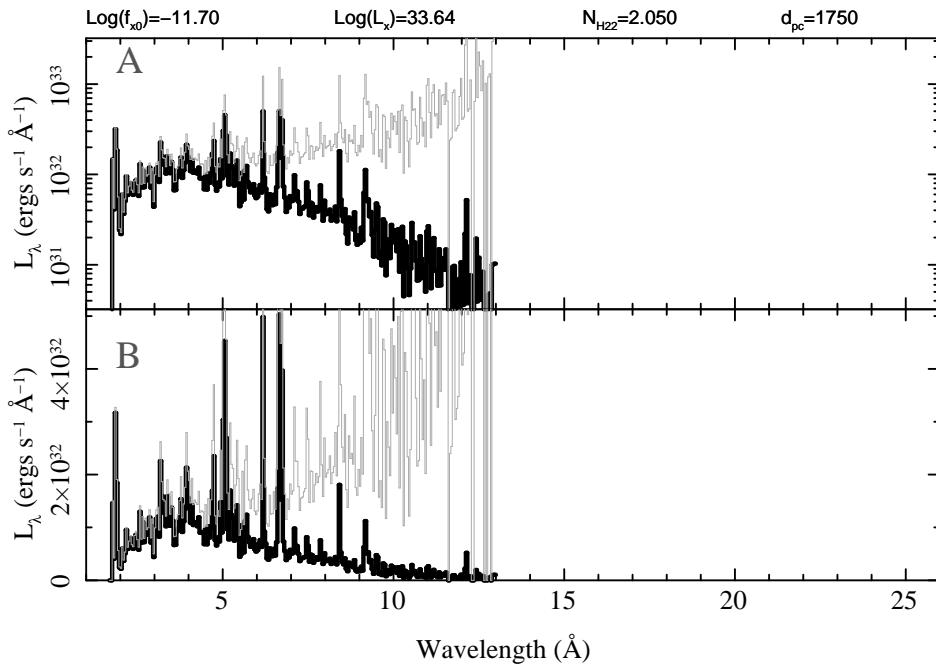
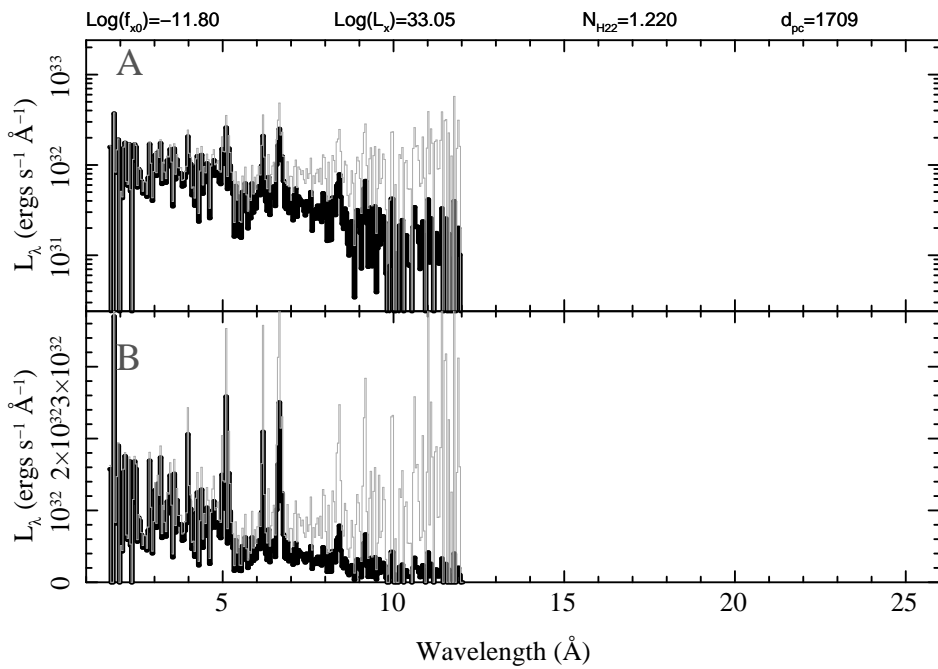
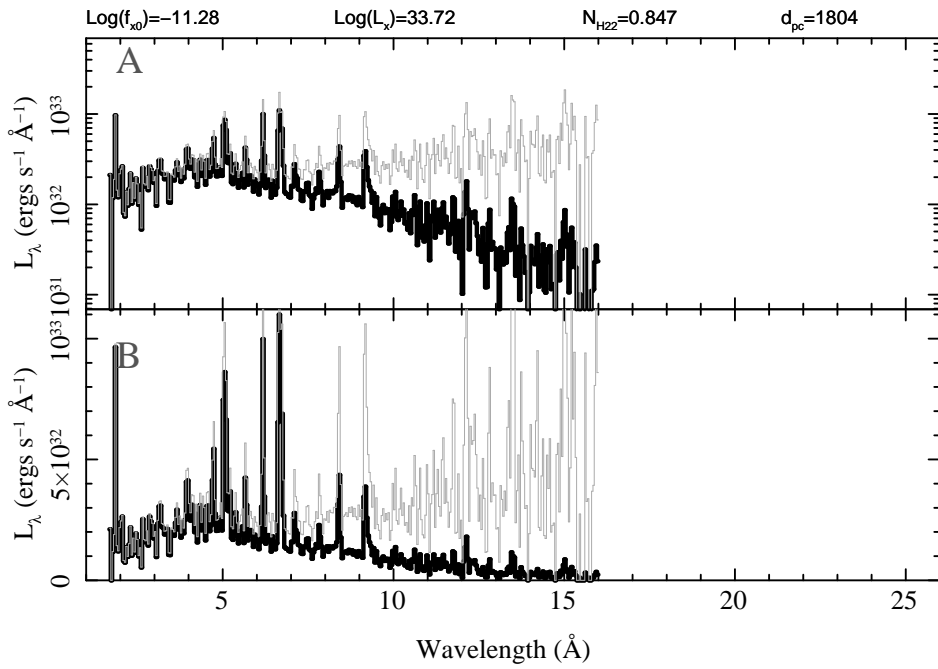


Figure C6. Cyg OB2-12

**Figure C7.** Cyg OB2-9**Figure C8.** Cyg OB2-8A

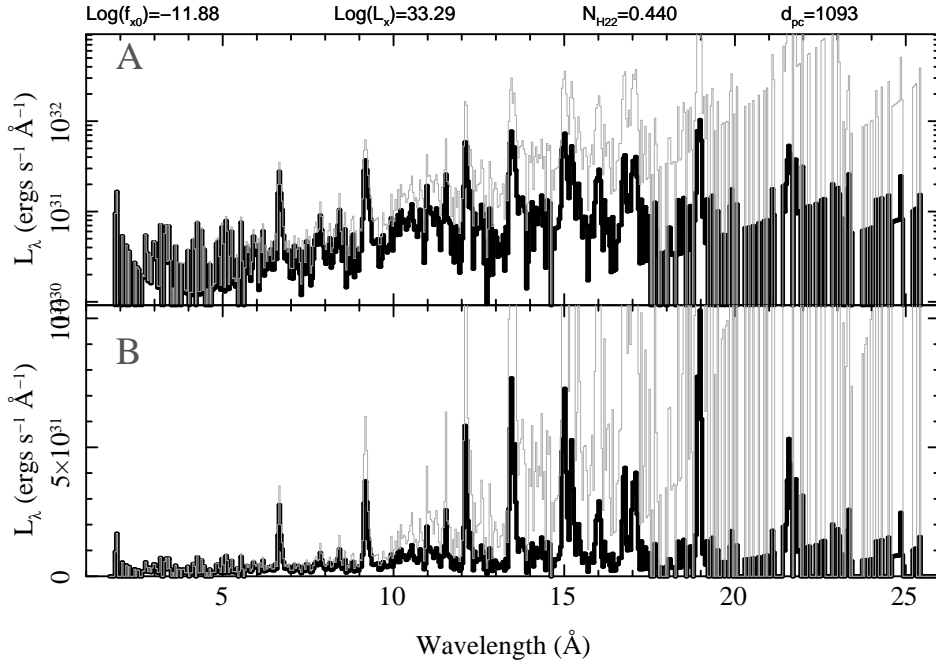


Figure C9. HD 206267

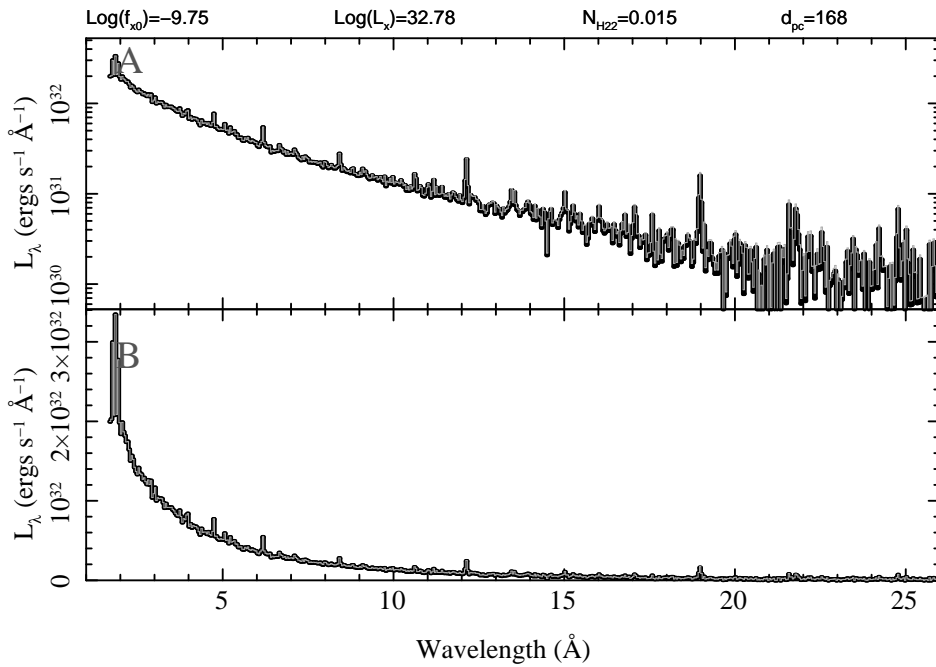
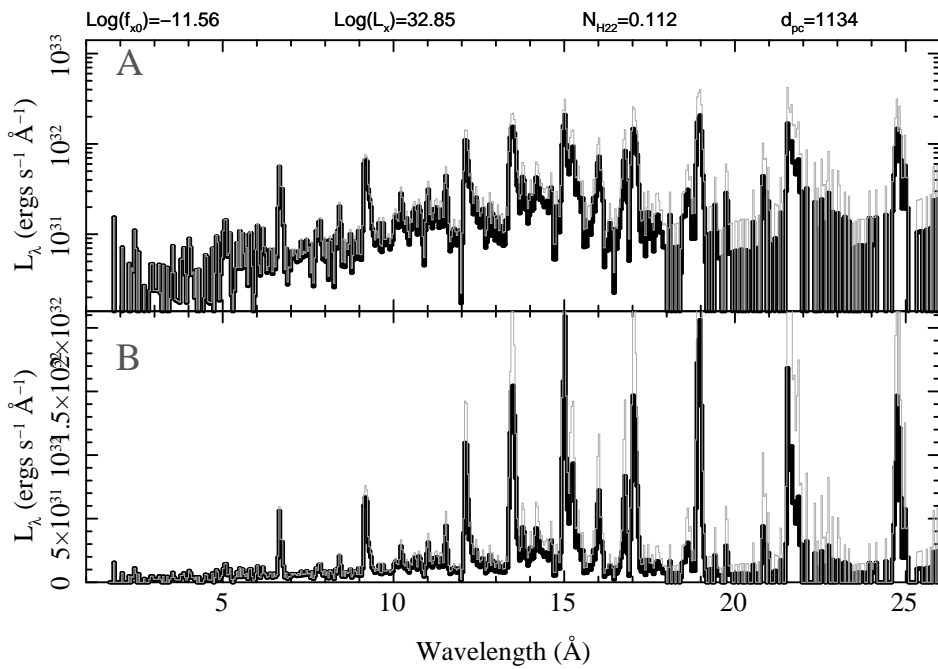
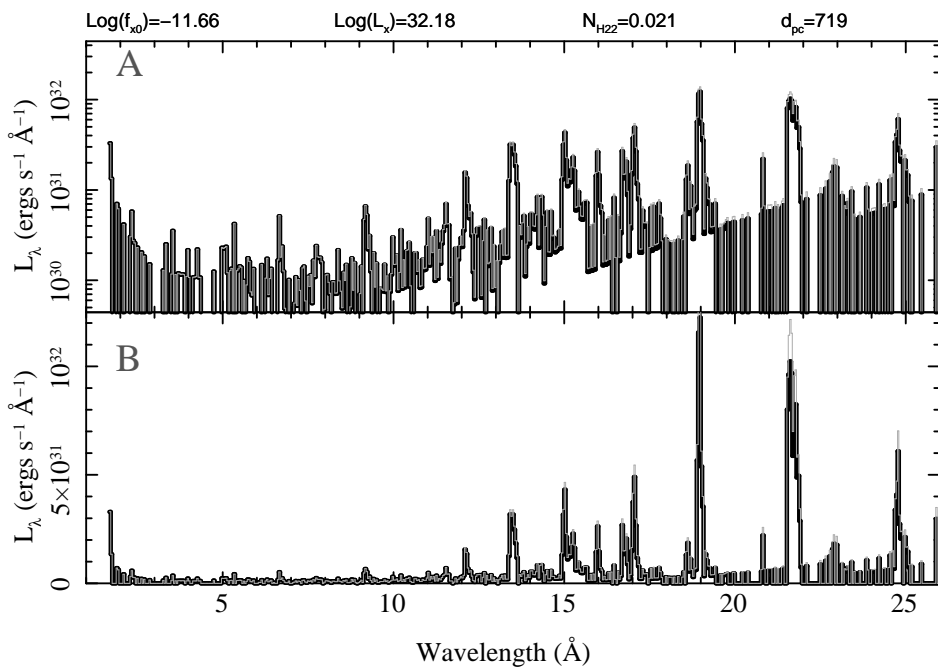


Figure C10. γ Cas

**Figure C11.** ξ Per**Figure C12.** 15 Mon

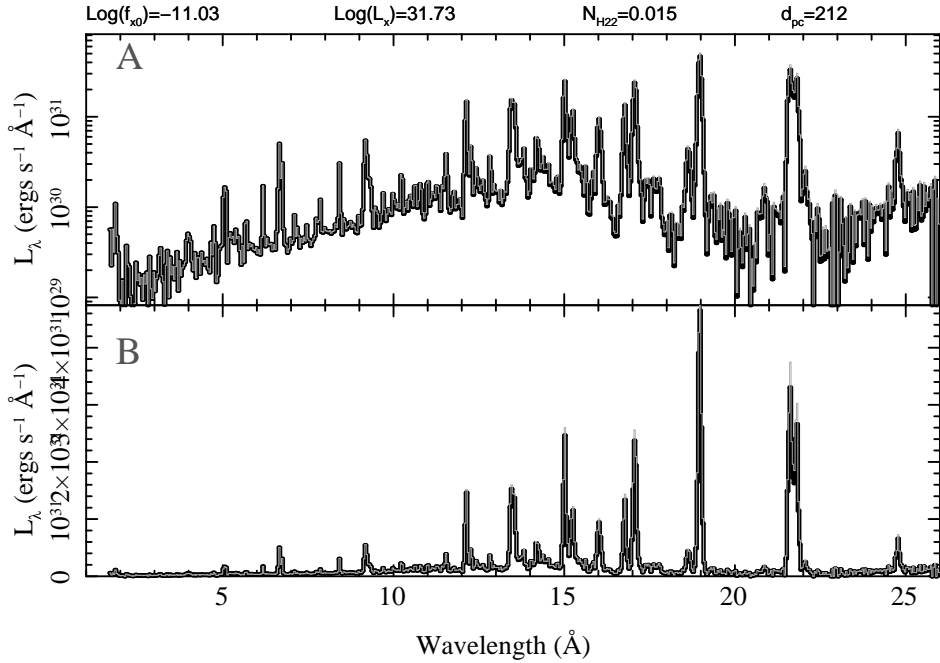


Figure C13. δ Ori

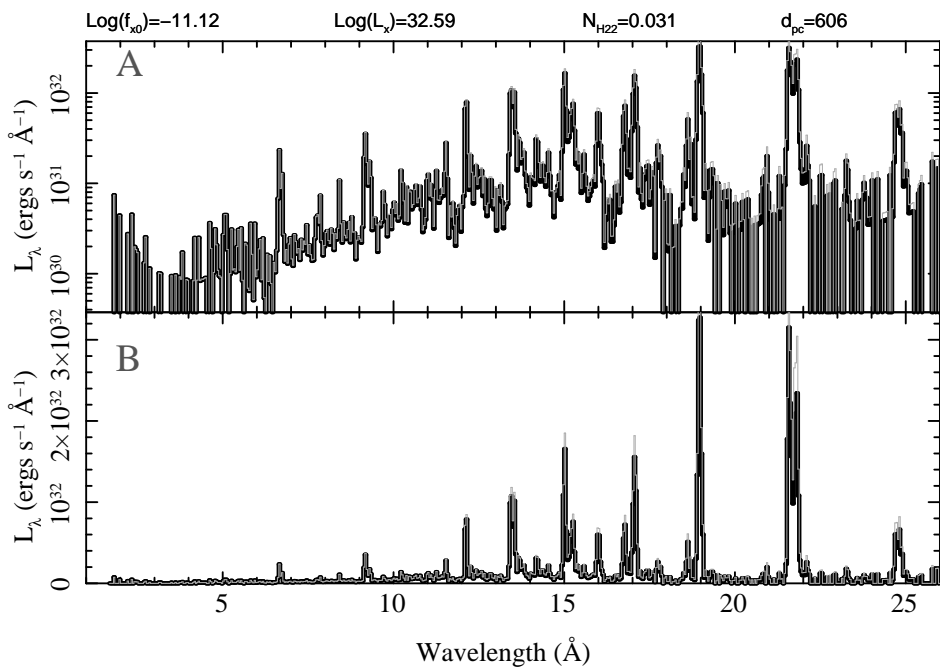


Figure C14. ϵ Ori

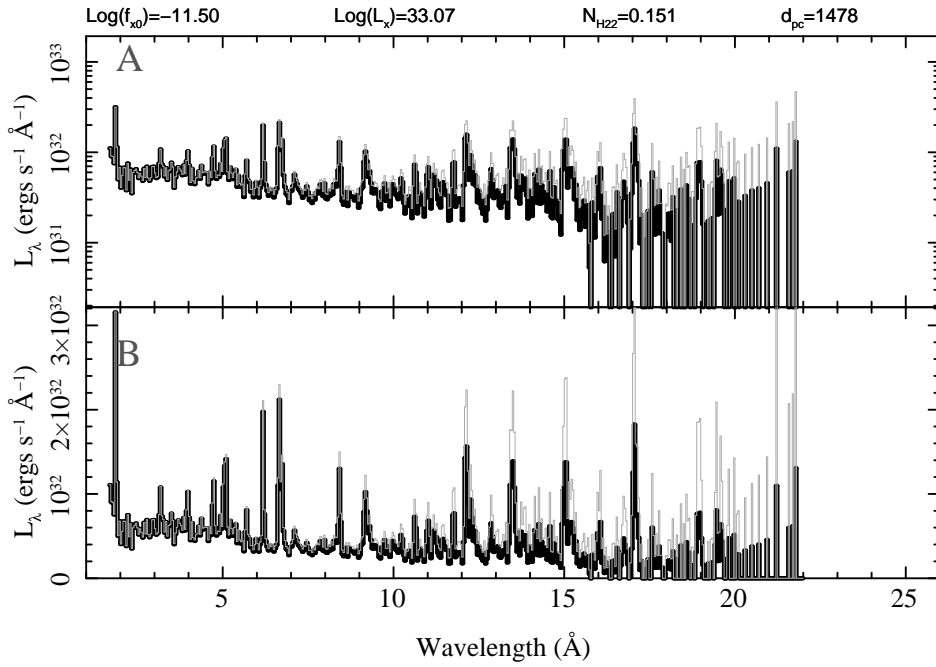
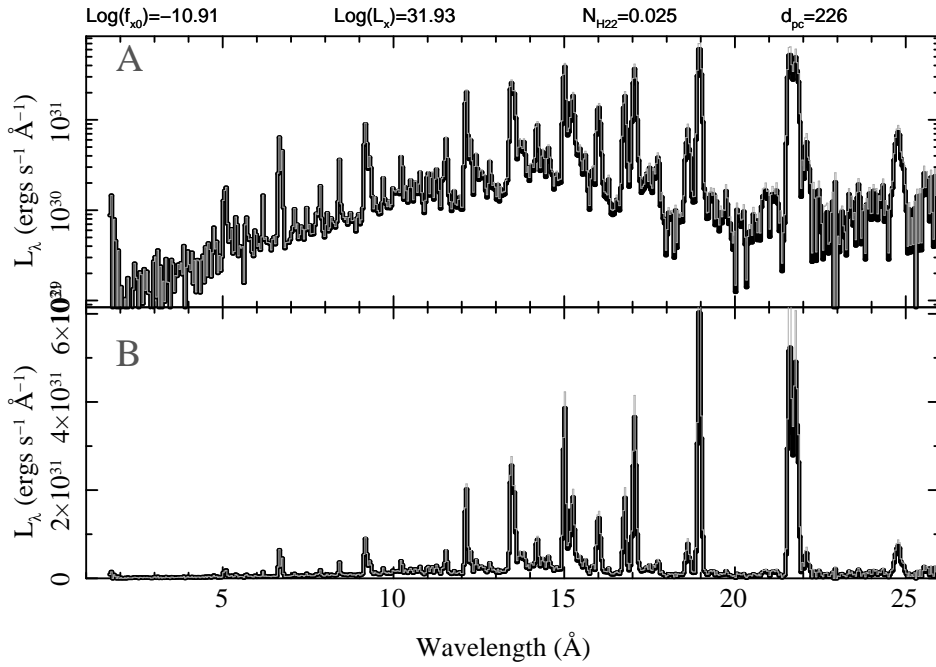
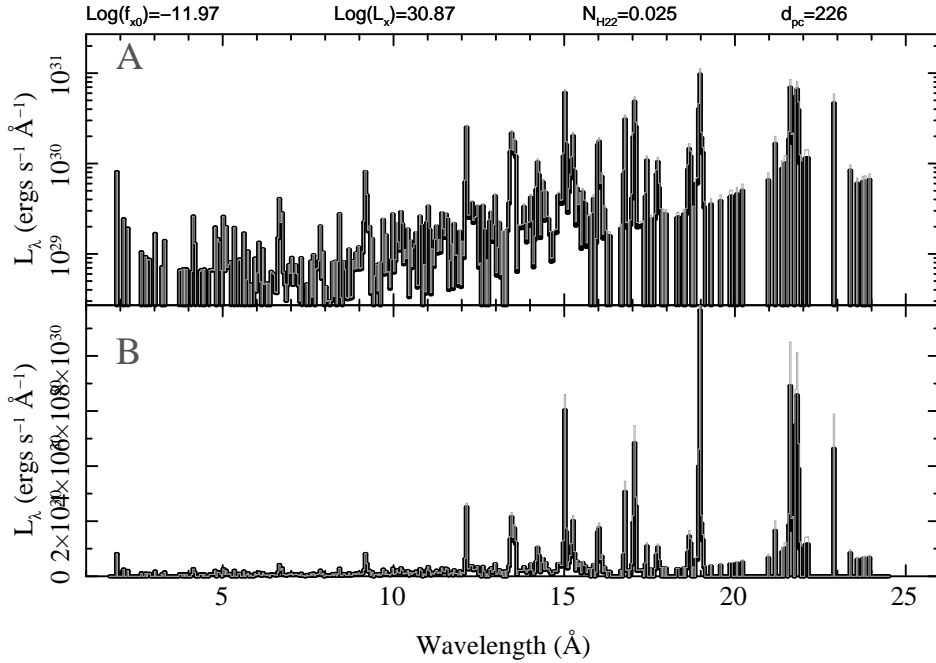
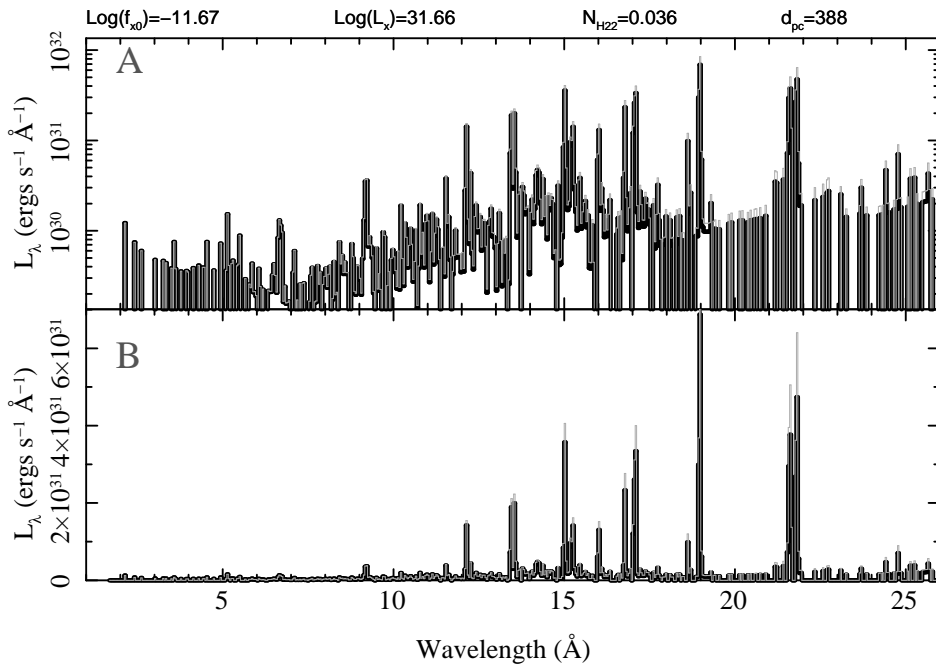


Figure C15. V640 Mon

Figure C16. ζ Ori

**Figure C17.** ζ Ori B**Figure C18.** σ Ori Aa

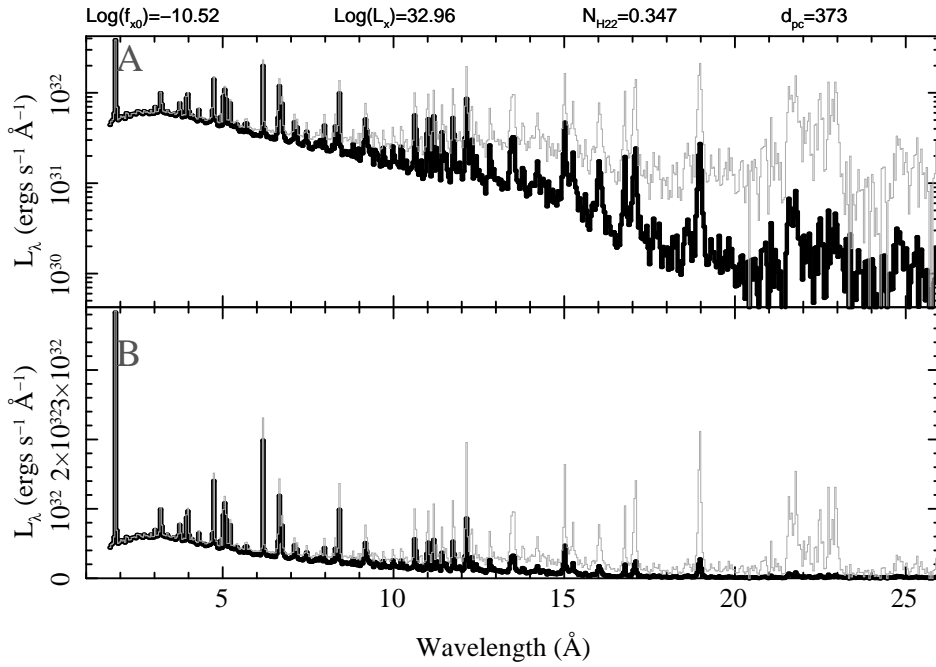


Figure C19. θ^1 Ori C

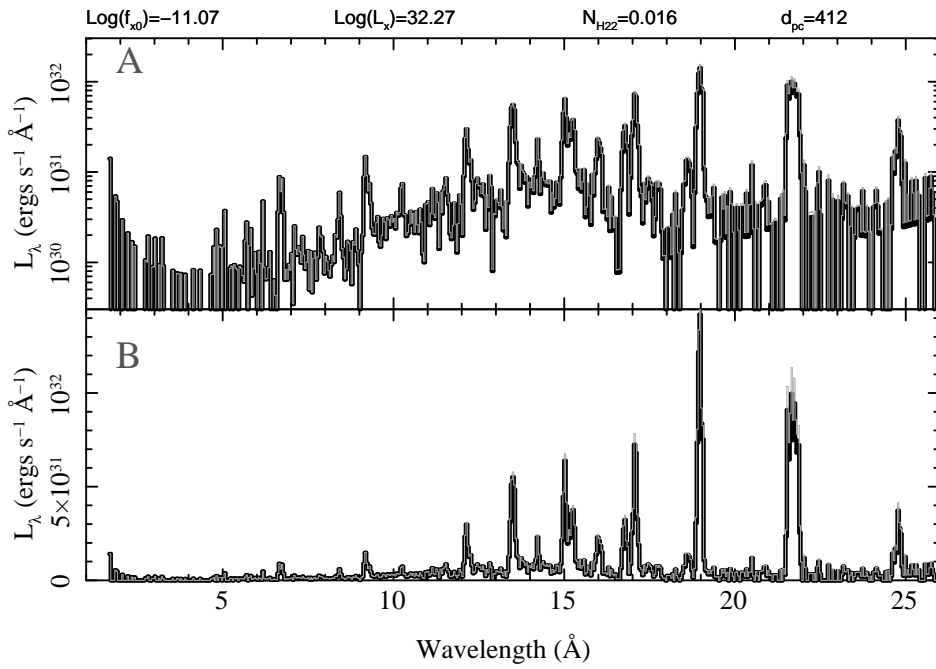
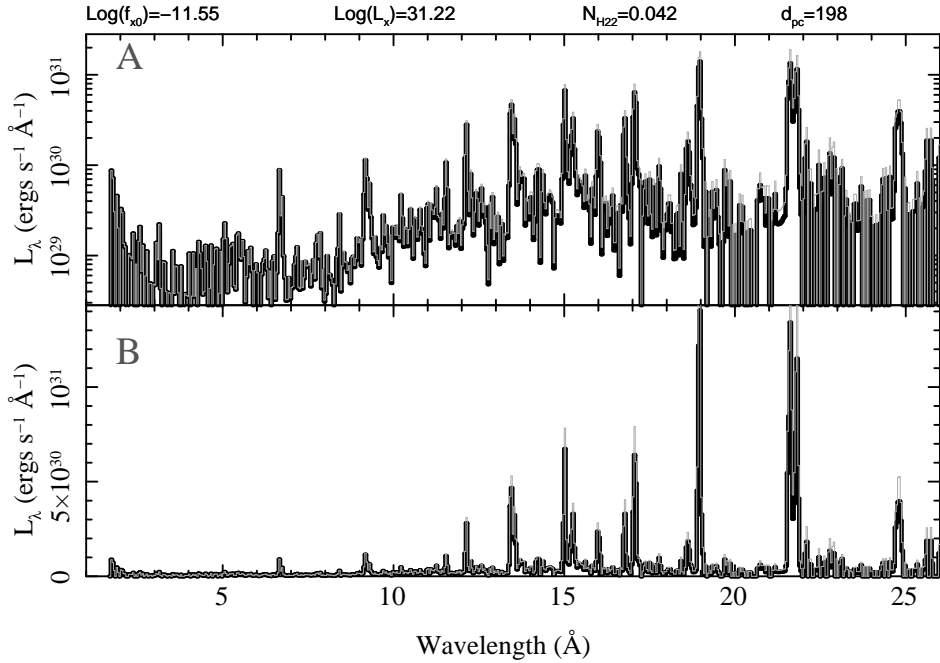
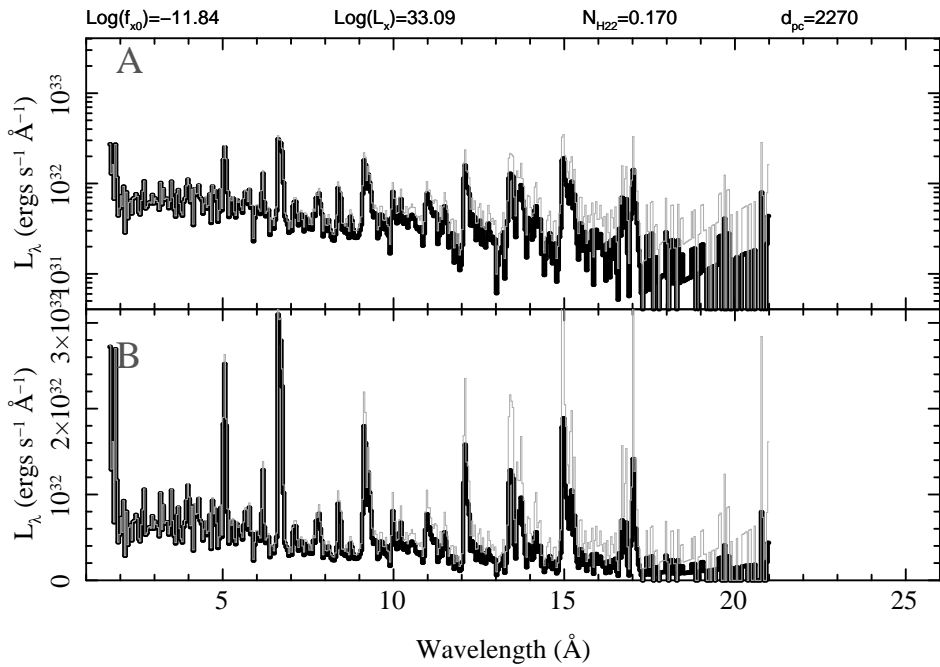


Figure C20. ν Ori

**Figure C21.** κ Ori**Figure C22.** WR 6

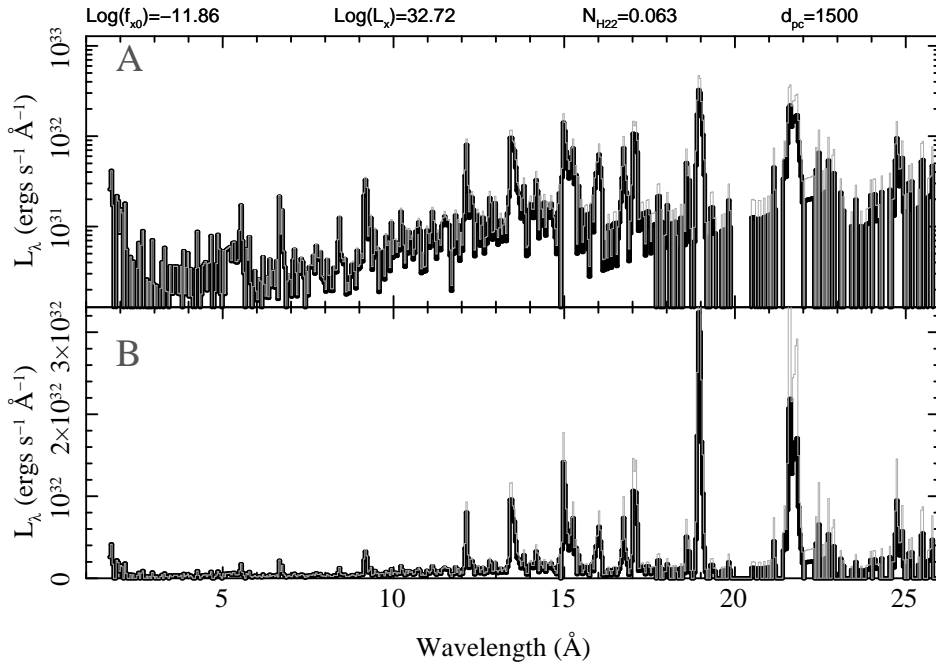
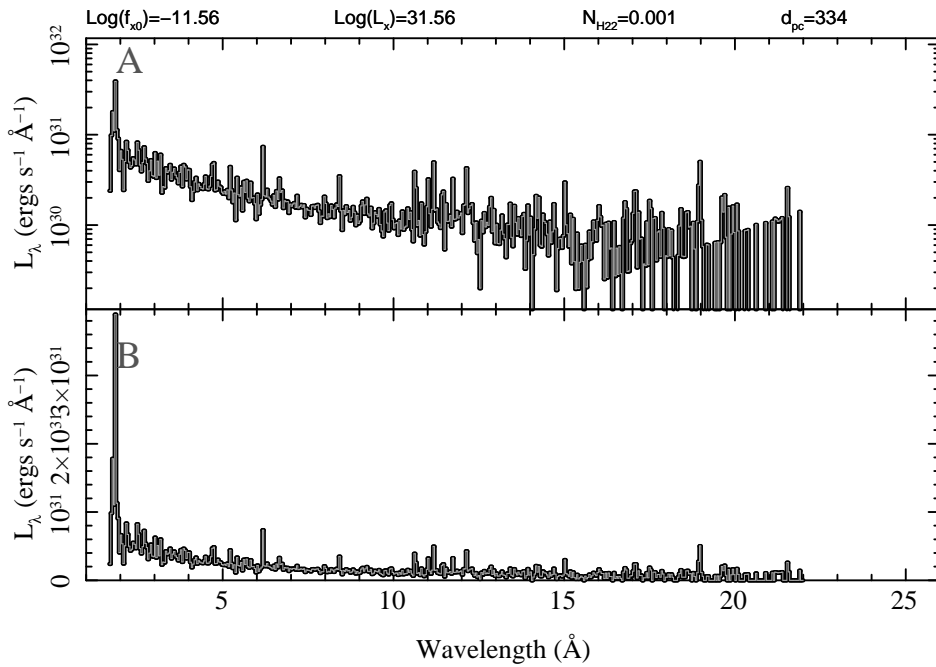
Figure C23. τ CMA

Figure C24. HD 42054

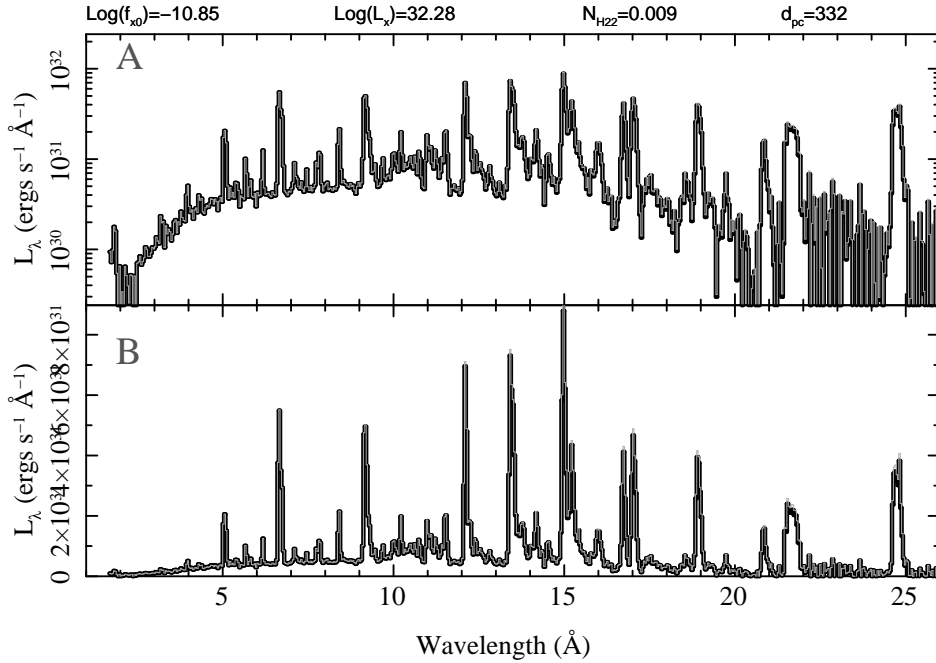


Figure C25. ζ Pup

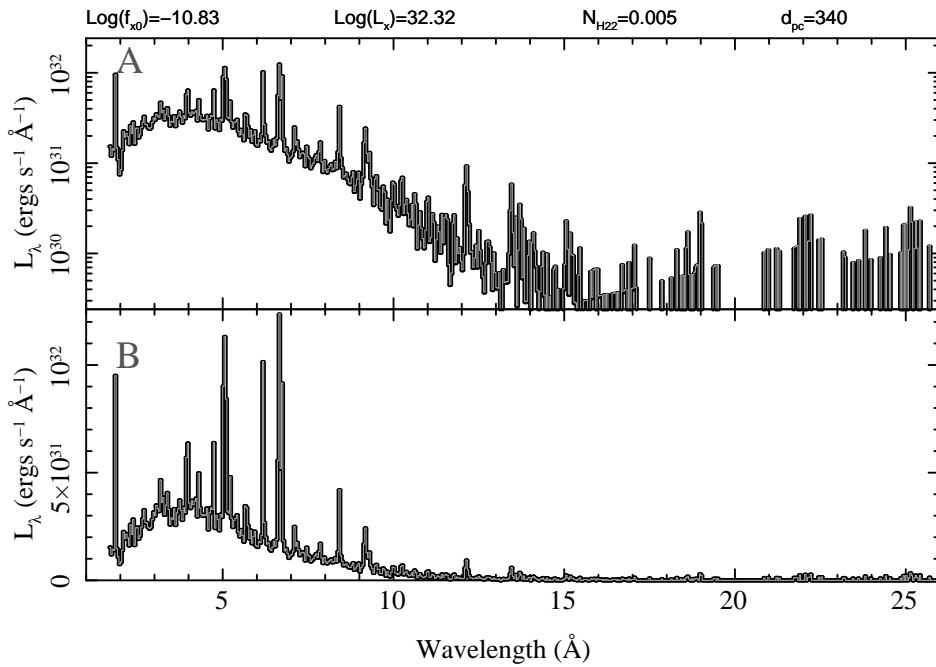


Figure C26. γ^2 Vel

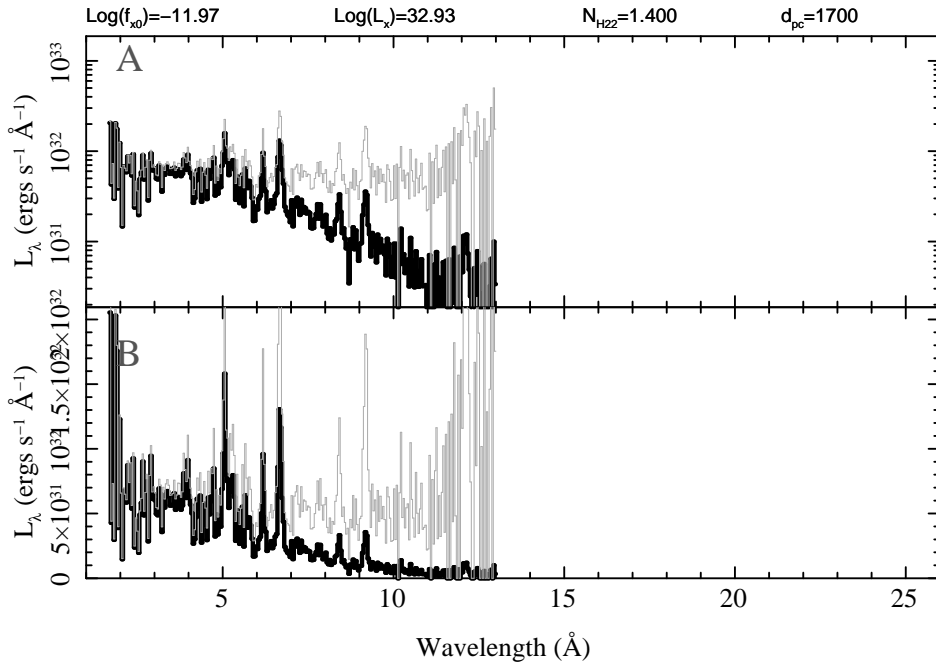


Figure C27. RCW 38 IRS 2

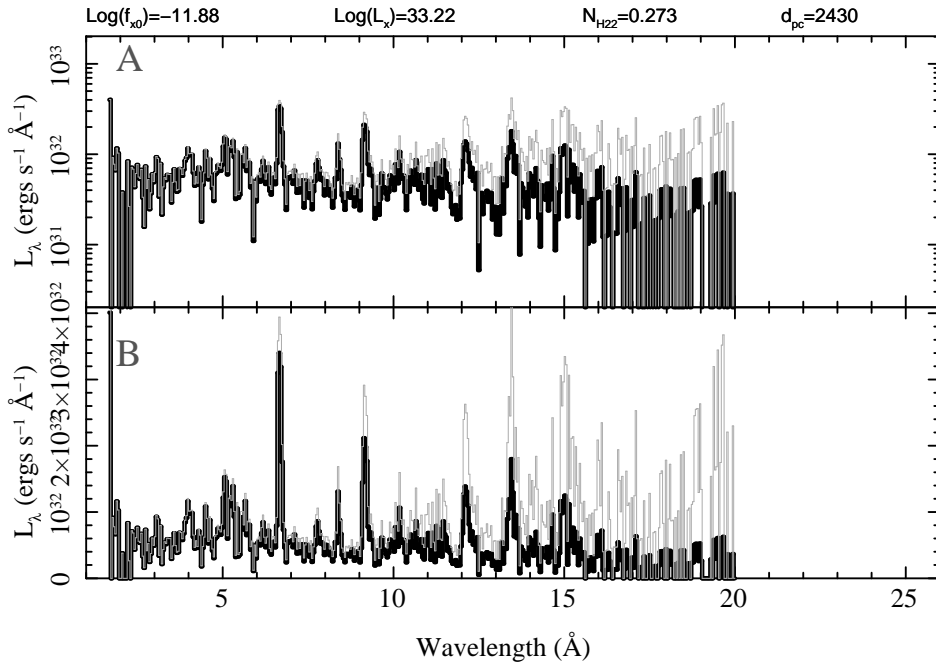


Figure C28. HD 93129A

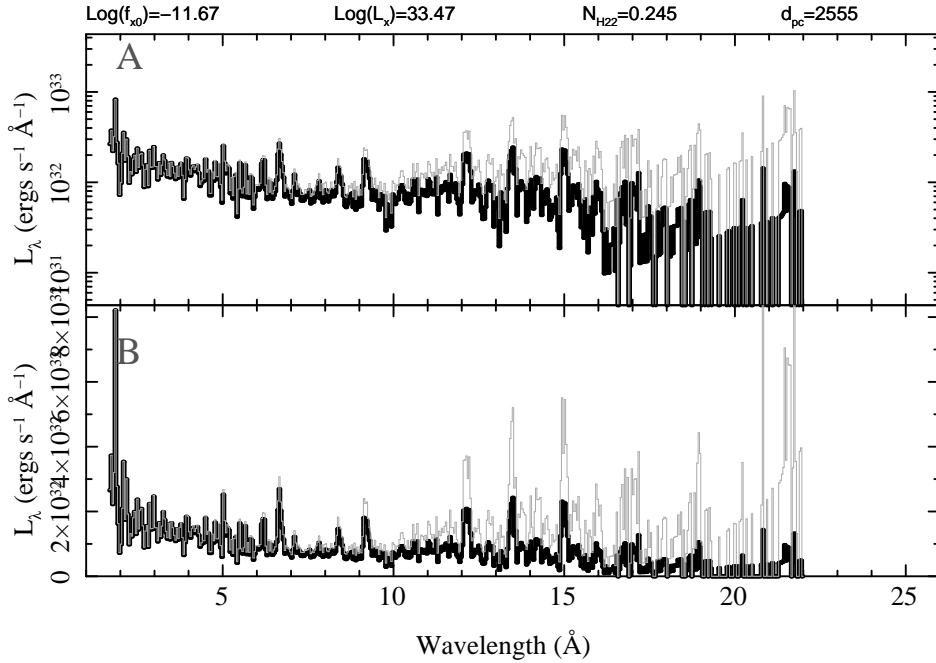


Figure C29. HD 93250

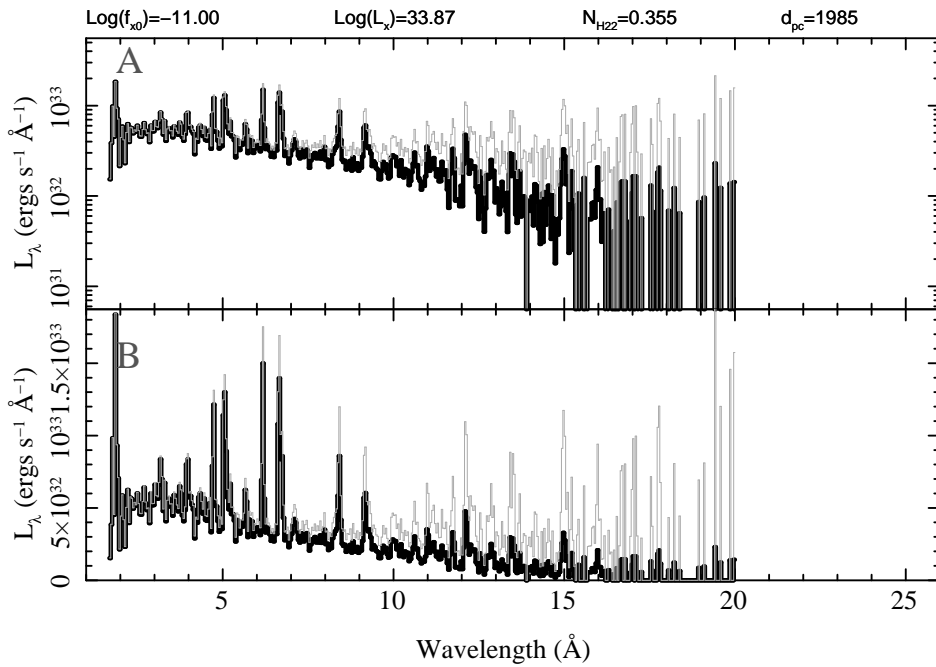
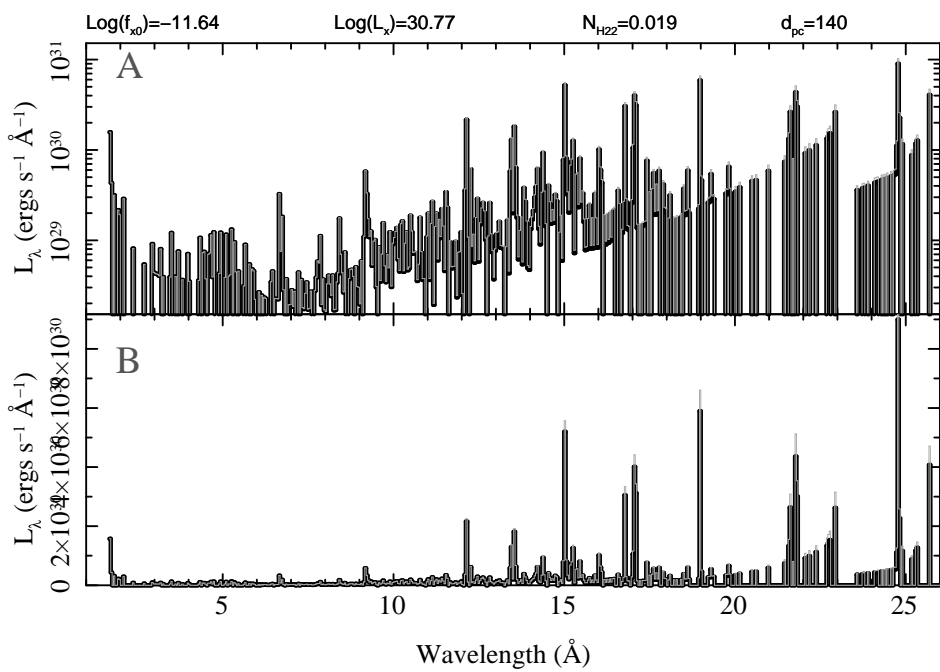
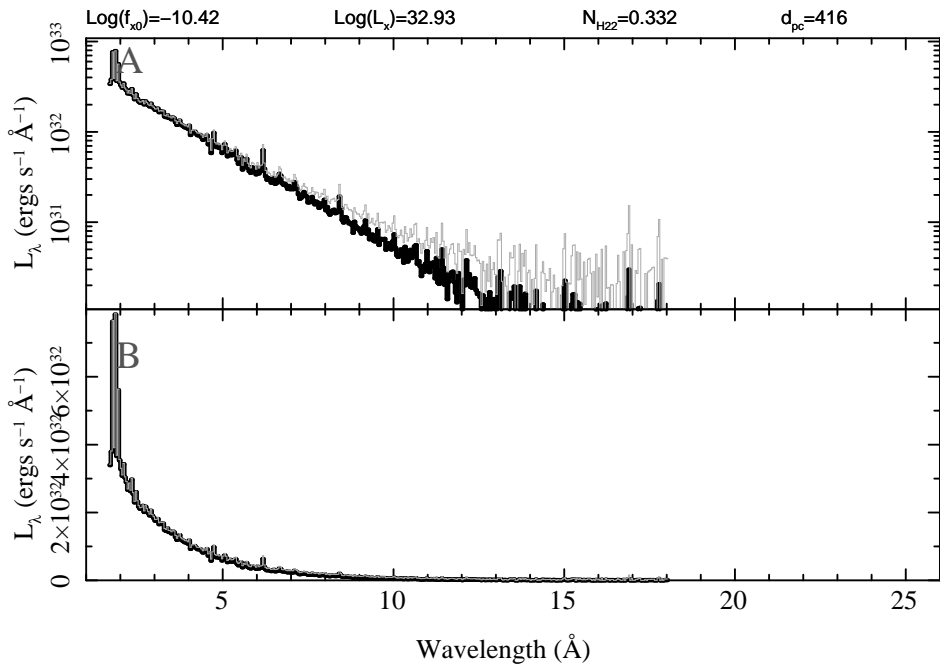
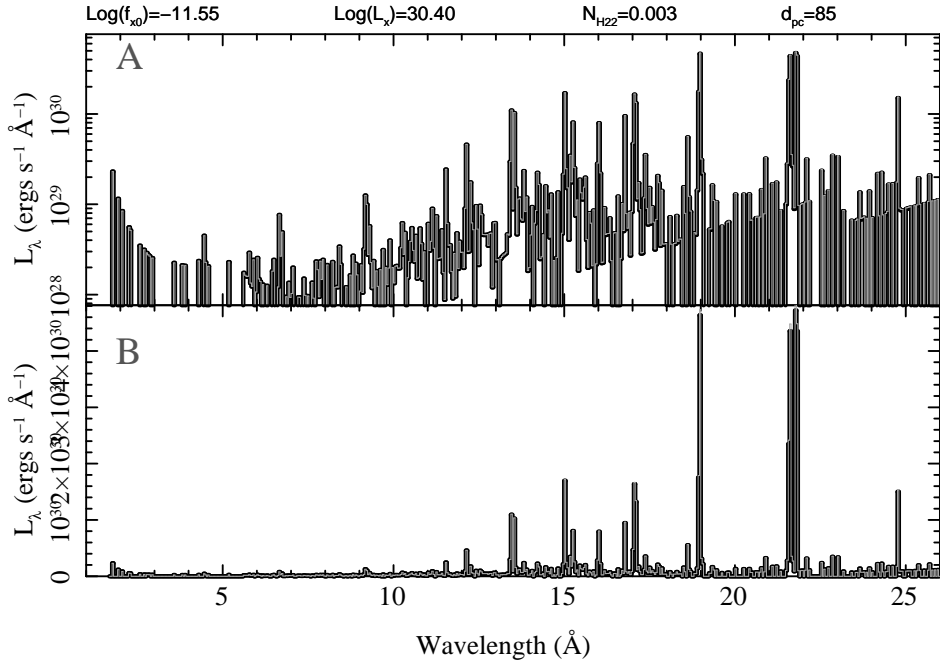
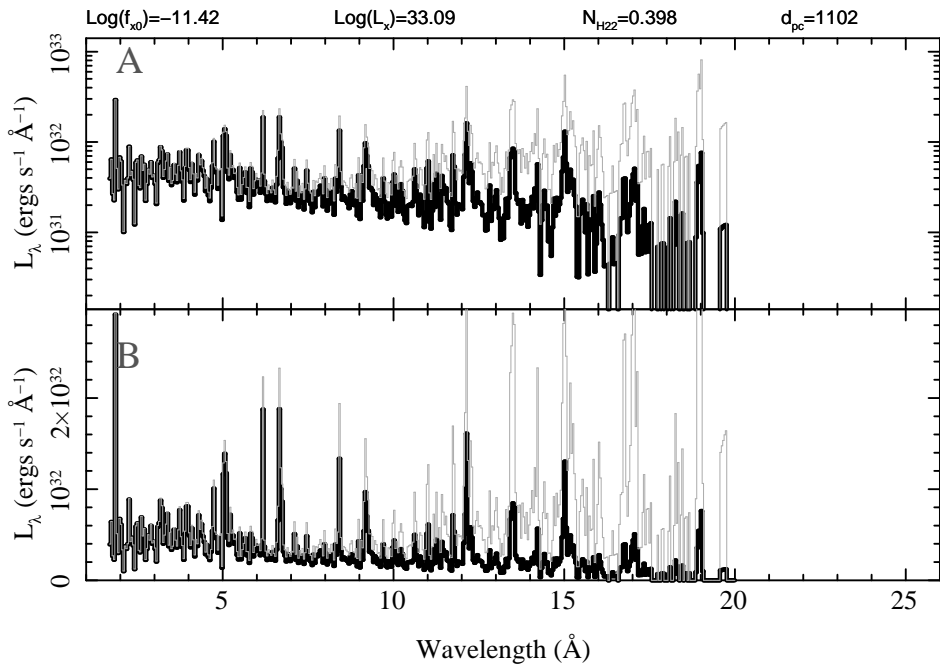


Figure C30. WR 25

**Figure C31.** θ Car**Figure C32.** HD 110432

**Figure C33.** β Cru**Figure C34.** HD 148937

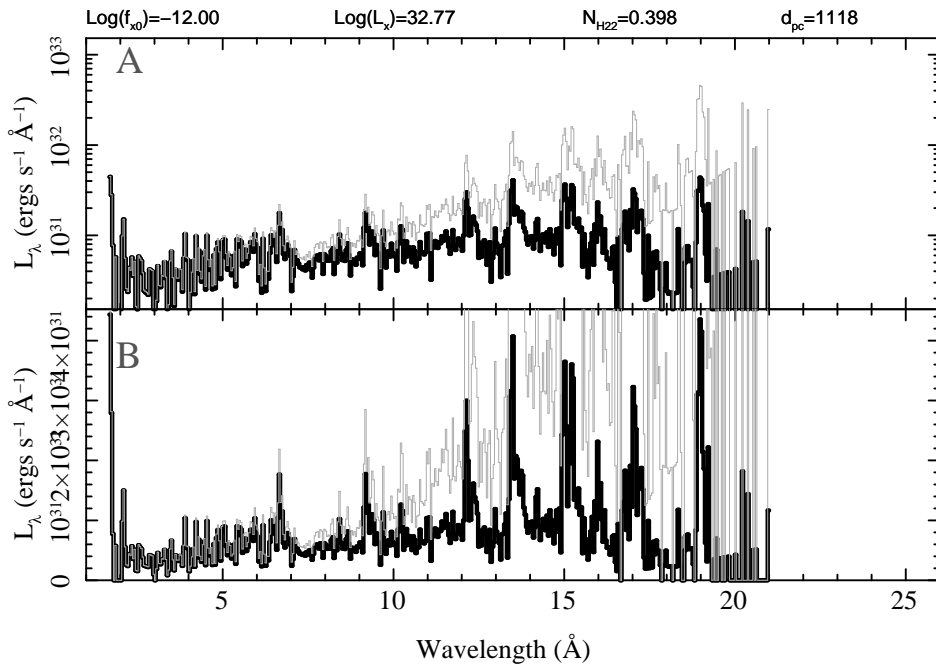


Figure C35. HD 150135

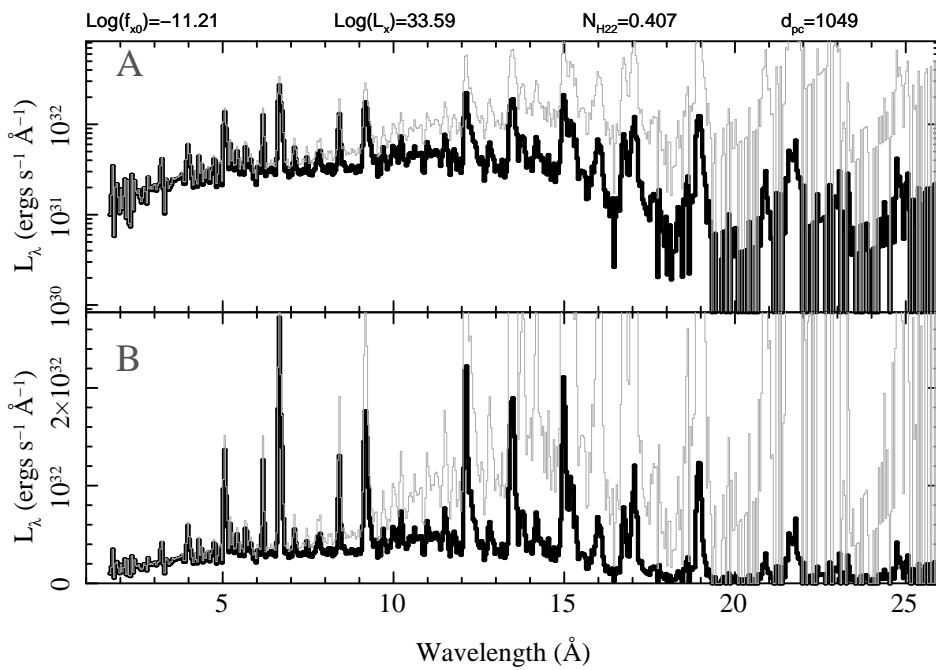


Figure C36. HD 150136

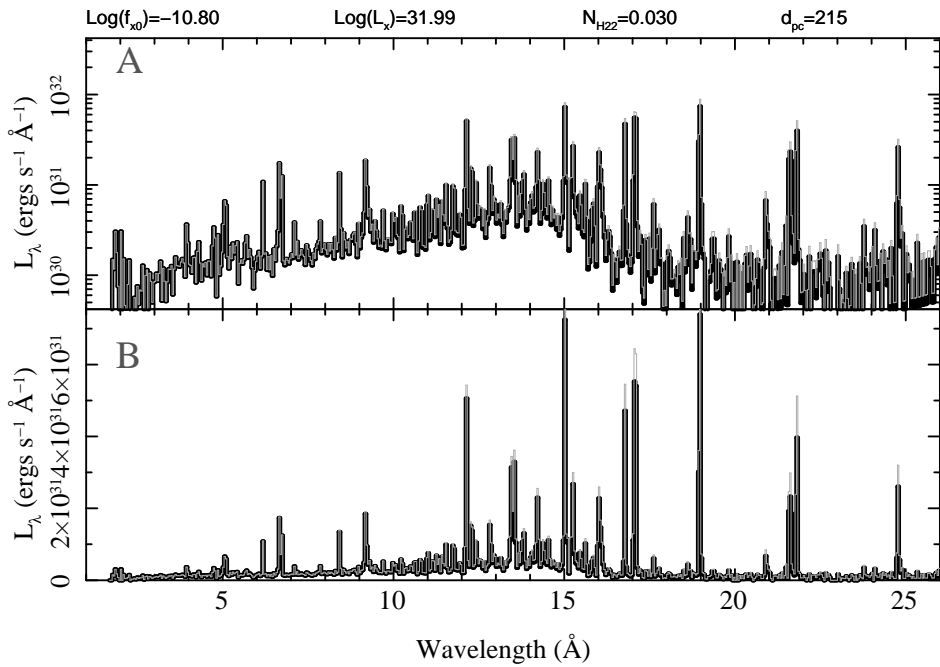


Figure C37. τ Sco

REFERENCES

- Arias, J. I., Walborn, N. R., Diaz, S. S., et al. 2016, VizieR Online Data Catalog, J/AJ/152/31
- Arnaud, K. A. 1996, in Astronomical Society of the Pacific Conference Series, Vol. 101, Astronomical Data Analysis Software and Systems V, ed. G. H. Jacoby & J. Barnes, 17–+
- Bailer-Jones, C. A. L., Rybizki, J., Fouesneau, M., Mantelet, G., & Andrae, R. 2018, AJ, 156, 58, doi: [10.3847/1538-3881/aacb21](https://doi.org/10.3847/1538-3881/aacb21)
- Berghofer, T. W., Schmitt, J. H. M. M., Danner, R., & Cassinelli, J. P. 1997, A&A, 322, 167
- Broos, P. S., Feigelson, E. D., Townsley, L. K., et al. 2007, ApJS, 169, 353, doi: [10.1086/512068](https://doi.org/10.1086/512068)
- Brown, J. C., Richardson, L. L., Antokhin, I., et al. 1995, A&A, 295, 725
- Canizares, C. R., Davis, J. E., Dewey, D., et al. 2005, PASP, 117, 1144, doi: [10.1086/432898](https://doi.org/10.1086/432898)
- Cazorla, C., & Nazé, Y. 2017, A&A, 608, A54, doi: [10.1051/0004-6361/201731562](https://doi.org/10.1051/0004-6361/201731562)
- Cohen, D. H., Kuhn, M. A., Gagné, M., Jensen, E. L. N., & Miller, N. A. 2008, MNRAS, 386, 1855, doi: [10.1111/j.1365-2966.2008.13176.x](https://doi.org/10.1111/j.1365-2966.2008.13176.x)
- Cohen, D. H., Leutenegger, M. A., Wollman, E. E., et al. 2010a, MNRAS, 405, 2391, doi: [10.1111/j.1365-2966.2010.16606.x](https://doi.org/10.1111/j.1365-2966.2010.16606.x)
- . 2010b, MNRAS, 405, 2391, doi: [10.1111/j.1365-2966.2010.16606.x](https://doi.org/10.1111/j.1365-2966.2010.16606.x)
- Cohen, D. H., Li, Z., Gayley, K. G., et al. 2014a, MNRAS, 444, 3729, doi: [10.1093/mnras/stu1661](https://doi.org/10.1093/mnras/stu1661)
- Cohen, D. H., Overdorff, A. M., Leutenegger, M. A., et al. 2022, MNRAS, doi: [10.1093/mnras/stac899](https://doi.org/10.1093/mnras/stac899)
- Cohen, D. H., Parts, V. V., Doskoch, G. M., et al. 2021a, MNRAS, 503, 715, doi: [10.1093/mnras/stab270](https://doi.org/10.1093/mnras/stab270)
- . 2021b, MNRAS, 503, 715, doi: [10.1093/mnras/stab270](https://doi.org/10.1093/mnras/stab270)
- Cohen, D. H., Wang, J., Petit, V., et al. 2020a, MNRAS, 499, 6044, doi: [10.1093/mnras/staa3124](https://doi.org/10.1093/mnras/staa3124)
- . 2020b, MNRAS, 499, 6044, doi: [10.1093/mnras/staa3124](https://doi.org/10.1093/mnras/staa3124)
- Cohen, D. H., Wollman, E. E., Leutenegger, M. A., et al. 2014b, MNRAS, 439, 908, doi: [10.1093/mnras/stu008](https://doi.org/10.1093/mnras/stu008)
- Corcoran, M. F., Swank, J. H., Petre, R., et al. 2001, ApJ, 562, 1031, doi: [10.1086/323322](https://doi.org/10.1086/323322)
- De Marco, O., Schmutz, W., Crowther, P. A., et al. 2000, A&A, 358, 187. <https://arxiv.org/abs/astro-ph/0004081>
- de Mink, S. E., Langer, N., Izzard, R. G., Sana, H., & de Koter, A. 2013, ApJ, 764, 166, doi: [10.1088/0004-637X/764/2/166](https://doi.org/10.1088/0004-637X/764/2/166)
- DeRose, K. L., Bourke, T. L., Gutermuth, R. A., et al. 2009, AJ, 138, 33, doi: [10.1088/0004-6256/138/1/33](https://doi.org/10.1088/0004-6256/138/1/33)
- Diplas, A., & Savage, B. D. 1994, ApJS, 93, 211, doi: [10.1086/192052](https://doi.org/10.1086/192052)
- Ezoe, Y., Ohashi, T., & Mitsuda, K. 2021, Reviews of Modern Plasma Physics, 5, 4, doi: [10.1007/s41614-021-00052-2](https://doi.org/10.1007/s41614-021-00052-2)
- Fabry, M., Hawcroft, C., Frost, A. J., et al. 2021, A&A, 651, A119, doi: [10.1051/0004-6361/202140452](https://doi.org/10.1051/0004-6361/202140452)
- Feldmeier, A., & Owocki, S. 1998, Ap&SS, 260, 113, doi: [10.1023/A:1001883105698](https://doi.org/10.1023/A:1001883105698)
- Feldmeier, A., Puls, J., & Pauldrach, A. W. A. 1997, A&A, 322, 878
- Fossati, L., Castro, N., Schöller, M., et al. 2015, A&A, 582, A45, doi: [10.1051/0004-6361/201526725](https://doi.org/10.1051/0004-6361/201526725)
- Foster, A. R., Ji, L., Smith, R. K., & Brickhouse, N. S. 2012, ApJ, 756, 128, doi: [10.1088/0004-637X/756/2/128](https://doi.org/10.1088/0004-637X/756/2/128)

- Fruscione, A., McDowell, J. C., Allen, G. E., et al. 2006, in Presented at the Society of Photo-Optical Instrumentation Engineers (SPIE) Conference, Vol. 6270, SPIE Conference Series, doi: [10.1117/12.671760](https://doi.org/10.1117/12.671760)
- Gayley, K. G. 2014, ApJ, 788, 90, doi: [10.1088/0004-637X/788/1/90](https://doi.org/10.1088/0004-637X/788/1/90)
- Gruner, D., Hainich, R., Sander, A. A. C., et al. 2019, A&A, 621, A63, doi: [10.1051/0004-6361/201833178](https://doi.org/10.1051/0004-6361/201833178)
- Güdel, M., & Nazé, Y. 2009, A&A Rev., 17, 309, doi: [10.1007/s00159-009-0022-4](https://doi.org/10.1007/s00159-009-0022-4)
- Hamann, W. R., & Koesterke, L. 1998, A&A, 335, 1003
- Hamann, W. R., Gräfener, G., Liermann, A., et al. 2019, A&A, 625, A57, doi: [10.1051/0004-6361/201834850](https://doi.org/10.1051/0004-6361/201834850)
- Haucke, M., Cidale, L. S., Venero, R. O. J., et al. 2018, A&A, 614, A91, doi: [10.1051/0004-6361/201731678](https://doi.org/10.1051/0004-6361/201731678)
- Hillier, D. J. 1991, A&A, 247, 455
- Hiltner, W. A., Garrison, R. F., & Schild, R. E. 1969, ApJ, 157, 313, doi: [10.1086/150069](https://doi.org/10.1086/150069)
- Houck, J. C., & Denicola, L. A. 2000, in Astronomical Society of the Pacific Conference Series, Vol. 216, Astronomical Data Analysis Software and Systems IX, ed. N. Manset, C. Veillet, & D. Crabtree, 591
- Hubrig, S., Briquet, M., Morel, T., et al. 2008a, A&A, 488, 287, doi: [10.1051/0004-6361:200809972](https://doi.org/10.1051/0004-6361:200809972)
- Hubrig, S., Schöller, M., Schnerr, R. S., et al. 2008b, A&A, 490, 793, doi: [10.1051/0004-6361:200810171](https://doi.org/10.1051/0004-6361:200810171)
- Huenemoerder, D. P., Mitschang, A., Dewey, D., et al. 2011, The Astronomical Journal, 141, 129, doi: [10.1088/0004-6256/141/4/129](https://doi.org/10.1088/0004-6256/141/4/129)
- Huenemoerder, D. P., Gayley, K. G., Hamann, W. R., et al. 2015a, ApJ, 815, 29, doi: [10.1088/0004-637X/815/1/29](https://doi.org/10.1088/0004-637X/815/1/29)
- Huenemoerder, D. P., Gayley, K. G., Hamann, W.-R., et al. 2015b, ApJ, 815, 29, doi: [10.1088/0004-637X/815/1/29](https://doi.org/10.1088/0004-637X/815/1/29)
- Huenemoerder, D. P., Ignace, R., Miller, N. A., et al. 2020, ApJ, 893, 52, doi: [10.3847/1538-4357/ab8005](https://doi.org/10.3847/1538-4357/ab8005)
- Ignace, R. 2016, Advances in Space Research, 58, 694, doi: [10.1016/j.asr.2015.12.044](https://doi.org/10.1016/j.asr.2015.12.044)
- Koen, C., & Johnston, C. 2021, MNRAS, 505, 5725, doi: [10.1093/mnras/stab1652](https://doi.org/10.1093/mnras/stab1652)
- Lesh, J. R. 1968, ApJS, 17, 371, doi: [10.1086/190179](https://doi.org/10.1086/190179)
- Leutenegger, M. A., Cohen, D. H., Zsargó, J., et al. 2010, ApJ, 719, 1767, doi: [10.1088/0004-637X/719/2/1767](https://doi.org/10.1088/0004-637X/719/2/1767)
- Linder, N., Rauw, G., Martins, F., et al. 2008, A&A, 489, 713, doi: [10.1051/0004-6361:200810003](https://doi.org/10.1051/0004-6361:200810003)
- Liszt, H. 2014a, ApJ, 780, 10, doi: [10.1088/0004-637X/780/1/10](https://doi.org/10.1088/0004-637X/780/1/10)
- . 2014b, ApJ, 783, 17, doi: [10.1088/0004-637X/783/1/17](https://doi.org/10.1088/0004-637X/783/1/17)
- Long, K. S., & White, R. L. 1980, ApJ, 239, L65, doi: [10.1086/183293](https://doi.org/10.1086/183293)
- Lucy, L. B., & White, R. L. 1980, ApJ, 241, 300, doi: [10.1086/158342](https://doi.org/10.1086/158342)
- Mahy, L., Gosset, E., Sana, H., et al. 2012, A&A, 540, A97, doi: [10.1051/0004-6361/201118199](https://doi.org/10.1051/0004-6361/201118199)
- Maíz Apellániz, J., & Barbá, R. H. 2020, A&A, 636, A28, doi: [10.1051/0004-6361/202037730](https://doi.org/10.1051/0004-6361/202037730)
- Maíz Apellániz, J., Crespo Bellido, P., Barbá, R. H., Fernández Aranda, R., & Sota, A. 2020a, A&A, 643, A138, doi: [10.1051/0004-6361/202038228](https://doi.org/10.1051/0004-6361/202038228)
- . 2020b, A&A, 643, A138, doi: [10.1051/0004-6361/202038228](https://doi.org/10.1051/0004-6361/202038228)
- Maíz Apellániz, J., Sana, H., Barbá, R. H., Le Bouquin, J. B., & Gamen, R. C. 2017, MNRAS, 464, 3561, doi: [10.1093/mnras/stw2618](https://doi.org/10.1093/mnras/stw2618)

- Maíz Apellániz, J., Sota, A., Arias, J. I., et al. 2016, *ApJS*, 224, 4,
doi: [10.3847/0067-0049/224/1/4](https://doi.org/10.3847/0067-0049/224/1/4)
- Maíz Apellániz, J., Trigueros Páez, E., Negueruela, I., et al. 2019, *A&A*, 626, A20,
doi: [10.1051/0004-6361/201935359](https://doi.org/10.1051/0004-6361/201935359)
- Marcolino, W. L. F., Bouret, J. C., Sundqvist, J. O., et al. 2013, *MNRAS*, 431, 2253,
doi: [10.1093/mnras/stt323](https://doi.org/10.1093/mnras/stt323)
- Martins, F., Schaefer, D., & Hillier, D. J. 2005, *A&A*, 436, 1049,
doi: [10.1051/0004-6361:20042386](https://doi.org/10.1051/0004-6361:20042386)
- Nazé, Y. 2009, *A&A*, 506, 1055,
doi: [10.1051/0004-6361/200912659](https://doi.org/10.1051/0004-6361/200912659)
- Nazé, Y., Flores, C. A., & Rauw, G. 2012, *A&A*, 538, A22, doi: [10.1051/0004-6361/201117387](https://doi.org/10.1051/0004-6361/201117387)
- Nazé, Y., & Motch, C. 2018, *A&A*, 619, A148,
doi: [10.1051/0004-6361/201833842](https://doi.org/10.1051/0004-6361/201833842)
- Nazé, Y., Petit, V., Rinbrand, M., et al. 2014, *ApJS*, 215, 10,
doi: [10.1088/0067-0049/215/1/10](https://doi.org/10.1088/0067-0049/215/1/10)
- Nazé, Y., & Rauw, G. 2008, *A&A*, 490, 801,
doi: [10.1051/0004-6361:200810364](https://doi.org/10.1051/0004-6361:200810364)
- Nazé, Y., Rauw, G., Czesla, S., Mahy, L., & Campos, F. 2019, *A&A*, 627, A99,
doi: [10.1051/0004-6361/201935141](https://doi.org/10.1051/0004-6361/201935141)
- Nazé, Y., Rauw, G., Czesla, S., Smith, M. A., & Robrade, J. 2022, *MNRAS*, 510, 2286,
doi: [10.1093/mnras/stab3378](https://doi.org/10.1093/mnras/stab3378)
- Nazé, Y., ud-Doula, A., & Zhekov, S. A. 2016, *ApJ*, 831, 138,
doi: [10.3847/0004-637X/831/2/138](https://doi.org/10.3847/0004-637X/831/2/138)
- Nazé, Y., Walborn, N. R., Rauw, G., et al. 2008, *AJ*, 135, 1946,
doi: [10.1088/0004-6256/135/5/1946](https://doi.org/10.1088/0004-6256/135/5/1946)
- Nebot Gómez-Morán, A., & Oskinova, L. M. 2018a, *A&A*, 620, A89,
doi: [10.1051/0004-6361/201833453](https://doi.org/10.1051/0004-6361/201833453)
- . 2018b, *A&A*, 620, A89,
doi: [10.1051/0004-6361/201833453](https://doi.org/10.1051/0004-6361/201833453)
- Nichols, J. S., Nazé, Y., Huenemoerder, D. P., et al. 2021, *ApJ*, 906, 89,
doi: [10.3847/1538-4357/abca3a](https://doi.org/10.3847/1538-4357/abca3a)
- Nieva, M.-F., & Przybilla, N. 2014, *A&A*, 566, A7, doi: [10.1051/0004-6361/201423373](https://doi.org/10.1051/0004-6361/201423373)
- Oskinova, L., Hamann, W.-R., Ignace, R., & Feldmeier, A. 2011a, *Bulletin de la Societe Royale des Sciences de Liege*, 80, 54.
<https://arxiv.org/abs/1012.1857>
- Oskinova, L. M. 2005, *Monthly Notices of the Royal Astronomical Society*, 361, 679,
doi: [10.1111/j.1365-2966.2005.09229.x](https://doi.org/10.1111/j.1365-2966.2005.09229.x)
- Oskinova, L. M. 2016, *Advances in Space Research*, 58, 739,
doi: [10.1016/j.asr.2016.06.030](https://doi.org/10.1016/j.asr.2016.06.030)
- Oskinova, L. M., Feldmeier, A., & Hamann, W. R. 2006, *MNRAS*, 372, 313,
doi: [10.1111/j.1365-2966.2006.10858.x](https://doi.org/10.1111/j.1365-2966.2006.10858.x)
- Oskinova, L. M., Huenemoerder, D. P., Hamann, W. R., et al. 2017, *ApJ*, 845, 39,
doi: [10.3847/1538-4357/aa7e79](https://doi.org/10.3847/1538-4357/aa7e79)
- Oskinova, L. M., Todt, H., Ignace, R., et al. 2011b, *MNRAS*, 416, 1456,
doi: [10.1111/j.1365-2966.2011.19143.x](https://doi.org/10.1111/j.1365-2966.2011.19143.x)
- Owocki, S. P., & Cohen, D. H. 2006, *ApJ*, 648, 565, doi: [10.1086/505698](https://doi.org/10.1086/505698)
- Owocki, S. P., Sundqvist, J. O., Cohen, D. H., & Gayley, K. G. 2013, *MNRAS*, 429, 3379,
doi: [10.1093/mnras/sts599](https://doi.org/10.1093/mnras/sts599)
- Pablo, H., Richardson, N. D., Fuller, J., et al. 2017, *MNRAS*, 467, 2494,
doi: [10.1093/mnras/stx207](https://doi.org/10.1093/mnras/stx207)
- Pajot, F., Barret, D., Lam-Trong, T., et al. 2018, *Journal of Low Temperature Physics*, 193, 901,
doi: [10.1007/s10909-018-1904-5](https://doi.org/10.1007/s10909-018-1904-5)
- Parkin, E. R., & Pittard, J. M. 2008, *MNRAS*, 388, 1047,
doi: [10.1111/j.1365-2966.2008.13511.x](https://doi.org/10.1111/j.1365-2966.2008.13511.x)
- Pollock, A. M. T., Corcoran, M. F., Stevens, I. R., & Williams, P. M. 2005, *ApJ*, 629, 482,
doi: [10.1086/431193](https://doi.org/10.1086/431193)

- Pradhan, P., Huenemoerder, D. P., Ignace, R., Pollock, A. M. T., & Nichols, J. S. 2021, arXiv e-prints, arXiv:2103.05053.
<https://arxiv.org/abs/2103.05053>
- Pradhan, P., Huenemoerder, D. P., Ignace, R., Pollock, A. M. T., & Nichols, J. S. 2021, *The Astrophysical Journal*, 915, 114, doi: [10.3847/1538-4357/ac02c4](https://doi.org/10.3847/1538-4357/ac02c4)
- Prinja, R. K., Barlow, M. J., & Howarth, I. D. 1990, *ApJ*, 361, 607, doi: [10.1086/169224](https://doi.org/10.1086/169224)
- Puebla, R. E., Hillier, D. J., Zsargó, J., Cohen, D. H., & Leutenegger, M. A. 2016, *MNRAS*, 456, 2907, doi: [10.1093/mnras/stv2783](https://doi.org/10.1093/mnras/stv2783)
- Puls, J., Markova, N., Scuderi, S., et al. 2006a, *A&A*, 454, 625, doi: [10.1051/0004-6361:20065073](https://doi.org/10.1051/0004-6361:20065073)
- . 2006b, *A&A*, 454, 625, doi: [10.1051/0004-6361:20065073](https://doi.org/10.1051/0004-6361:20065073)
- Rate, G., & Crowther, P. A. 2020, *MNRAS*, 493, 1512, doi: [10.1093/mnras/stz3614](https://doi.org/10.1093/mnras/stz3614)
- Rauw, G., & Nazé, Y. 2016, *A&A*, 594, A82, doi: [10.1051/0004-6361/201629207](https://doi.org/10.1051/0004-6361/201629207)
- Rauw, G., Blomme, R., Nazé, Y., et al. 2016, *A&A*, 589, A121, doi: [10.1051/0004-6361/201526871](https://doi.org/10.1051/0004-6361/201526871)
- Rowan, T. 1990, PhD thesis, Department of Computer Sciences, University of Texas at Austin
- Sana, H., de Mink, S. E., de Koter, A., et al. 2012, *Science*, 337, 444, doi: [10.1126/science.1223344](https://doi.org/10.1126/science.1223344)
- Schaefer, G. H., Hummel, C. A., Gies, D. R., et al. 2016, *AJ*, 152, 213, doi: [10.3847/0004-6256/152/6/213](https://doi.org/10.3847/0004-6256/152/6/213)
- Schmutz, W., Schweickhardt, J., Stahl, O., et al. 1997, *A&A*, 328, 219
- Shenar, T., Osokinova, L., Hamann, W. R., et al. 2015, *ApJ*, 809, 135, doi: [10.1088/0004-637X/809/2/135](https://doi.org/10.1088/0004-637X/809/2/135)
- Skinner, S. L., Sokal, K. R., Cohen, D. H., et al. 2008, *ApJ*, 683, 796, doi: [10.1086/589917](https://doi.org/10.1086/589917)
- Skinner, S. L., Zhekov, S. A., Palla, F., & Barbosa, C. L. D. R. 2005, *MNRAS*, 361, 191, doi: [10.1111/j.1365-2966.2005.09154.x](https://doi.org/10.1111/j.1365-2966.2005.09154.x)
- Slettebak, A. 1982, *ApJS*, 50, 55, doi: [10.1086/190820](https://doi.org/10.1086/190820)
- Smith, M. A., & Robinson, R. D. 1999, *ApJ*, 517, 866, doi: [10.1086/307216](https://doi.org/10.1086/307216)
- Smith, R. K., Brickhouse, N. S., Liedahl, D. A., & Raymond, J. C. 2001, *ApJ*, 556, L91, doi: [10.1086/322992](https://doi.org/10.1086/322992)
- Sota, A., Maíz Apellániz, J., Walborn, N. R., et al. 2011, *ApJS*, 193, 24, doi: [10.1088/0067-0049/193/2/24](https://doi.org/10.1088/0067-0049/193/2/24)
- Stevens, I. R., Blondin, J. M., & Pollock, A. M. T. 1992, *ApJ*, 386, 265, doi: [10.1086/171013](https://doi.org/10.1086/171013)
- Sundqvist, J. O., & Owocki, S. P. 2013, *MNRAS*, 428, 1837, doi: [10.1093/mnras/sts165](https://doi.org/10.1093/mnras/sts165)
- ud-Doula, A., & Nazé, Y. 2016, *Advances in Space Research*, 58, 680, doi: [10.1016/j.asr.2015.09.025](https://doi.org/10.1016/j.asr.2015.09.025)
- Usov, V. V. 1992, *ApJ*, 389, 635, doi: [10.1086/171236](https://doi.org/10.1086/171236)
- van Leeuwen, F. 2007, *A&A*, 474, 653, doi: [10.1051/0004-6361:20078357](https://doi.org/10.1051/0004-6361:20078357)
- Wade, G. A., Neiner, C., Alecian, E., et al. 2016, *MNRAS*, 456, 2, doi: [10.1093/mnras/stv2568](https://doi.org/10.1093/mnras/stv2568)
- Walborn, N. R., Nichols, J. S., & Waldron, W. L. 2009, *ApJ*, 703, 633, doi: [10.1088/0004-637X/703/1/633](https://doi.org/10.1088/0004-637X/703/1/633)
- Waldron, W. L., & Cassinelli, J. P. 2007, *ApJ*, 668, 456, doi: [10.1086/520919](https://doi.org/10.1086/520919)
- . 2009, *ApJ*, 692, L76, doi: [10.1088/0004-637X/692/2/L76](https://doi.org/10.1088/0004-637X/692/2/L76)
- Weidner, C., Kroupa, P., & Bonnell, I. A. D. 2010, *MNRAS*, 401, 275, doi: [10.1111/j.1365-2966.2009.15633.x](https://doi.org/10.1111/j.1365-2966.2009.15633.x)
- Willis, A. J., Schild, H., & Stevens, I. R. 1995, *A&A*, 298, 549
- Wojdowski, P. S., & Schulz, N. S. 2005, *ApJ*, 627, 953, doi: [10.1086/430586](https://doi.org/10.1086/430586)

- Wolk, S. J., Bourke, T. L., Smith, R. K., Spitzbart, B., & Alves, J. 2002, ApJ, 580, L161, doi: [10.1086/345611](https://doi.org/10.1086/345611)
- XRISM Science Team. 2020, arXiv e-prints, arXiv:2003.04962.
<https://arxiv.org/abs/2003.04962>
- Zhekov, S. A., Gagné, M., & Skinner, S. L. 2014, ApJ, 785, 8, doi: [10.1088/0004-637X/785/1/8](https://doi.org/10.1088/0004-637X/785/1/8)
- Zhekov, S. A., & Park, S. 2010, ApJ, 721, 518, doi: [10.1088/0004-637X/721/1/518](https://doi.org/10.1088/0004-637X/721/1/518)
- Zorec, J., Cidale, L., Arias, M. L., et al. 2009, A&A, 501, 297, doi: [10.1051/0004-6361/200811147](https://doi.org/10.1051/0004-6361/200811147)
- Zorec, J., Frémant, Y., & Cidale, L. 2005, A&A, 441, 235, doi: [10.1051/0004-6361:20053051](https://doi.org/10.1051/0004-6361:20053051)